LDR 101

UNCLASSIFIED

OAK RIDGE NATIONAL LABORATORY LIBRARY
3 4456 0024743 6

ORNL-1879
Progress

5

CENTRAL RESEARCH LIBRARY
DOCUMENT COLLECTION

PHYSICS DIVISION

SEMIANNUAL PROGRESS REPORT

FOR PERIOD ENDING MARCH 20, 1955

CENTRAL RESEARCH LIBRARY
DOCUMENT COLLECTION

LIBRARY LOAN COPY

DO NOT TRANSFER TO ANOTHER PERSON

If you wish someone else to see this document, send in name with document and the library will arrange a loan.

OAK RIDGE NATIONAL LABORATORY
OPERATED BY
UNION CARBIDE NUCLEAR COMPANY
A Division of Union Carbide and Carbon Corporation
UCC
POST OFFICE BOX P · OAK RIDGE, TENNESSEE

UNCLASSIFIED

UNCLASSIFIED

ORNL-1879

COPY NO. 3

Contract No. W-7405-eng-26

PHYSICS DIVISION

SEMIANNUAL PROGRESS REPORT

for Period Ending March 20, 1955

A. H. Snell, Director

Edited by
J. L. Fowler and E. O. Wollan
Associate Directors

DATE ISSUED

SEP 15 1955

OAK RIDGE NATIONAL LABORATORY
Operated by
UNION CARBIDE NUCLEAR COMPANY
A Division of Union Carbide and Carbon Corporation
Post Office Box P
Oak Ridge, Tennessee

UNCLASSIFIED

OAK RIDGE NATIONAL LABORATORY LIBRARY
3 4456 0024743 6

INTERNAL DISTRIBUTION

1. C. E. Center
2. Biology Library
3. Health Physics Library
4-6. Central Research Library
7. Reactor Experimental Engineering Library
8-12. Laboratory Records Department
13. Laboratory Records, ORNL R.C.
14. C. E. Larson
15. L. B. Emlet (K-25)
16. J. P. Murray (Y-12)
17. A. M. Weinberg
18. E. H. Taylor
19. E. D. Shipley
20. E. J. Murphy
21. F. C. VonderLage
22. A. H. Snell
23. A. Hollaender
24. J. A. Swartout
25. K. Z. Morgan
26. F. L. Culler
27. M. T. Kelley
28. E. M. King
29. E. O. Wollan
30. D. W. Cardwell
31. A. S. Householder
32. L. D. Roberts
33. R. B. Briggs
34. R. N. Lyon
35. W. C. Koehler
36. E. P. Blizard
37. M. E. Rose
38. G. E. Boyd
39. Lewis Nelson
40. R. W. Stoughton
41. C. E. Winters
42. W. H. Jordan
43. E. C. Campbell
44. D. S. Billington
45. M. A. Bredig
46. R. S. Livingston
47. C. P. Keim
48. F. C. Maienchein
49. C. E. Clifford
50. G. H. Clewett
51. C. D. Susano
52. C. J. Borkowski
53. M. J. Skinner
54. M. K. Wilkinson
55. S. Bernstein
56. P. M. Reyling
57. D. D. Cowen
58. W. M. Good
59. G. C. Williams
60. J. L. Fowler
61. R. W. Johnson
62. J. R. McNally, Jr.
63. J. L. Gabbard
64. C. L. Storrs
65. P. M. Steir
66. R. A. Charpie
67. E. P. Wigner (consultant)
68. H. A. Bethe (consultant)
69. K. Lark-Horovitz (consultant)
70. Eugene Guth (consultant)
71. R. W. Peelle
72. W. M. Breazeale (consultant)
73. E. C. Smith
74. C. G. Shull
75. P. R. Bell
76. G. G. Kelley
77. C. C. Harris
78. H. G. MacPherson (consultant)
79. P. H. Stelson
80. J. E. Sherwood
81. U. H. Bents
82-83. ORNL Document Reference Library, Y-12 Branch
84. W. Zobel
85. R. B. Murray
86. H. B. Willard
87. J. Schenck
88. J. H. Neiler
89. E. D. Klema

EXTERNAL DISTRIBUTION

90. W. G. Pollard, ORINS
91. W. K. H. Panofsky, Stanford University
92. L. C. Biedenharn, Rice Institute
93. R. F. Bacher, California Institute of Technology
94. John Dunning, Columbia University
95. Phillips Petroleum Co., Attn: Librarian
96. R. L. Heath, Phillips Petroleum Company
97. S. DeBenedetti, Carnegie Institute of Technology
98. Massachusetts Institute of Technology, Department of Electrical Engineering
99. A. von Hippel, Laboratory for Insulation Research, MIT
100. M. Goodrich, Louisiana State University
101. Truman S. Grey, Massachusetts Institute of Technology
102. V. C. Wilson, General Electric Co., Schenectady
103. D. S. Hughes, University of Texas
104. E. A. Rollor, ANP Project Office, Fort Worth
105. S. Frankel, Physics Dept., University of Pennsylvania
106. G. Griffith, Westinghouse Research Laboratory, E. Pittsburgh, Pennsylvania
107. F. Allison, Emory and Henry University, Emory, Virginia
108. J. A. Sauer, Physics Dept., Pennsylvania State University
109. J. E. Goldman, Dept. of Physics, Carnegie Institute of Technology
110. R. Stephenson, Dept. of Chemical Engineering, New York University
111. M. Goldhaber, Brookhaven National Laboratory
112. M. N. Saha, c/o Library, Institute of Nuclear Physics, 92 Upper Circular Road, Calcutta, India
113. J. A. Wheeler, Palmer Physical Laboratory, Princeton University
114. R. S. Christy, California Institute of Technology
115. T. J. Turner, Wake Forrest College
116. T. Lauritsen, California Institute of Technology
117. N. F. Ramsey, Harvard University
118. University of Notre Dame (Attention: Library)
119. J. H. Van Vleck, Harvard University
120. Division of Research and Medicine, AEC, ORO

121-459. Given distribution as shown in TID-4500 under Physics Category

Physics Division progress reports previously issued in this series are as follows:

ORNL-325 Supplement	December, January, and February, 1948-1949
ORNL-366	Period Ending June 15, 1949
ORNL-481	Period Ending September 25, 1949
ORNL-577	Period Ending December 15, 1949
ORNL-694	Period Ending March 15, 1950
ORNL-782	Period Ending June 15, 1950
ORNL-865	Period Ending September 20, 1950
ORNL-940	Period Ending December 20, 1950
ORNL-1005	Period Ending March 20, 1951
ORNL-1092	Period Ending June 20, 1951
ORNL-1164	Period Ending September 20, 1951
ORNL-1278	Period Ending December 20, 1951
ORNL-1289	Period Ending March 20, 1952
ORNL-1365	Period Ending June 20, 1952
ORNL-1415	Period Ending September 20, 1952
ORNL-1496	Period Ending December 20, 1952
ORNL-1620	Period Ending September 10, 1953
ORNL-1705	Period Ending March 10, 1954
ORNL-1798	Period Ending September 10, 1954

CONTENTS

PUBLICATIONS vii

PAPERS PRESENTED AT SCIENTIFIC MEETINGS BY MEMBERS OF THE PHYSICS DIVISION vii

ANNOUNCEMENTS ix

SUMMARY 1

1. HIGH-VOLTAGE PHYSICS 4
   - 1.1 Neutron-induced Fission Cross Sections of U^{234} and U^{236} 4
   - 1.2 Total Neutron Cross Section of Fluorine 4
   - 1.3 Elastic Scattering of Neutrons by Lithium 5
   - 1.4 Elastic Scattering of Neutrons from Neon 6
   - 1.5 Angular Distribution of n-p Scattering at 17.9 Mev 7
   - 1.6 Cross Section for Fast-Neutron Excitation of Zr^{90m} 9
   - 1.7 Coulomb Excitation 12
     - 1.7.1 Angular Distributions 12
     - 1.7.2 Gamma-Ray Yields from Cadmium Nuclei 13
   - 1.8 Yield of the Reaction $Si^{28}(p,p'\gamma)Si^{28}$ 15
   - 1.9 Accelerator Energy Calibration and Proton-Neutron Threshold Measurements 15

2. RADIOACTIVITY AND NUCLEAR ISOMERISM 18
   - 2.1 Inner Bremsstrahlung–Gamma-Ray Correlations 18
     - 2.1.1 Tantalum-181 18
     - 2.1.2 Hafnium-177 18
   - 2.2 Decay and Gamma Spectrum of 0.8-sec Zr^{90m} 18
   - 2.3 Half-Life Measurement by Square-Wave Activation 19
   - 2.4 Prompt Fission Gamma Rays 20

3. NEUTRON DIFFRACTION 24
   - 3.1 Magnetic Structure of Uranium Hydride 24
   - 3.2 Magnetic Structure of $MnCl_2$ 27
   - 3.3 A New Structure in the Perovskite-Type Compounds $(La,Ca)MnO_3$ 28
   - 3.4 Ferromagnetic- and Antiferromagnetic-Moment Data for the $[(1-x)La, xCa]MnO_3$ Series of Compounds 31

4. LOW-TEMPERATURE PHYSICS – NUCLEAR ALIGNMENT 34
   - 4.1 Brute-Force Polarization of In^{115} Nuclei 34
   - 4.2 Extension of Molecular-Field Theory to a Hexagonal Lattice 35
   - 4.3 Effect of Crystalline Electric Fields on Antiferromagnetic Transitions 36

5. HEAVY-ION PHYSICS 39
   - 5.1 Electron-Capture and -Loss Cross Sections for Protons in Various Gases 39

6. NEUTRINO RECOIL 44

6.1 Recoil Spectrometry 44
6.1.1 Charge Spectrum of the Recoiling Cl^{37} Atoms 45
6.1.2 Energy of the Recoils 47
6.1.3 Natural Line Widths 47

7. NEUTRON CROSS SECTIONS AND FISSION PHYSICS 50

7.1 Absorption Cross Sections for Long-lived Fission-Product Zr^{93}, Am^{241}, and Enriched Stable Platinum Isotopes 50

7.2 Fission Neutron Spectrum of U^{233} 51

7.3 Energy Spectrum of Gamma Rays Accompanying the Fission of U^{235} 51

8. REACTOR PHYSICS AND SHIELDING 57

8.1 Attenuation of Swimming Pool Reactor Radiations 57
8.1.1 Reactor Description 57
8.1.2 Radiation Detectors 57
8.1.3 Measurements 58
8.1.4 Results 60

8.2 Calibration of Control Rods in the Bulk Shielding Reactor 60
8.2.1 Reactor Loadings 60
8.2.2 Distributed-Poison Calibration Method 61
8.2.3 Inhour Calibration Method 63
8.2.4 Conclusions 63

8.3 Reactivity Changes Due to Beam Holes and Partial Reflectors Adjacent to the Bulk Shielding Reactor 63

9. THEORETICAL PHYSICS 68

9.1 *L*-Shell Internal Conversion Coefficients 68

9.2 *M*-Shell Internal Conversion 68

9.3 Orbital Capture 68
9.3.1 Effect of *L* Capture 69
9.3.2 Effect of Electron Transitions 69
9.3.3 Other Effects 69
9.3.4 Angular Correlation Effects 69

9.4 High-Energy Fixed-Frequency Cyclotron Studies 69

9.5 Theory of Nuclear Forces 70

PUBLICATIONS

R. G. Allen, T. E. Stephenson, C. P. Stanford, and S. Bernstein, "Slow Neutron Cross Sections of Gold, Silver, Indium, Nickel, and Nickel Oxide," *Phys. Rev.* **96**, 1297–1305 (1954).

P. H. Stelson, "Angular Distributions of α Particles from the $Na^{23}(p,\alpha)Ne^{20}$ Reaction," *Phys. Rev.* **96**, 1584–1590 (1954).

J. E. Sherwood, T. E. Stephenson, and S. Bernstein, "Stern-Gerlach Experiment on Polarized Neutrons," *Phys. Rev.* **96**, 1546–1548 (1954).

R. A. Erickson, L. D. Roberts, and J. W. T. Dabbs, "Mutual Inductance Bridge and Cryostat for Low-Temperature Magnetic Measurements," *Rev. Sci. Instr.* **25**, 1178–1182 (1954).

C. D. Moak, W. M. Good, and W. E. Kunz, "Charged Particles from the Bombardment of Li^7 by He^3," *Phys. Rev.* **96**, 1363–1365 (1954).

C. H. Johnson, H. B. Willard, and J. K. Bair, "Total Cross Section of Li^6 for Neutrons," *Phys. Rev.* **96**, 985–988 (1954).

C. P. Stanford, T. E. Stephenson, and S. Bernstein, "Neutron Spin from Magnetic Resonance Experiment," *Phys. Rev.* **96**, 983–984 (1954).

P. M. Stier, C. F. Barnett, and G. E. Evans, "Charge States of Heavy-Ion Beams Passing Through Gases," *Phys. Rev.* **96**, 973–982 (1954).

C. F. Barnett, G. E. Evans, and P. M. Stier, "Characteristics of an Electron Multiplier in the Detection of Positive Ions," *Rev. Sci. Instr.* **25**, 1112–1115 (1954).

L. D. Roberts, S. Bernstein, J. W. T. Dabbs, and C. P. Stanford, "Capture of Polarized Neutrons by Polarized Sm^{149} Nuclei," *Phys. Rev.* **95**, 105–110 (1954).

P. R. Bell, "Scintillation Spectrometer with Improved Response," *Science* **120**, 625–626 (1954).

P. R. Bell, "Spectrometry," *Nucleonics* **12**, 54–55 (1954).

J. Schenck, "Scintillation Counters" (Review of book by J. B. Birks), *Science* **120**, 385 (1954).

H. B. Willard, J. K. Bair, and J. D. Kington, "Polarization of Fast Neutrons from Nuclear Reactions," *Phys. Rev.* **95**, 1359–1360 (1954).

C. G. Shull and M. K. Wilkinson, "Neutron Diffraction Studies of the Magnetic Structure of Alloys of Transition Elements," *Phys. Rev.* **97**, 304–310 (1955).

W. E. Kunz, "Deuterium He^3 Reaction," *Phys. Rev.* **97**, 456–462 (1955).

A. H. Snell, "Nuclear Reactors for Industry and Universities" (Review of book edited by E. H. Wakefield), *Physics Today* **8**, 19–20 (February 1955).

R. L. Macklin and H. E. Banta, "Tritium Production from Lithium by Deuteron Bombardment," *Phys. Rev.* **97**, 753–757 (1955).

A. H. Snell and F. Pleasonton, "Spectrometry of Recoils from Neutrino Emission in Argon-37," *Phys. Rev.* **97**, 246–248 (1955).

M. K. Wilkinson, C. G. Shull, L. D. Roberts, and S. Bernstein, "Some Neutron Diffraction Observations on the Superconducting State," *Phys. Rev.* **97**, 889 (1955).

PAPERS PRESENTED AT SCIENTIFIC MEETINGS BY MEMBERS OF THE PHYSICS DIVISION

American Physical Society Meeting, Baltimore, March 17–19, 1955

C. F. Barnett and P. M. Stier, "Electron Capture Cross Section for Protons."

American Physical Society Meeting, New York City, January 27–29, 1955

E. C. Campbell, R. W. Peelle, F. C. Maienschein, and P. H. Stelson, "Decay and Fast Neutron Excitation of Zr^{90m}."

A. Galonsky and J. Judish, "*n-p* Scattering at 17.9 Mev."

N. H. Lazar and E. D. Klema, "The Decay of Bi^{207}."

R. B. Murray and L. D. Roberts, "Magnetic and Thermal Properties of $MnCl_2$ at Liquid Helium Temperatures."

R. W. Peelle, "Differential Cross Sections for the Scattering of Protons on Carbon as a Function of Incident Proton Energy."

L. D. Roberts and R. B. Murray, "Magnetic and Thermal Properties of UI_3 at Liquid Helium Temperatures."

A. H. Snell and F. Pleasonton, "Magnetic and Electric Deflection Spectrometry of Neutrino Recoils in Argon 37."

P. M. Stier, C. F. Barnett, R. A. Howard, and W. Bugg, "Charge States of Hydrogen Ions in Gases."

T. A. Welton, "On the Possible Convergence of the Mass Renormalization."

H. B. Willard, J. D. Kington, and J. K. Bair, "The $C^{13}(p,\gamma)N^{14}$ Reaction."

L. C. Biedenharn and A. Simon, "Analysis of Angular Distribution Data by Electronic Computers."

Conference on Electronic Techniques (AIEE-IRE-ISA), Chicago, November 10–12, 1954

J. E. Francis and P. R. Bell, "Medical Spectrometer."

Oak Ridge Regional Symposium, Nashville, November 12–13, 1954

A. H. Snell, "Physics Research with a Reactor."

American Physical Society Meeting, Chicago, November 26–27, 1954

P. H. Stelson and F. K. McGowan, "Angular Distribution of Gamma Rays from Coulomb Excitation."

Diffraction Conference, Pittsburgh, November 3–5, 1954

M. K. Wilkinson, N. S. Gingrich, and C. G. Shull, "Magnetic Structure of Mn_2Sb by Single Crystal Neutron Diffraction."

Conference on Ferrimagnetism, U. S. Naval Ordnance Laboratory, White Oak, Md., October 11–12, 1954

W. C. Koehler and E. O. Wollan, "Neutron Diffraction Studies of Magnetic Compounds."

Calorimetry Conference, Schenectady, N.Y., September 17–18, 1954

L. D. Roberts and R. B. Murray, "The Thermal and Magnetic Properties of Anhydrous Manganous Chloride and Uranium Tri-iodide at Liquid Helium Temperatures."

Fourth Oak Ridge Regional Symposium, Duke University, March 11–12, 1955

A. H. Snell, "The Structure of the Atom."

NOTE – The following paper was presented at the Southeastern Section Meeting of the American Physical Society held in Knoxville, Tennessee, April 1–3, 1954, but was not listed in ORNL 1798: P. H. Stelson and E. C. Campbell, "Cross Section for Excitation of Pb^{207m} by Elastic Scattering of Neutrons."

ANNOUNCEMENTS

The following persons have been added to the staff of the Physics Division during this period: J. H. Gibbons, U. H. Bents (ORINS fellow), and H. W. Schmitt (High Voltage); H. Brysk and D. A. Geffen (Theoretical); W. Zobel and R. B. Murray (Shielding); alternate co-op students H. Steiner and S. W. Mosko (Neutron Diffraction); and technicians J. F. Ellis (Critical Experiments) and R. E. Wright and I. D. Conner (Shielding).

H. E. Hungerford (Shielding) transferred to the Aircraft Reactor Engineering Division.

Terminations: None.

PHYSICS DIVISION
SEMIANNUAL PROGRESS REPORT

SUMMARY

HIGH-VOLTAGE PHYSICS

The fission cross sections of U^{234} and U^{236} have been measured in the energy ranges from 4.0 Mev down to their respective thresholds. In both U^{234} and U^{236} the cross section rises to a leveling-off energy in an interval of a few hundred kilovolts. In both isotopes, maxima and minima in cross sections appear as the energy is increased.

The total neutron cross section of fluorine has been studied by employing both an $Li^7(p,n)Be^7$ and an $H^3(p,n)He^3$ neutron source in the energy range 0.5 to 5.0 Mev. Resonances not previously reported were observed at 1.10 and 2.25 Mev, as well as at several energies above 3 Mev.

Neutron elastic-scattering differential cross sections have been obtained at various angles on Li^6 and Li^7. The results obtained confirm that the Li^7 state at 7.46 Mev is $J = 5/2$ formed by p wave and that the Li^8 state formed by 200-kev neutrons on Li^7 is $J = 3$ formed by p wave.

Neutron elastic-scattering angular distributions have been studied in neon as a function of neutron energy. One result of the experiment is the observation of numerous resonances not previously reported. Strong backward scattering was observed for the resonances at 1.38, 1.62, and 1.68 Mev.

The neutron-proton scattering differential cross section has been measured as a function of angle at 17.9 Mev. The results give for the angular distribution the form $[1 + (0.08 \pm 0.03) \cos^2 \theta]$.

Zirconium-90 has a metastable state of 0.83-sec half life. This state has been studied by neutron inelastic scattering on Zr^{90}. By threshold determination of the 0.83-sec activity, the level has been located at 2.35 Mev, and the half life indicates an $E5$ character for the emitted gamma ray, suggesting, though not proving, the 2.3-Mev state to be 5–.

A detailed study has been made of the angular distribution of coulomb-excited gamma radiation in comparison with theory. A smooth dependence on proton energy is observed for the angular-distribution coefficients. However, the observed dependence differs from that predicted by the theory both in shape and in the Z-dependence.

A determination has been made of the excitation curve for the production of the 1.78-Mev $Si^{28}(p,p'\gamma)Si^{28}$ gamma ray. Measured and tabulated are the resonances corresponding to states in P^{29}.

It has been found that, because of a combination of probe location and saturation effects in the iron of the analyzer magnet, there is not strictly a linear relation between proton momentum and frequency of a proton-moment fluxmeter. Numerous (p,n) thresholds have been remeasured on the basis of an accurately determined relationship between proton momentum and frequency of a proton-moment fluxmeter.

RADIOACTIVITY AND NUCLEAR ISOMERISM

An attempt has been made to measure the inner bremsstrahlung–gamma ray directional angular correlation. During the work it has been shown by Brysk and Rose that in nearly all cases this correlation is isotropic, and no knowledge of the nuclear levels can be obtained. The angular correlations of gamma rays in cascade have been measured for certain excited states in Ta^{181} and Hf^{177}.

Half-life and gamma-energy measurements are presented for an isomer Zr^{90m} produced by inelastic scattering of neutrons on zirconium.

A method is proposed for measuring half lives of nuclear isomers by means of a pulse-activation technique.

An investigation of the U^{235} prompt fission gamma rays in coincidence with the fission fragments has been completed. The coincidence pulse-height spectra indicate a continuous gamma-ray spectrum with an average of 7.51 prompt gamma rays per fission with a total energy of 7.46 Mev. The observed gamma-ray distribution decreases exponentially from the lowest energy measured to approximately 7.5 Mev.

NEUTRON DIFFRACTION

The ferromagnetic scattering properties of UD_3 and UH_3 have been studied over a wide range of temperatures, and from the angular distribution of the scattered neutrons, information on the ionic state of the uranium atom is obtained.

Preliminary experiments have been carried out on both polycrystalline and single-crystal samples of $MnCl_2$ in order to establish the magnetic structure which develops at temperatures near 2°K.

A new antiferromagnetic structure has been observed in the manganite series of compounds. This structure, although more complicated than the structures previously observed, fits well into the general scheme of structure types proposed for this series, and it is in excellent accord with recently proposed theoretical coupling criteria.

The correlation with composition of the observed coherent moments associated with these compounds is plotted and discussed.

LOW TEMPERATURES AND NUCLEAR ALIGNMENT

Indium-115 nuclei have been polarized by the application of a field of 11,150 gauss directly to the nuclear-spin system at a temperature of 0.043°K. This nuclear polarization was observed through the change produced in the thermal capture cross section for polarized neutrons and established $J = I + \frac{1}{2} = 5$ for the 1.458-ev level.

The molecular-field theory of antiferromagnetism has been extended to the case of a hexagonal lattice, and the effect of a simple type of electric-field splitting on the antiferromagnetic transition temperature has been investigated.

HEAVY-ION PHYSICS

Curves are given of the fraction of a hydrogen beam which has charge −1, 0, and +1 after passage through sufficient gas for equilibrium to be established between competing electron-capture and -loss reactions. The cross sections for a neutral hydrogen atom to become ionized (either negatively or positively) is reported. The energy range studied was from 3 to 30 kev, and the target gasses were hydrogen, helium, nitrogen, oxygen, neon, and argon. Good agreement is obtained between these results and the previously reported work at higher energies.

Electron-capture cross sections have been measured for protons in the energy range 20 to 200 kev. These are in excellent agreement with cross sections computed from the previously reported electron-loss cross sections and ratio of electron-loss to -capture cross sections.

NEUTRINO RECOIL

The recoils which result from neutrino emission in the electron-capture decay of A^{37} are found to have an energy of 9.6 ± 0.2 ev, which is in excellent agreement with the energy to be expected from emission of a single neutrino with the known transition energy of 816 kev. The charge spectrum of the recoiling ions has been accurately measured out to seven charges. The natural half-width of the charge-1 recoil line has been found to be slightly less than 1.8 ev; it is thought that this may be purely the thermal width, because selection of the charge-1 recoils may exclude contributions to the line width as the result of ejection of the most energetic Auger electrons.

NEUTRON CROSS SECTIONS AND FISSION PHYSICS

Absorption cross sections have been determined for the long-lived fission-product Zr^{93}, Am^{241}, and enriched stable platinum isotopes.

The fission neutron spectrum of U^{233} was measured at the Bulk Shielding Facility with the proton-recoil neutron spectrometer for the energy region between 1.3 and 10 Mev.

Preliminary measurements have been made of the gamma spectrum for U^{233} fission for the energy interval between 0.5 and 2.3 Mev. The results for this interval indicate 5.0 photons/fission for a total energy of 5.1 Mev/fission.

REACTOR PHYSICS AND SHIELDING

The attenuation, by water, of the gamma-ray dose rate and the thermal-neutron flux from the Bulk Shielding Reactor has been measured out to distances of 770 and 470 cm, respectively. It was found that beyond a distance of 200 cm from the reactor the slopes of plots of the two measurements are similar, which indicates that essentially all neutrons in this region are photoneutrons produced by gamma rays in the naturally occurring deuterium in the pool water. With the photoneutrons subtracted, the true thermal-neutron attenuation curve is exponential with a relaxation length that varies between 6 and 9 cm over a reduction of 10^{10}.

The regulating and safety rods of the BSR have been calibrated by two methods for several reactor loadings with reflectors of water, beryllium oxide,

and combinations of the two. The results of these measurements are presented.

Two BSR loadings were used in a determination of the effects on the BSR reactivity of placing beam holes and partial reflectors adjacent to the BSR. The beam holes consisted of cylinders of various diameters and lengths placed against the reactor in one case and against the BeO reflector in another.

THEORETICAL PHYSICS

Work on the program of calculation of internal conversion coefficients is reported. Considerable progress has been made on the L-shell work. The need for M-shell coefficients has given rise to an extension of the program in this direction, and the formulation and programing of this problem have been completed.

A comprehensive study of orbital capture has been carried out. All theoretical results of interest to the experimentalist have been re-examined, extended, and collected.

A rather general Oracle code has been constructed, tested, and used for determining the stability of proton orbits in fixed-frequency high-energy cyclotrons. Fairly complete data on magnetic fields, orbit radii, and focusing frequencies have been obtained for a number of cyclotrons with field patterns which repeat in various fractions of a revolution and which spiral at various pitches. A 1-Bev machine of this type appears to be feasible.

A computational procedure has been devised for obtaining the essential results of pseudoscalar meson theory, without dependence on perturbation theory.

1. HIGH-VOLTAGE PHYSICS

1.1 NEUTRON-INDUCED FISSION CROSS SECTIONS OF U^{234} AND U^{236}

R. W. Lamphere R. E. Greene

The fission cross sections of the uranium isotopes, 234 and 236, have been measured from their thresholds to 4.0-Mev neutron energy by use of neutrons from the $H^3(p,n)He^3$ reaction. The neutron energy spread varied from 60 to 100 kev for most points. A large number of points were taken in order to establish the shapes of the cross-section curves as well as possible.

Uranium-234 has a threshold at 360 kev; its cross section rises to 1.24 barns at 850 kev, dips to 1.08 barns at 1.06 Mev, rises to 1.47 barns at 1.9 Mev, dips to 1.40 barns at 2.4 Mev, and then rises to 1.55 barns at 4.0 Mev. Variations in between these points appear smooth with the energy spread present in the neutron beam.

Similarly, U^{236} has a threshold at about 700 kev; its cross section rises to 0.36 barn at 970 kev and remains nearly constant to 1.04 Mev, where the cross section again rises, reaching 0.75 barn at 1.40 Mev, then falls to 0.66 barn at 1.56 Mev, rises to 0.89 barn at 2.5 Mev, falls to 0.87 barn at 2.7 Mev, and then rises to 0.99 barn at 4.0 Mev.

These results are shown in Fig. 1.1, and they are believed to be accurate to within 4%.

1.2 TOTAL NEUTRON CROSS SECTION OF FLUORINE

J. E Wills H. B. Willard

The total neutron cross section of F^{19} has been remeasured[1] for neutron energies between 0.5 and

[1]Neutron Cross Section Advisory Group, *Neutron Cross Sections*, AECU-2040 (May 15, 1952).

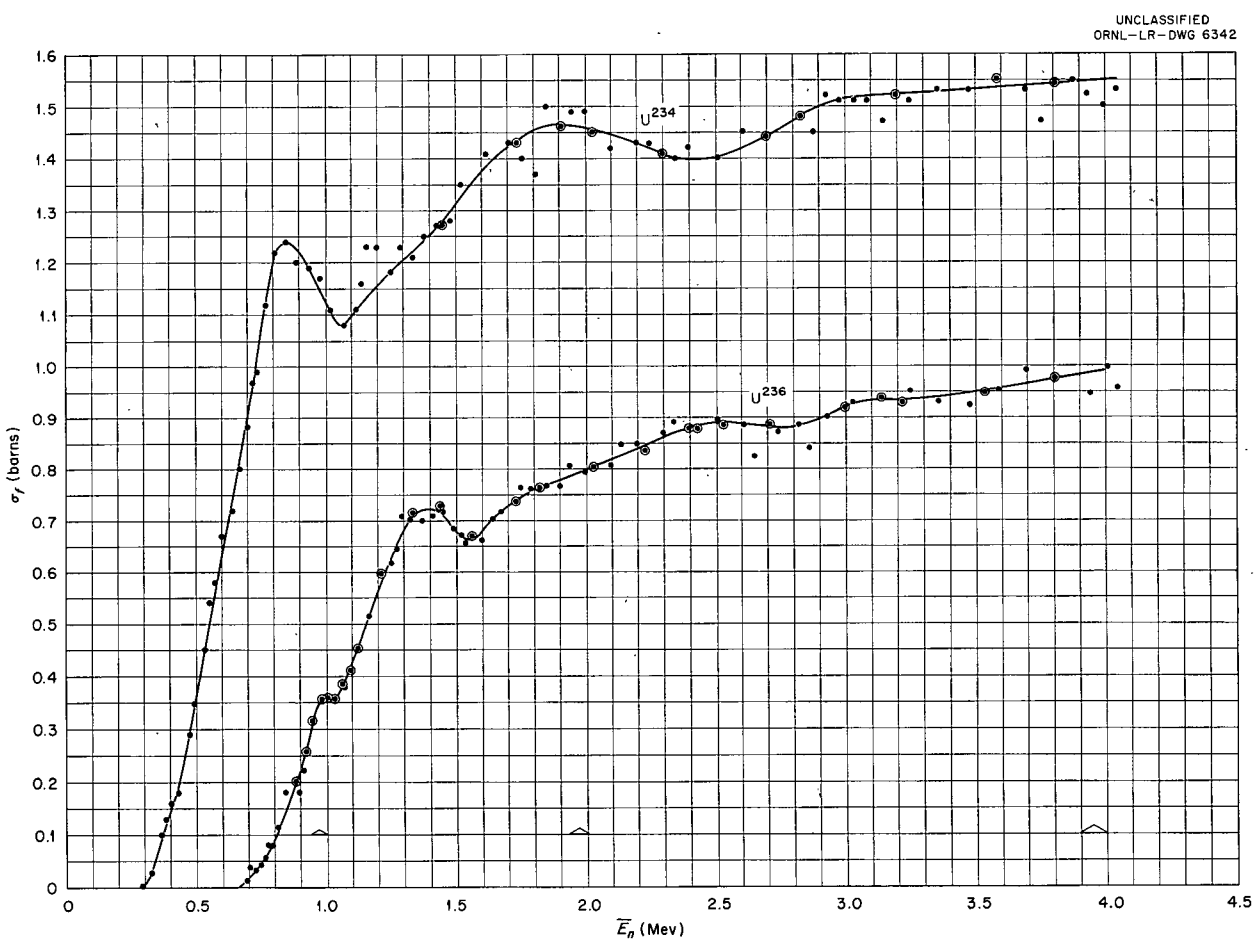

Fig. 1.1. Fission Cross Sections of U^{234} and U^{236} as a Function of Neutron Energy.

5 Mev. One set of measurements was made with an energy resolution of about 70 kev and a statistical precision of about ±0.07 barn. Two sets of measurements were made with a resolution of about 20 kev and a precision of about ±0.15 barn. A standard transmission technique was employed. The experimental geometry was such that corrections for finite size of counter and scatterer were negligible.

For the first set of measurements, the $Li^7(p,n)Be^7$ reaction served as a source of neutrons. For the subsequent determinations, the neutrons were furnished by the $H^3(p,n)He^3$ reaction. Protons resolved in energy to about 0.1% were provided by the 5.5-Mv Van de Graaff. The neutrons were detected with a propane-filled recoil counter biased against gamma radiation.

The results are shown in Fig. 1.2. The levels at 1.10 and 2.25 Mev, as well as all levels above 3 Mev, have not been previously reported.

1.3 ELASTIC SCATTERING OF NEUTRONS BY LITHIUM

H. B. Willard
J. K. Bair
H. O. Cohn
J. D. Kington

Angular distributions of neutrons scattered elastically by Li^6 and Li^7 have been measured in the region of 200 to 500 kev by the technique described previously.[2]

Results for Li^6 shown in Fig. 1.3 are in good

[2] H. B. Willard, J. K. Bair, and J. D. Kington, *Phys. Semiann. Prog. Rep. Sept. 10, 1953*, ORNL-1620, p 5.

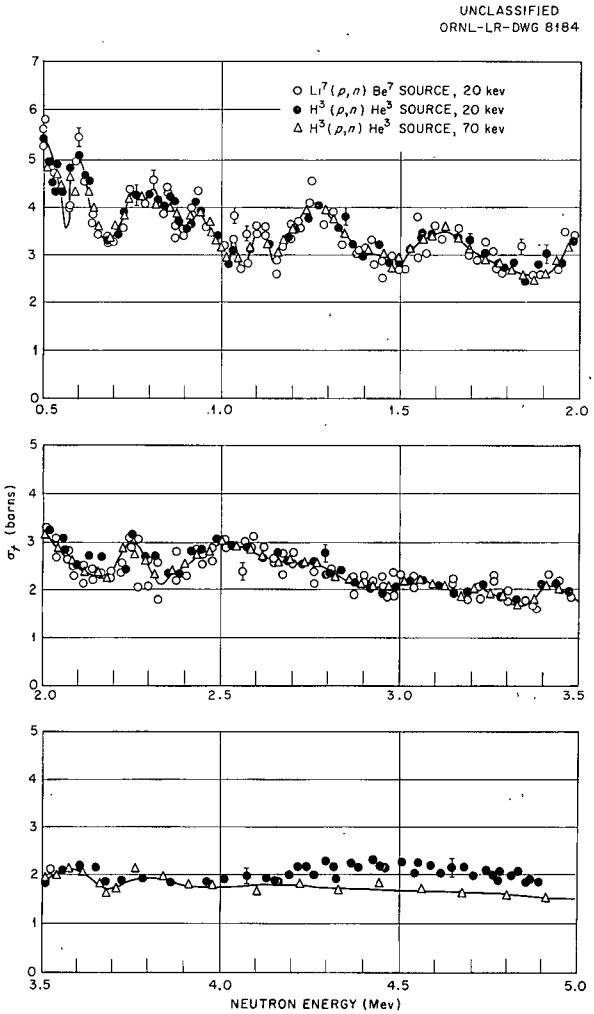

Fig. 1.2. Total Neutron Cross Section of Fluorine.

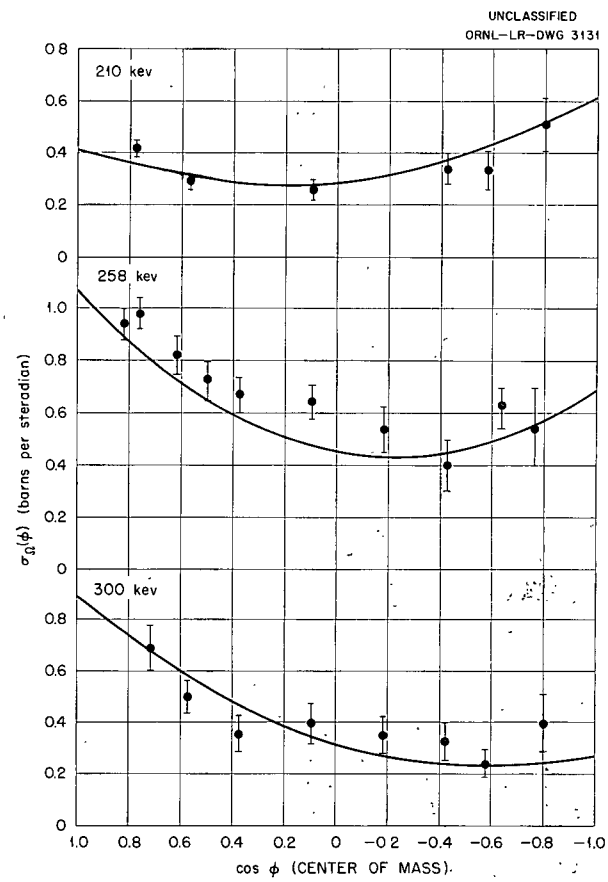

Fig. 1.3. Angular Distribution of Neutrons Elastically Scattered by Li^6.

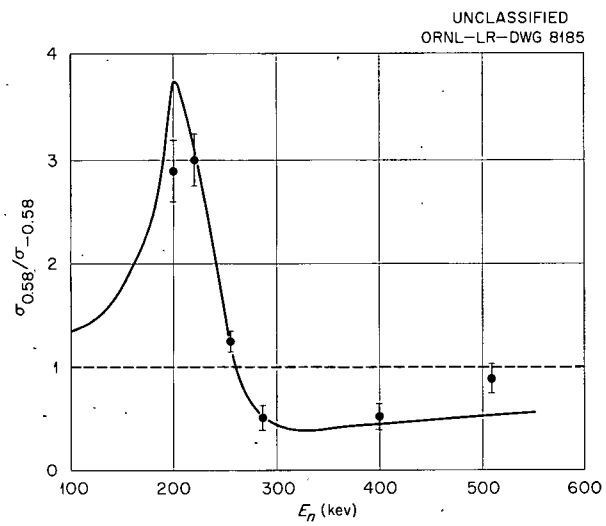

Fig. 1.4. The Ratio $\sigma(\cos\theta = 0.58)/\sigma(\cos\theta = -0.58)$ as a Function of Neutron Energy on Li^7.

agreement[3] with theory for the p-wave formation of a $J = \frac{5}{2}$ level in Li^7 at 7.46 Mev.

In order to detect the strong interference term between the s-wave potential scattering and p-wave resonance scattering by Li^7, the ratio of $\sigma_{C.M.}$ ($\cos\theta = 0.58$) to $\sigma_{C.M.}$ ($\cos\theta = -0.58$) was measured as a function of neutron energy. Results shown in Fig. 1.4 are in good agreement with theoretical results calculated on the assumption that the level is $J = 3$ and that it interferes with the s-wave potential scattering which has a statistical channel spin mixture.

1.4 ELASTIC SCATTERING OF NEUTRONS FROM NEON

H. O. Cohn J. L. Fowler

The technique of pulse-height analysis of nuclear recoils in a proportional counter has been used for

[3] C. H. Johnson, H. B. Willard, and J. K. Bair, *Phy Rev.* 96, 985 (1954).

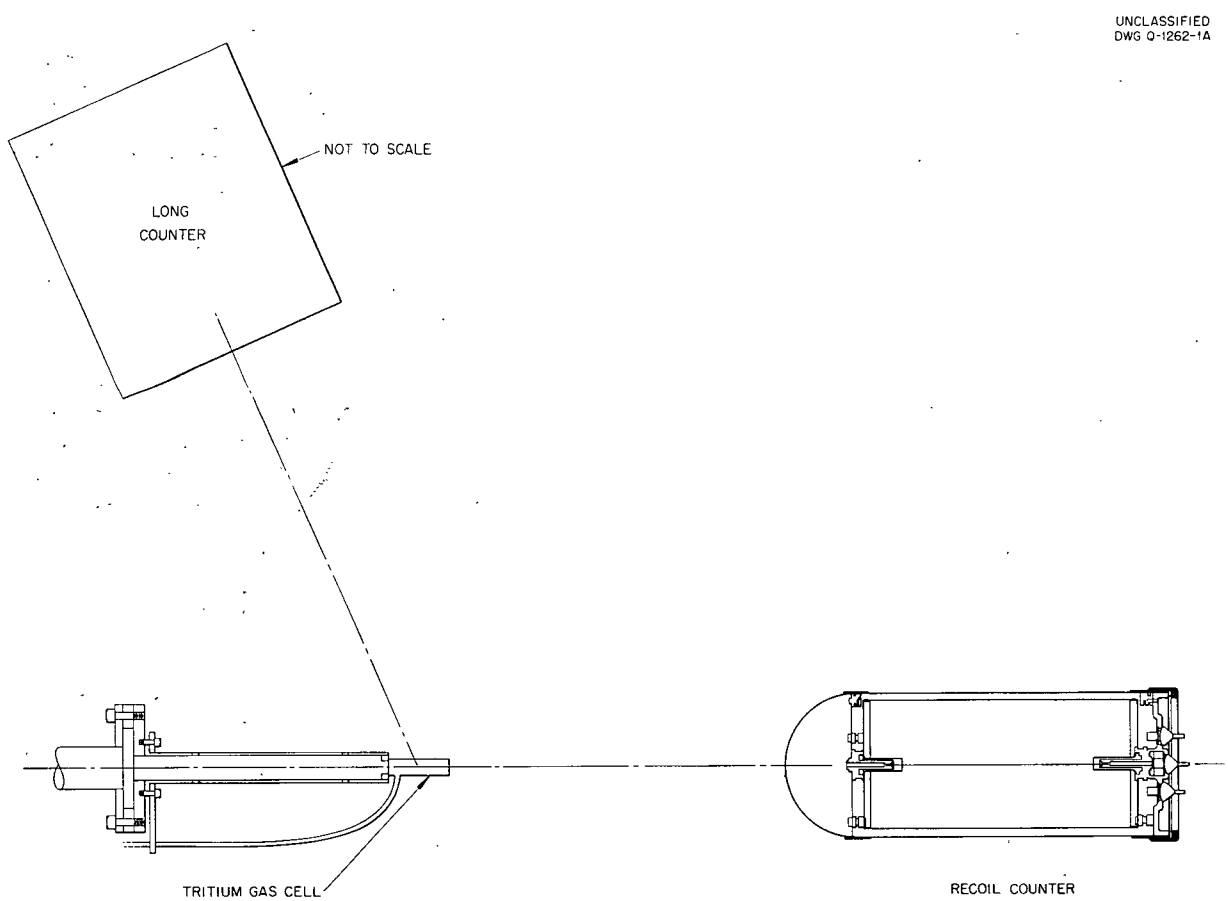

Fig. 1.5. Experimental Setup for Neon Recoil Counter.

a preliminary study of the scattering of neutrons from neon of natural abundance in the energy region 0.8 to 1.7 Mev. Monoenergetic neutrons were produced by bombarding a zirconium tritide target with analyzed protons from the 5.5-Mv electrostatic generator. The neutron energy resolution at 1-Mev neutron energy determined by the rise at threshold of the yield from the tritium target was 9 kev. The proportional counter,[4] shown in Fig. 1.5, was filled to 2 atm with purified neon gas to which was added 2% CO_2. The neutrons were monitored with a long counter, also shown in Fig. 1.5. With low bias settings, the integral counts (Fig. 1.6, right side) show up prominent resonances at neutron energies (±0.01 Mev) of 0.91, 1.31, 1.38, 1.62, and 1.68 Mev. Previously reported resonances in this energy range found from alpha groups by study of the $Ne^{20}(n,\alpha)O^{17}$ reaction[5] are at 1.44 and 1.59 Mev (with fairly large error); the $Ne^{20}(d,p)Ne^{21}$ reaction[6] gave a value of 1.60 ± 0.06 Mev.

[4] J. L. Fowler, C. H. Johnson, and J. R. Risser, *Phys. Rev.* 91, 441A (1953).

[5] G. v. Gierke, *Z. Naturforsch.* 9a, 164 (1954).

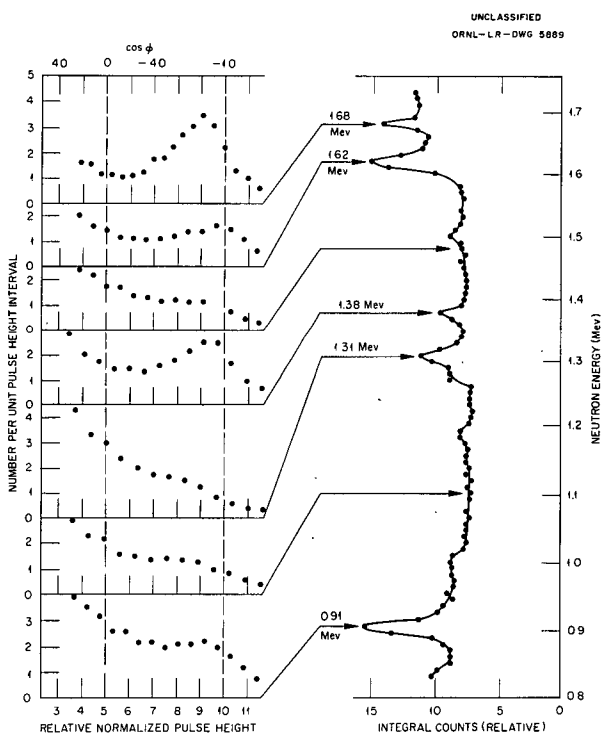

Fig. 1.6. Pulse-Height Distribution for Ne^{20}.

Some of the nuclear-recoil-energy spectra determined by analyzing the amplified recoil pulses from the proportional counter with a 20-channel pulse-height analyzer are shown on the left side of Fig. 1.6. The arrows indicate the energy at which the spectrum was measured. In the absence of inelastic scattering the angular distribution of elastic scattering of neutrons can be deduced from the energy distribution of recoil nuclei.[7,8] The energy of the recoil nucleus is proportional to $(1 - \cos\phi)$, where ϕ is the neutron scattering angle in the center-of-mass system. In this system the number of recoils in the energy interval ΔE is proportional to the differential scattering cross section times the interval $\Delta \cos\phi$. In Fig. 1.6 the upper edge of the recoil-energy distribution has been adjusted to correspond to $\cos\phi = -1$, and the energy scale is labeled also as $\cos\phi$. The lower energy portion of the recoil-energy spectrum is very distorted; an approximate interpretation can be made only for large-angle neutron scattering, >90 deg. As can be seen from Fig. 1.6, this upper portion of the recoil spectra indicates that the three higher energy resonances are characterized by increased backward scattering of neutrons. It is to be noted that under the above conditions it is more likely for energy resonances characterized by backward-scattered neutrons to show up as prominent peaks in the total counts vs E_n curve, whereas resonances not having this characteristic may be depressed.

An experiment is being devised to detect the scattered neutrons with a scintillator in coincidence with the neon nuclear recoil. Here, the neon recoil will be used only as an indication that scattering has taken place; the differential scattering cross section will be determined by the neutron-detecting scintillator.

1.5 ANGULAR DISTRIBUTION OF *n-p* SCATTERING AT 17.9 Mev

A. Galonsky J. P. Judish

There have been several measurements of the *n-p* scattering angular distribution with neutrons in the region of 14 Mev. The best value of $\sigma(180°)/\sigma(90°)$ is 1.05 ± 0.02. At 27 Mev the effect is much

[6] R. Middleton and C. T. Tai, *Proc. Phys. Soc. (London)* 64A, 801 (1951).

[7] E. Baldinger, P. Huber, and H. Staub, *Helv. Phys. Acta* 11, 245 (1938).

[8] H. H. Barschall and M. H. Kanner, *Phys. Rev.* 58, 590 (1940).

larger,[9] namely, 1.28 ± 0.10. The only previous measurement between 14 and 27 Mev gave the inconclusive result[10] $\sigma(150°)/\sigma(90°) = 1.06 \pm 0.16$ for neutrons between 18 and 21 Mev. The value found in this experiment for $\sigma(180°)/\sigma(90°)$ is 1.08 ± 0.03 for 17.9-Mev neutrons.

Deuterons accelerated to 1.96 Mev by the 2.5-Mv electrostatic generator entered a 1.5-in.-long tritium gas target through a 0.05-mil nickel foil. The deuteron energy in the tritium target was 1.7 ± 0.1 Mev. Hence the neutrons produced at 0 deg in the $H^3(d,n)He^4$ reaction had energies of 17.9 ± 0.1 Mev. A very stable, long propane recoil counter biased above *d-d* neutrons was the neutron-flux monitor.

The *n-p* angular distribution was obtained by counting with a triple-coincidence telescope[11] the number of protons ejected from a polyethylene radiator as a function of angle made with the 17.9-Mev neutrons incident on the radiator. The proton counts were normalized to the propane-monitor counts, and at least six runs were made at each of ten angles from 0 to 45 deg.

Figure 1.7 shows the tritium gas target, the polyethylene radiator, the two proportional counters, and the NaI spectrometer. The thickness of the NaI crystal, 2.5 mm, is sufficient to stop a 20-Mev proton. To adjust for the longer rise time of the proportional-counter pulses, the NaI pulses were delayed by the proper time before entering the coincidence circuit. Since the proton energy loss was only about 1% in each proportional counter, the triple-coincidence spectra were very broad – in qualitative agreement with the Symon-Landau theory.[12] At each angle the NaI coincidence spectrum had a peak less than 25% wide at half-maximum and a small, low-energy tail caused by coulomb scattering of the protons in the telescope. The noncoincidence counting rates of the three detectors were so low and so nearly constant with angle that corrections for accidental coincidences and deadtime were negligible. Backgrounds varied from 1% at 0 deg to 50% at 45 deg.

Aside from radiator thickness, the angular resolution of the system, ±3 deg, was the major factor

[9] J. E. Brolley, Jr., J. H. Coon, and J. L. Fowler, *Phys. Rev.* 82, 190 (1951).

[10] E. M. Baldwin, *Phys. Rev.* 83, 495 (1951).

[11] C. C. Trail and C. H. Johnson, *Phys. Semiann. Prog. Rep. Sept. 10, 1954*, ORNL-1798, p 8.

[12] B. B. Rossi, *High Energy Particles*, p 29 ff., Prentice-Hall, New York, 1952.

UNCLASSIFIED
ORNL-LR-DWG 3038B

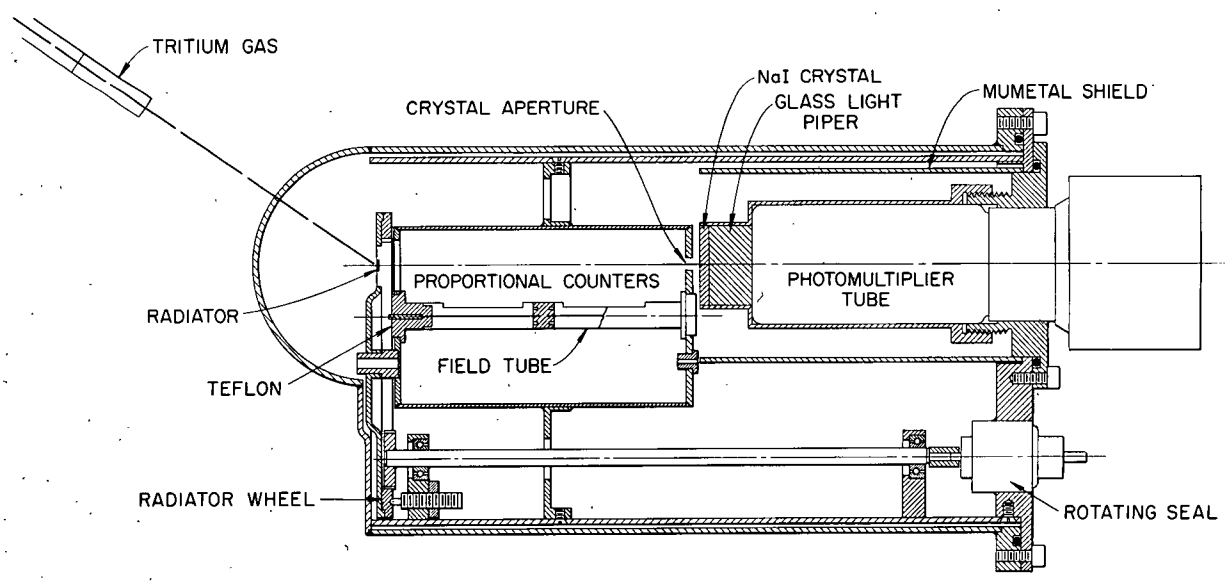

Fig. 1.7. The $H^3(d,n)He^4$ Neutron Source, Radiator, and Triple-Coincidence Telescope Detector (Approximately to Scale).

in broadening the NaI peaks. Since $E_p = E_n \cos^2 \theta$, where E_p and E_n are the recoil proton and incident neutron energies, respectively, it is unimportant (for the proton spectra) to have good angular resolution near 0 deg, but it is very important at large angles. An increased efficiency without sacrifice of energy resolution was achieved by the well-known device of using a rectangular rather than a circular radiator and NaI aperature. For the dimensions chosen for both radiator and aperature, 0.2 × 0.4 in., the angular acceptance is not appreciably increased, except for angles less than about 10 deg, where the proton energy is almost constant with angle.

Since three different radiators, 0.003, 0.008, and 0.016 in. thick, were used in this experiment, it was necessary to have an accurate comparison of their weights. Each radiator was cut into a 0.2 × 0.4 in. rectangle, weighed on a microbalance, and then made to stick to a ¾-in. tantalum disk by gentle heating on a hotplate. Each tantalum disk was then mounted on a radiator wheel inside the telescope. The number of hydrogen atoms is directly proportional to the weight. No area measurements are required, and no assumption need be made as to the uniformity in thickness of the polyethylene foils. This method also eliminates the usual slit in front of the radiator.

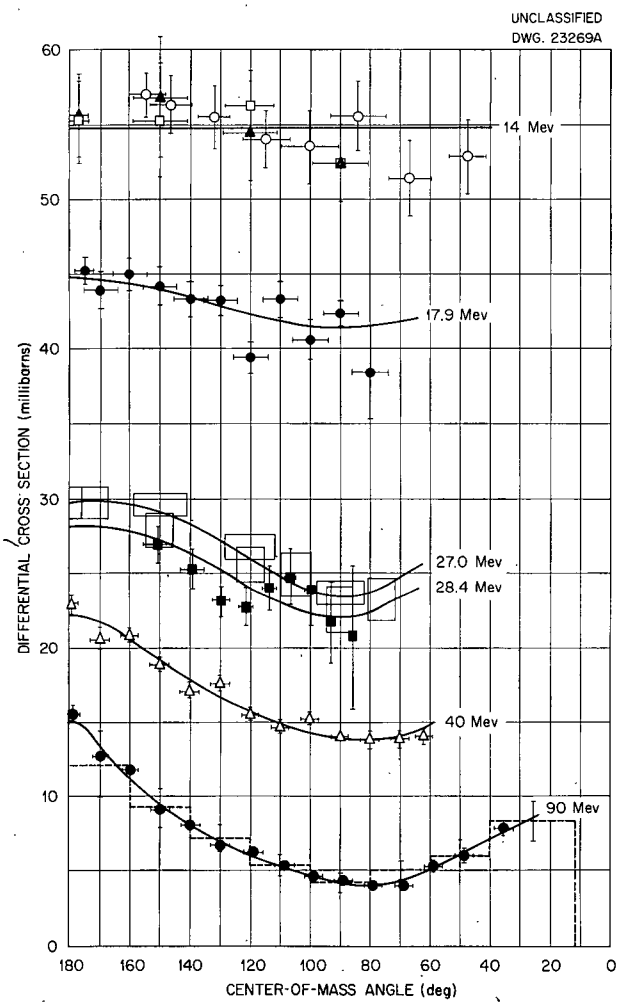

Fig. 1.8. Angular Distributions for *n-p* Scattering.

The results of this experiment for 17.9-Mev neutrons are shown in Fig. 1.8, along with measurements compiled by J. L. Fowler for other neutron energies. The relative yields measured here were normalized to the known total cross section, 535 millibarns. Of the three functions, $\sigma(\theta)$ proportional to 1, $1 + k \cos \theta$, and $1 + k \cos^2 \theta$, the best least-squares fit is $1 + (0.08 \pm 0.03) \cos^2 \theta$, although $1 + (0.08 \pm 0.04) \cos \theta$ is also a good fit. The solid curve in Fig. 1.8 for 17.9 Mev is $1 + 0.08 \cos^2 \theta$.

1.6 CROSS SECTION FOR FAST-NEUTRON EXCITATION OF Zr^{90m}

E. C. Campbell P. H. Stelson

To identify the nuclear reaction responsible for producing the 0.83 ± 0.03 sec activity (see Sec. 2.2) in Zr^{90} and to study it in more detail, we used monoenergetic neutrons from the ORNL 5.5-Mv electrostatic accelerator. The neutrons were produced by the $H^3(p,n)$ reaction in a tritium gas target. An electronic timer and an electrostatic proton-beam deflector provided a repetitive cycle for short neutron bombardment and gamma counting of the zirconium target. Details of the target assembly and of the timing cycle are given in Fig. 1.9. The neutron intensity was monitored by a long counter at an angle of 60 deg to the beam. Anthracene rather than NaI was used as a scintillation detector in order to avoid background associated with neutron activation of the phosphor. The cross section was obtained from the observed ratio of anthracene counts to counts in the neutron monitor. This involved correction for the angular distribution of neutrons from the $H^3(p,n)$ reaction, attenuation of gamma rays produced in the zirconium, and efficiency of the anthracene detector for the particular geometry employed. It is judged from a consideration of the systematic errors in the calibration procedure that the error in the absolute

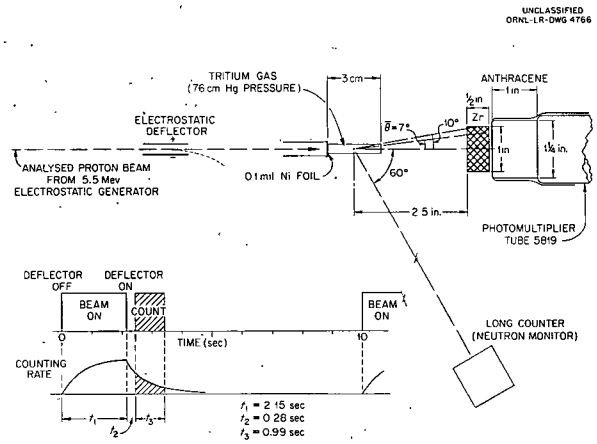

Fig. 1.9. Target Assembly and Timing Cycle - $Zr^{90}(n,n')Zr^{90m}$ (0.83 sec).

cross section could be as high as 40%, while the relative cross sections are probably accurate to within 5%.

By keeping the neutron energy fixed at 3.02 Mev and by varying the counting delay time t_2, the decay curve shown in Fig. 1.10 was obtained. The agreement with the previous result is satisfactory and gives assurance that the activity studied in this way is the same as that found with neutrons in the reactor.

The curve showing the cross section for the production of the 0.8-sec activity as a function of neutron energy is given in Fig. 1.11. The threshold observed at 2.3 Mev is taken as strong evidence that the activity is due to an isomer of Zr^{90} produced by inelastic scattering of neutrons on Zr^{90}, that is, $Zr^{90}(n,n')Zr^{90m}$. The small peak in the cross-section curve at 3.2 Mev is thought to be due to the slight decrease of sensitivity of the long counter as the result of a resonance in the neutron scattering cross section of carbon (contained in the paraffin shielding of the counter) at 2.1 Mev, the energy of the neutrons emitted at 60 deg.

The existence of a metastable state of Zr^{90} is of particular interest theoretically, since Zr^{90} is an even-even nucleus and contains a closed neutron shell (N = 50) and a closed proton subshell (Z = 40). The observed half life and energy point to a high multipole order for the radiation emitted and, therefore, a high spin for the isomeric state, since the ground state is expected to be 0^+.

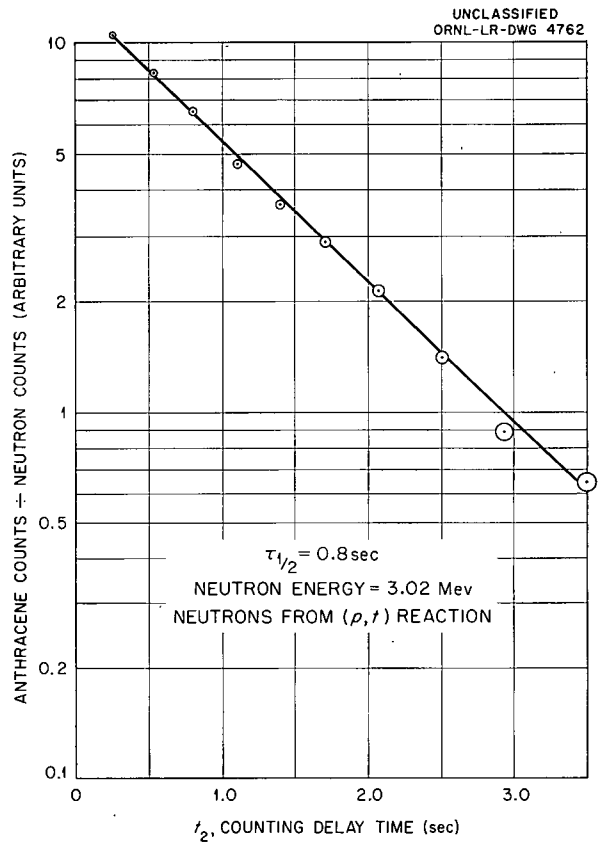

Fig. 1.10. Decay of Zr^{90m}.

If we calculate the expected half life of the 2.3-Mev excited state from the approximate formulas of Weisskop, we obtain for $M4$, 0.004 sec; for $E5$, 3 sec; and for $M5$, 320 sec. Comparison with the experimental half life of 0.83 sec would lead, on this basis, to an $E5$ assignment and an assignment of 5– for the spin and parity of the excited state. Such a conclusion should be made with considerable caution, since there is now considerable experimental evidence that transition probabilities from excited states differ in some cases by a few orders of magnitude from those predicted by the theory. It is found, however, that $M4$ transitions agree rather better with the theory than others, and, for this reason, it is probable that one can exclude $M4$ from consideration.

To obtain further information on this point, a comparison was made of the experimental cross-section curve near the threshold with that predicted by the theory of inelastic neutron scattering

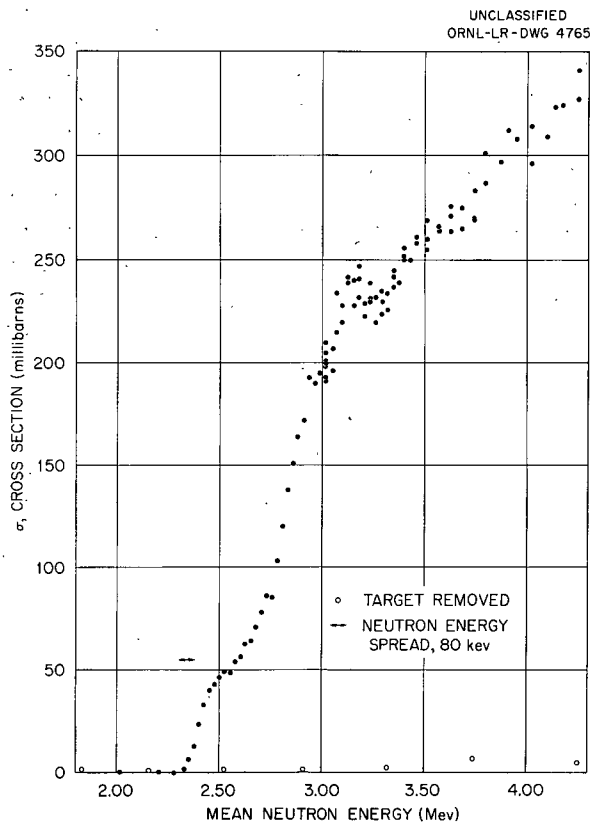

Fig. 1.11. Cross Section of $Zr^{90}(n,n')Zr^{90m}$ (0.8 sec).

by Hauser and Feshbach.[13] They showed that if one assumes a statistical model for the compound nucleus but not for the residual nucleus, then the cross section for inelastic scattering is dependent on the spins and parities of the excited states in which the residual nucleus is left after neutron emission from the compound nucleus. The cross-section calculation involves a summing of the products of neutron penetrabilities for the incoming and outgoing neutrons over all J values of the compound nucleus (consistent with conservation of angular momentum and parity) and over all states of the residual nucleus, which are assumed to have a specified spin and parity. It is further assumed that gamma-ray competition to the ground state of the compound nucleus [resulting in a fast (n,γ) reaction] may be neglected. In the particular case considered, it is expected that this assumption is valid, since it has been demonstrated that the fast-neutron capture cross sections are abnormally low (~ 1 millibarn) for nuclei with closed neutron shells. Furthermore, it is reasonable to suppose that, in this process, states of low spin in the compound nucleus would be excited rather than high-spin states, which are important for the inelastic scattering leading to the isomeric level.

The comparison is shown in Fig. 1.12. Here, the theoretical curves were folded into a trapezoidal resolution function having the calculated full width at half maximum of 80 kev. This neutron energy spread is due to straggling of protons in the 0.1-mil nickel foil at the entrance to the tritium gas target, to the thickness of the target, and to the dependence of neutron energy on emission angle. These "smeared" curves are shown in the figure as solid lines labeled with the assumed designation of the isomeric state.

The plot was made semilogarithmic in order to

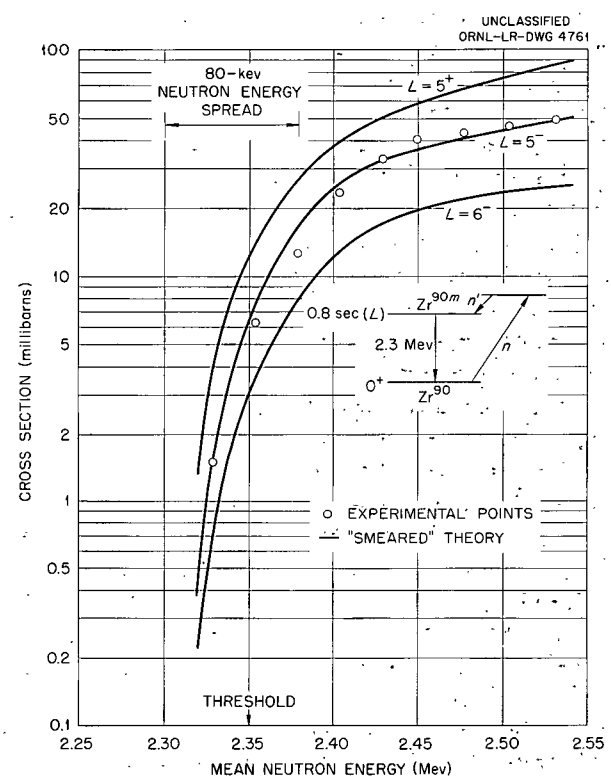

Fig. 1.12. Comparison of Experimental Cross-Section Values of $Zr^{90}(n,n')Zr^{90m}$ with Theoretical Curves.

[13] W. Hauser and H. Feshbach, *Phys. Rev.* 87, 366 (1952).

show that the *shape* of the cross-section curve is determined principally by the resolution function near threshold. Any choice between a 5+, 5−, and 6− conclusion must therefore be made on the basis of the *magnitude* of the cross section. While it seems unlikely that the experimental cross section could be in error by as much as a factor of 2, we cannot yet definitely exclude any of the three values. It is to be noted that the 5− assignment is also preferred from transition probability considerations.

It seems probable that the isomeric state is associated with the excitation of a single proton from the 40 subshell rather than with a more tightly bound neutron from the closed neutron shell ($N = 50$). A possible explanation of the occurrence of a highly excited 5− level lies in the promotion of a $p_{1/2}$ proton into a $g_{9/2}$ state.

1.7 COULOMB EXCITATION

P. H. Stelson F. K. McGowan

1.7.1 Angular Distributions

To test further the semiclassical theory of angular distribution of gamma rays following coulomb excitation given by Alder and Winther,[14] we have carried out measurements on the 555-kev gamma ray in Cd^{114}. The thick target of Cd^{114} was prepared by electrodeposition of a sample enriched to 94.2% in Cd^{114} onto nickel. In order to compare experimental angular distribution coefficients for a thick target with theory, we must evaluate the expected thick-target coefficients. These coefficients are deduced from the total excitation cross section and the thin-target angular distribution coefficients as given by the numerical calculations of Alder and Winther. According to their numerical calculations and for cases of practical interest, it follows that the thick-target energy coefficients $[a_\nu(\xi_i)]_t$ vs ξ_i will be nearly a unique function. To put it differently, if many different cases are measured, one would expect the resulting points $a_\nu(\xi_i)_{exp}$ to fall on a smooth curve as a function of ξ_i, where ξ_i is the value of the parameter ξ corresponding to the incident proton energy on the thick target.

A comparison between theory and experiment is shown in Figs. 1.13 and 1.14, which also include data previously reported.[15] For the medium-weight nuclei, the deviations of the observed energy-dependent coefficients from theory for a thick target are larger than they are for the heavy nuclei. The question might arise as to what effect the multiple Rutherford scattering of the protons as they traverse a thick target would have on the observed energy-dependent coefficients. The problem of the effect of multiple scattering on the proton-gamma angular distribution is similar to the problem of the effect of scattering of electrons in a conversion electron-gamma angular distribution.[16] The form of the correlation is unchanged, and each coefficient $a_\nu A_\nu$ is multiplied by an attenuation factor G_ν. We have evaluated the attenuation

[14] K. Alder and A. Winther, *Phys. Rev.* 91, 1578 (1953); 96, 237 (1954).

[15] P. H. Stelson and F. K. McGowan, *Phys. Semiann. Prog. Rep. Sept. 10, 1954*, ORNL-1798, p 14.

[16] S. Frankel, *Phys. Rev.* 83, 673 (1951).

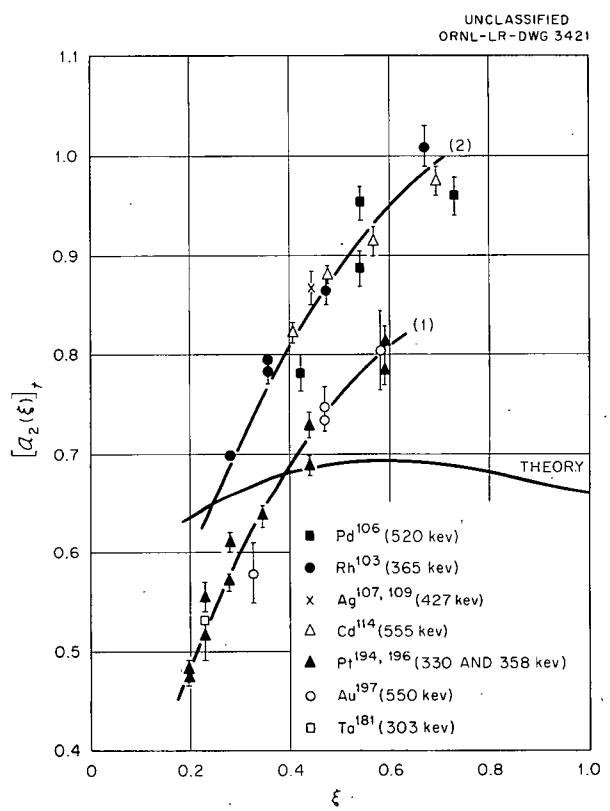

Fig. 1.13. Thick-Target Energy-dependent Coefficient $a_2(\xi)$ Deduced from Angular-Distribution Measurements Plotted at a Value of ξ Corresponding to the Incident-Proton Energy on the Thick Target. The solid curve labeled "theory" represents the thick-target energy-dependent coefficient $[a_2(\xi_i)]_t$.

factors G_ν for a thick target and for the case when $a_\nu(\xi)$ is constant. The results are presented in Table 1.1. The effect of multiple Rutherford scattering on the observed thick-target energy coefficients is in the right direction but is not nearly large enough to account for the difference between curves 1 and 2 of Fig. 1.13. In any case, the attenuation coefficients for multiple scattering are significant and should be included in the analysis of thick-target angular distribution measurements. The data presented in Figs. 1.13 and 1.14 have not been corrected for multiple Rutherford scattering, because we have no satisfactory thin target a_ν from which we could evaluate these attenuation coefficients for a thick target. The fact that the points for heavy (or for medium-weight) nuclei fall on a smooth curve indicates that the parameter ξ correctly takes into account the excitation energy and the exciting proton energy. However, since two distinct curves are obtained, we conclude that the dependence on Z_2 is not correctly accounted for by the Alder-Winther theory.

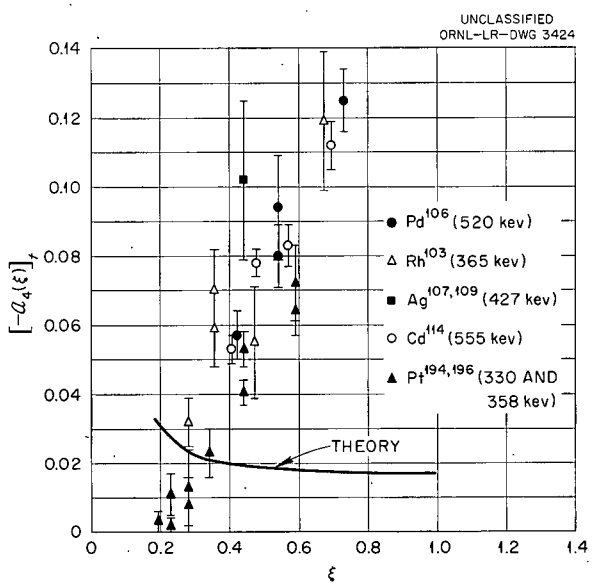

Fig. 1.14. Thick-Target Energy-dependent Coefficient $a_4(\xi)$ Deduced from Angular-Distribution Measurements Plotted at a Value of ξ Corresponding to the Incident-Proton Energy on the Thick Target. The solid curve labeled "theory" represents the thick-target energy-dependent coefficient $[a_4(\xi_i)]_t$.

1.7.2 Gamma-Ray Yields from Cadmium Nuclei

The yields of gamma rays resulting from coulomb excitation have been measured for the eight isotopes of cadmium. The rather complex spectrum of normal cadmium has been resolved into the contributions of the different isotopes by the use of isotopically enriched targets. Thick metallic targets were prepared by electrodeposition of the cadmium onto nickel. Approximately 50 mg of the enriched metal was required for each target.

The information obtained is given in Tables 1.2 and 1.3. In Table 1.2, the gamma rays given in the column headed E_γ are assigned to the nuclei listed in the first column. The observed yields of the gamma rays for different incident proton energies are given in the third and fourth columns. The transitions per microcoulomb are deduced by use of the isotopic enrichment (fifth column) and the total internal conversion coefficient, α_T (seventh column). From the number of transitions

TABLE 1.1. ATTENUATION COEFFICIENTS FOR MULTIPLE RUTHERFORD SCATTERING FOR PROTON-GAMMA DISTRIBUTIONS FROM THICK TARGETS FOR THE CASE WHEN $a_\nu(\xi)$ IS CONSTANT

Pt^{194}; ΔE = 330 kev			Rh^{103}; ΔE = 365 kev		
E_p (Mev)	$\bar{G}_2$	$\bar{G}_4$	E_p (Mev)	$\bar{G}_2$	$\bar{G}_4$
5.0	0.955	0.841	2.9	0.980	0.940
4.0	0.961	0.872	2.5	0.982	0.946
3.0	0.971	0.916	2.1	0.985	0.956
2.0	0.988	0.961	1.7	0.989	0.969

TABLE 1.2. SUMMARY OF GAMMA YIELDS AND INFORMATION NEEDED TO OBTAIN THE REDUCED $E2$ TRANSITION PROBABILITIES

Nucleus	E_γ (kev)	E_p (Mev)	$I\left(\frac{\lambda\text{'s}}{\text{Microcoulomb}}\right)$	Isotopic Abundance (%)	Classification	α_{total}	Transitions / Microcoulomb	$\int_0^E \frac{E f g_2(\xi)\, dE}{dE/d\rho x}$	$B(E2)_{ex} \times 10^{48}$
Cd^{116}	517	2.10	1.12×10^4	71.2	$E2$	0.0064	1.58×10^4	5.12×10^2	0.579
		2.40	3.94×10^4				5.57×10^4	1.89×10^3	0.554
		2.70	1.02×10^5				1.44×10^5	4.94×10^3	0.547
		3.00	2.11×10^5				2.98×10^5	1.03×10^4	0.545
		3.30	3.79×10^5				5.36×10^5	1.85×10^4	0.544
Cd^{114}	555	2.10	8.58×10^3	94.2	$E2$	0.0052	9.15×10^3	3.16×10^2	0.535
		2.40	3.56×10^4				3.80×10^4	1.33×10^3	0.527
		2.70	1.01×10^5				1.08×10^5	3.75×10^3	0.532
		3.00	2.17×10^5				2.32×10^5	8.24×10^3	0.520
		3.30	4.24×10^5				4.52×10^5	1.53×10^4	0.544
Cd^{112}	610	2.10	3.39×10^3	83.5	$E2$	0.0046	4.08×10^3	1.58×10^2	0.468
		2.40	1.76×10^4				2.12×10^4	7.86×10^2	0.489
		2.70	5.65×10^4				6.80×10^4	2.48×10^3	0.497
		3.00	1.27×10^5				1.53×10^5	5.90×10^3	0.470
		3.30	2.64×10^5				3.18×10^5	1.17×10^4	0.493
Cd^{110}	656	2.10	1.44×10^3	70.0	$E2$	0.0033	2.06×10^3	8.27×10^1	0.444
		2.40	9.07×10^3				1.30×10^4	4.88×10^2	0.474
		2.70	2.95×10^4				4.23×10^4	1.71×10^3	0.440
		3.00	7.49×10^4				1.07×10^5	4.37×10^3	0.436
		3.30	1.63×10^5				2.33×10^5	9.08×10^3	0.457
Cd^{108}	630	2.10						1.20×10^2	
		2.40	2.14×10^3	14.2	$E2$	0.0038	1.51×10^4	6.41×10^2	0.412
		2.70	6.02×10^3				4.25×10^4	2.01×10^3	0.370
		3.00	1.94×10^4				1.37×10^5	5.17×10^3	0.464
		3.30	5.35×10^4				3.78×10^5	1.04×10^4	0.636
Cd^{106}	630	2.10	6.16×10^2	32.9	$E2$	0.0038	1.87×10^3	1.20×10^2	0.267
		2.40	5.35×10^3				1.62×10^4	6.41×10^2	0.434
		2.70	1.47×10^4				4.45×10^4	2.01×10^3	0.380
		3.00	3.89×10^4				1.18×10^5	5.17×10^3	0.392
		3.30	8.83×10^4				2.67×10^5	1.04×10^4	0.441
Cd^{113}	582	2.10	1.63×10^3	54.1	$E2$?	0.0046	3.03×10^3	2.25×10^2	0.246
		2.40	8.99×10^3				1.67×10^4	1.03×10^3	0.296
		2.70	2.70×10^4				5.01×10^4	3.07×10^3	0.298
		3.00	5.74×10^4				1.07×10^5	6.99×10^3	0.280
		3.30	1.035×10^5				1.92×10^5	1.34×10^4	0.262
Cd^{113}	300	2.10	1.41×10^4	54.1	$M1$?	0.024	2.67×10^4	5.10×10^3	0.0957
		2.40	3.03×10^4				5.74×10^4	1.07×10^4	0.0980
		2.70	5.75×10^4				1.09×10^5	1.98×10^4	0.101
		3.00	9.50×10^4				1.80×10^5	3.16×10^4	0.104
		3.30	1.49×10^5				2.82×10^5	4.72×10^4	0.109
Cd^{111}	610	2.10	4.78×10^2	64.5	$E2$?	0.0040	7.44×10^2	1.58×10^2	0.0845
		2.40	2.77×10^3				4.31×10^3	7.86×10^2	0.0985
		2.70	7.67×10^3				1.19×10^4	2.48×10^3	0.0861
		3.00	2.43×10^4				3.78×10^4	5.90×10^3	0.115
		3.30	5.03×10^4				7.83×10^4	1.17×10^4	0.120
Cd^{111}	250	2.10	1.08×10^3	64.5	$E2$	0.061	1.78×10^3		
		2.40	2.74×10^3				4.50×10^3		
		2.70	5.05×10^3				8.31×10^3		
		3.00	9.25×10^3				1.52×10^4		
		3.30	1.43×10^4				2.35×10^4		
Cd^{111}	342	2.10	1.13×10^4	64.5	$M1$?	0.0176	1.78×10^4	3.40×10^3	0.104
		2.40	2.66×10^4				4.20×10^4	8.02×10^3	0.104
		2.70	5.25×10^4				8.27×10^4	1.54×10^4	0.106
		3.00	8.87×10^4				1.40×10^5	2.60×10^4	0.107
		3.30	1.43×10^5				2.26×10^5	4.00×10^4	0.112

TABLE 1.3. SUMMARY OF THE TRANSITION PROBABILITIES, HALF LIVES, AND QUADRUPOLE MOMENTS FOR THE EVEN ISOTOPES OF CADMIUM

Nucleus	E (kev)	I	$B(E2)_d \times 10^{48}$	$T_{1/2}$ (sec)	$(Q_0)_{ex} \times 10^{24}$	$(Q_0)_{B(E2)} \times 10^{24}$	$\frac{(Q_0)_{B(E2)}}{(Q_0)_{ex}}$	$\frac{B(E2)_d}{B(E2)_{sp}}$
Cd^{116}	517	2	0.110	1.39×10^{-11}	6.16	2.35	0.38	15.8
Cd^{114}	555	2	0.106	1.01×10^{-11}	5.94	2.31	0.39	15.7
Cd^{112}	610	2	0.0966	6.93×10^{-12}	5.70	2.20	0.39	14.6
Cd^{110}	656	2	0.0900	5.17×10^{-12}	5.51	2.13	0.39	14.0
Cd^{108}	630	2	0.0830	6.86×10^{-12}	5.65	2.17	0.36	13.2
Cd^{106}	630	2	0.0824	6.91×10^{-12}	5.66	1.96	0.36	13.4

per microcoulomb and the integral

$$\int_0^E \frac{E_f g_2(\xi)\, dE}{dE/d\rho x}$$

(given in the ninth column in units of kev × mg/cm^2), the reduced transition probability for $E2$ excitation, $B(E2)_{ex}$, is obtained. These values are given in the last column.

The half lives, the electric quadrupole moments derived from excitation energies $(Q_0)_{ex}$, the reduced transition probabilities $(Q_0)_{B(E2)}$, and the ratios $(Q_0)_{B(E2)}/(Q_0)_{ex}$ and $B(E2)_d/B(E2)_{sp}$ are given for the even isotopes in Table 1.3. The $B(E2)_d$ is the reduced transition probability for decay by an $E2$ transition. The $B(E2)_{sp}$ is the reduced transition probability for decay by an $E2$ transition between single-particle states.

1.8 YIELD OF THE REACTION $Si^{28}(p,p'\gamma)Si^{28}$

H. B. Willard
H. O. Cohn
J. K. Bair
J. D. Kington

A thin-target yield curve has been obtained for the gamma rays resulting from the excitation of the 1.78-Mev level in Si^{28} by the inelastic scattering of protons. Gamma rays were detected by a 3 × 3 in. NaI crystal. Incident protons of energies ranging from 2 to 5 Mev were obtained from the ORNL 5.5-Mv accelerator. Table 1.4 lists preliminary data on the levels observed below 5-Mev bombarding energy.

Table 1.4 lists in the first column the number of the resonance, in the second column the proton energy at which the level is observed, in the third column the observed width, and in the fourth column the energy of excitation in the P^{29} compound nucleus.

TABLE 1.4. ENERGY LEVELS IN Si^{28} EXCITED BY INELASTIC PROTON SCATTERING

Level No.	E_p (Mev)	Γ Observed (kev)	E_{ex} in P^{29} (Mev)
1	3.10	13	5.72
2	3.34	14	5.95
3	3.57	≈70	6.17
4	3.72	≈50	6.31
5	4.24	14	6.92
6	4.44	≈100	7.01
7	4.69	≲3.6	7.25
8	4.89	13	7.44

1.9 ACCELERATOR ENERGY CALIBRATION AND PROTON-NEUTRON THRESHOLD MEASUREMENTS

J. D. Kington
H. O. Cohn
J. K. Bair
H. B. Willard

A nuclear-resonance instrument has been installed on the beam-analyzing magnet of the 5.5-Mv Van de Graaff accelerator to permit direct determination of the magnetic field. The analyzed proton energy should be related to the resonant

frequency f by the expression

$$E\left(1+\frac{E}{2Mc^2}\right) = kf^2 ,$$

where Mc^2 is the proton rest energy and k is a constant. However, because the magnetic field may saturate later at the location of the nuclear-resonance probe rather than where the beam passes through the magnet, some variation of the constant is to be expected at high fields.

A calibration was obtained by detecting the known (p,n) thresholds of H^3, Li^7, and Be^9 by using the mass 1 and the mass 2 beam and of B^{11} and C^{13} by using the mass 1 beam. In addition, some of the previously used $F^{19}(p,\alpha\gamma)O^{16}$ resonances (masses 1, 2, and 3) and the $Al^{27}(p,\gamma)Si^{28}$ resonance at 993.3 kev (masses 1 and 2) were measured. Calculated values of k, obtained in these measurements, are plotted in Fig. 1.15 as a function of equivalent proton energy. All points except the $F^{19}(p,\alpha\gamma)O^{16}$ resonances at 1355 and 1381 kev were fitted by least squares to the parabola shown. All values except these fall on

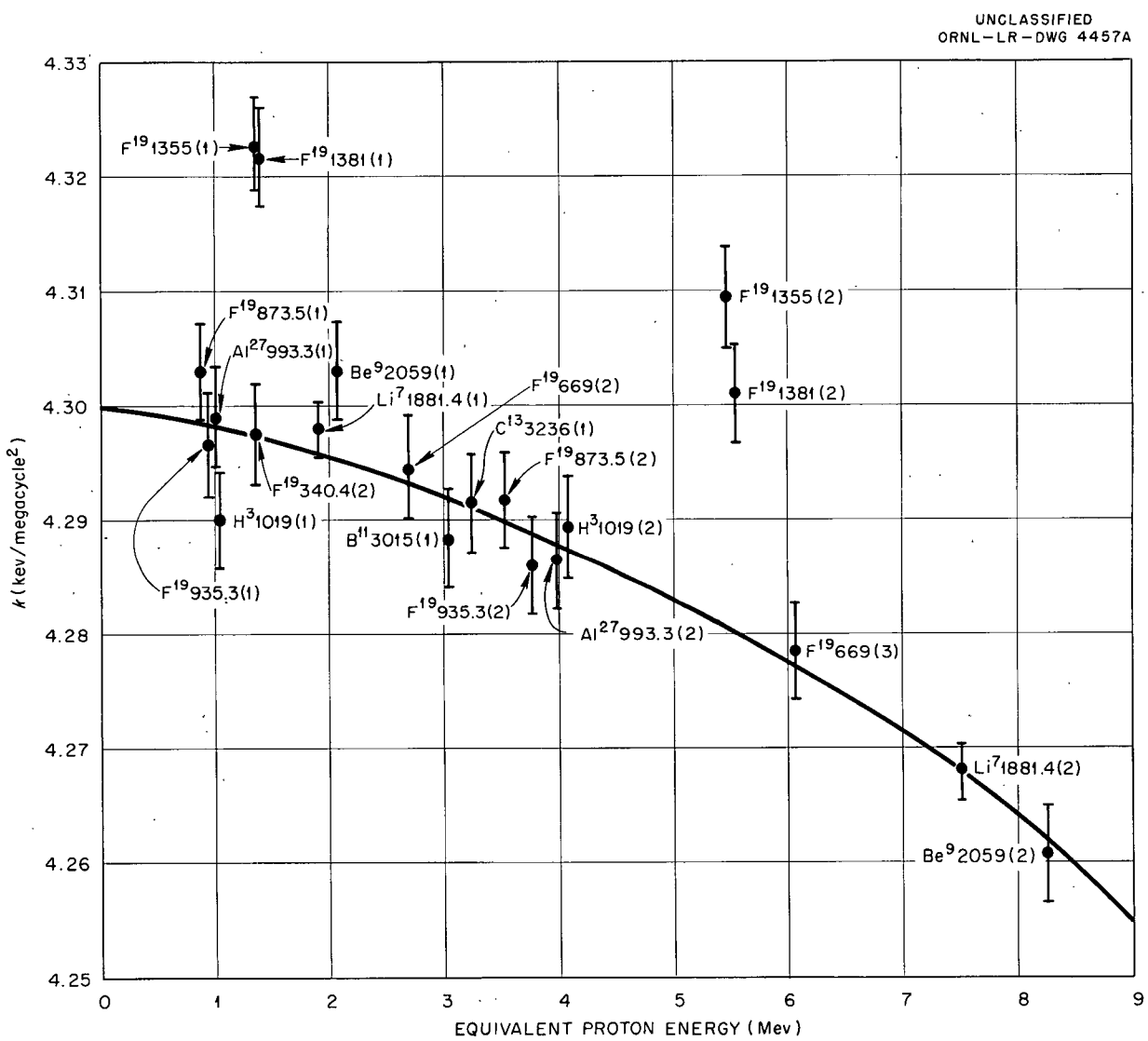

Fig. 1.15. Curve of Calibration Constant for the 5.5-Mv Van de Graaff vs Equivalent Proton Energy.

TABLE 1.5. REACTION THRESHOLDS

Reaction	New Threshold (kev)	Old Threshold (kev)	Old Threshold Corrected* (kev)
$F^{19}(p,n)Ne^{19}$	4240 ± 8	4253 ± 5	4243
$Na^{23}(p,n)Mg^{23}$	5053 ± 10	5090 ± 10	5061
$Al^{27}(p,n)Si^{27}$	5792 ± 10	5819 ± 10	5789

*Corrected to the new values of the $F^{19}(p,\alpha\gamma)O^{16}$ resonances.

the curve within the limits of error. It is concluded that the energies of these resonances should be 1347 ± 2 and 1374 ± 2 kev. Recent measurements at the California Institute of Technology are in good agreement with these new values.[17]

Since several previous threshold measurements by this group were based in part on the incorrect values of 1355 and 1381 kev for these $F^{19}(p,\alpha\gamma)O^{16}$ resonances, new data were obtained for $F^{19}(p,n)Ne^{19}$, $Na^{23}(p,n)Mg^{23}$, and $Al^{27}(p,n)Si^{27}$. In addition, the thresholds for the $N^{15}(p,n)O^{15}$, $Mg^{25}(p,n)Al^{25}$, $Mg^{26}(p,n)Al^{26*}$, $Cu^{63}(p,n)Zn^{63}$, and $Cu^{65}(p,n)Zn^{65}$ reactions were obtained. Table 1.5 compares the new values of the F^{19}, Na^{23}, and Al^{27} neutron thresholds with the earlier data and presents the earlier data corrected for the new values of 1347 and 1374 kev for the $F^{19}(p,\alpha\gamma)O^{16}$ resonances. Table 1.6 gives the thresholds for the reactions studied and the reaction Q values. The values given for Mg^{26} are for neutron emission to the first excited state in Al^{26}, based on the recent data[18] showing an isomeric state in Al^{26} at 219 ± 13 kev, together with the high spin value (J = 5) of the ground state of Al^{26}.

[17] C. A. Barnes, private communication.

[18] R. W. Kavanagh, W. R. Mills, and R. Sherr, *Phys. Rev.* 97, 248 (1955).

TABLE 1.6. REACTION THRESHOLDS AND Q VALUES

Reaction	Threshold (kev)	$-Q$ (kev)
$N^{15}(p,n)O^{15}$	3776 ± 8	3540
$F^{19}(p,n)Ne^{19}$	4240 ± 8	4028
$Na^{23}(p,n)Mg^{23}$	5053 ± 10	4842
$Mg^{25}(p,n)Al^{25}$	5289 ± 25	5085
$Mg^{26}(p,n)Al^{26}$	5200 ± 10	5007
$Al^{27}(p,n)Si^{27}$	5792 ± 10	5585
$Cu^{63}(p,n)Zn^{63}$	4213 ± 8	4147
$Cu^{65}(p,n)Zn^{65}$	2170 ± 5	2137

The values in Table 1.6 should supersede those given in the last semiannual progress report,[19] wherein the thresholds were computed by using a constant value of k; further, the value for sodium was erroneously attributed to Mg^{26} because of a target impurity.

[19] J. D. Kington, J. K. Bair, and H. B. Willard, *Phys. Semiann. Prog. Rep. Sept. 10, 1954*, ORNL-1798, p 8.

2. RADIOACTIVITY AND NUCLEAR ISOMERISM

2.1 INNER BREMSSTRAHLUNG–GAMMA-RAY CORRELATIONS

E. D. Klema

An intensive series of experiments has been carried out in an attempt to measure inner bremsstrahlung–gamma-ray directional angular correlations. Three electron-capturing isotopes, Be^7, Cr^{51}, and Mn^{54}, were studied. These are all cases in which the electron capture takes place part of the time to an excited state of the product nucleus, which then decays by the emission of a single gamma ray to the ground state.

In each case the window of one differential analyzer was set to accept pulses corresponding to photon energies between 26 and 39 kev, and the window of the other analyzer was set on the full-energy peak of the gamma ray in question. Under these conditions gamma-ray scattering from one detector to the other could not contribute to the observed coincidence counting rate. In each of the above cases a coincidence rate of the order of 2×10^{-2} counts/sec was found. It was established that this effect was due to the fact that iodine K x rays escaping from the NaI crystal detecting the gamma rays were being detected in the window of the other analyzer. The effect was eliminated by surrounding the crystal used for gamma-ray detection with a graded shield made of 5 mils of cadmium and 5 mils of copper. When this was done, the coincidence rates observed with the Be^7 and the Mn^{54} sources were the random rates to be expected from the "singles" counting rates.

In the case of Cr^{51}, a net coincidence rate of the order of 4×10^{-4} counts/sec was observed, and three points were obtained of the bremsstrahlung spectrum in coincidence with the gamma ray. These were obtained with the lower window set from 26 to 39 kev, from 39 to 52 kev, and from 52 to 65 kev. At this time it was discovered by Brysk and Rose[1] that the expected bremsstrahlung–gamma-ray angular correlations are isotropic for nearly all cases, and the work was discontinued.

In the course of the above experiments, since the coincidence counting rates were extremely low, it was necessary to determine how large the apparent coincidence rate was for the apparatus with no source in place. It was found that, with the source removed, two coincidence counts were recorded in a 24-hr period; with the source removed and the lead from the pulse-height selector of one of the amplifiers disconnected, no coincidences were observed in a 24-hr period.

2.1.1 Tantalum-181

The directional angular correlation of the main 132–480-kev gamma-gamma cascade in Ta^{181} has been measured in a series of five experiments with a total of 1.2×10^6 coincidence counts obtained at 19 angular positions. The form of the Hf^{181} source was HfF_4 in 27 N HF. The correlation was measured in order to check previous data taken at five angles with nonautomatic equipment. The time-integral correlation function obtained, after correcting for the finite angular resolution of the detectors, is

$$W(\theta) = 1 - (0.286 \pm 0.0018)P_2(\cos\theta) - (0.067 \pm 0.0025)P_4(\cos\theta) .$$

The coefficients of the function obtained in the present experiment are in good agreement with those found previously.

2.1.2 Hafnium-177

The angular correlation of the 206–112-kev gamma-gamma cascade in Hf^{177} has been measured at 19 angular positions; again, the measurements served as a check on previous measurements made with equipment which has since been improved. These data have not yet been analyzed.

2.2 DECAY AND GAMMA SPECTRUM OF 0.8-sec Zr^{90m}

E. C. Campbell F. C. Maienschein
R. W. Peelle

When natural zirconium of high purity was irradiated with neutrons inside the ORNL Graphite Reactor, it was found to exhibit an activity which decays with a half life of 0.83 ± 0.03 sec. Irradiation and ejection of the sample were accomplished with the aid of a fast pneumatic device consisting principally of a rectangular aluminum tube through which the zirconium sample, held in a plastic sample carrier, is blown into and out of the reactor with compressed gas. Upon ejection from the

[1] H. Brysk and M. E. Rose, *Angular Correlation in Orbital Capture*, ORNL-1862 (March 23, 1955).

reactor, the sample travels directly into a shielded region, where it is brought to rest pneumatically and where the radiations emitted by the sample are detected by a scintillation counter or spectrometer. The transit time from reactor to detector is of the order of 0.1 sec.

In Fig. 2.1 is shown the decay curve. Data were taken with a standard $1 \times 1\frac{1}{2}$ in. NaI scintillation counter with a single-channel analyzer set to accept pulses corresponding to gamma-ray energies above 1.1 Mev. A moving-pen galvanometer writing on paper moving at 12.5 cm/sec recorded pips from a scale of 800. From these data the decay curve was computed. From analysis of several such records taken under slightly different conditions, we determined the half life to be 0.83 ± 0.03 sec.

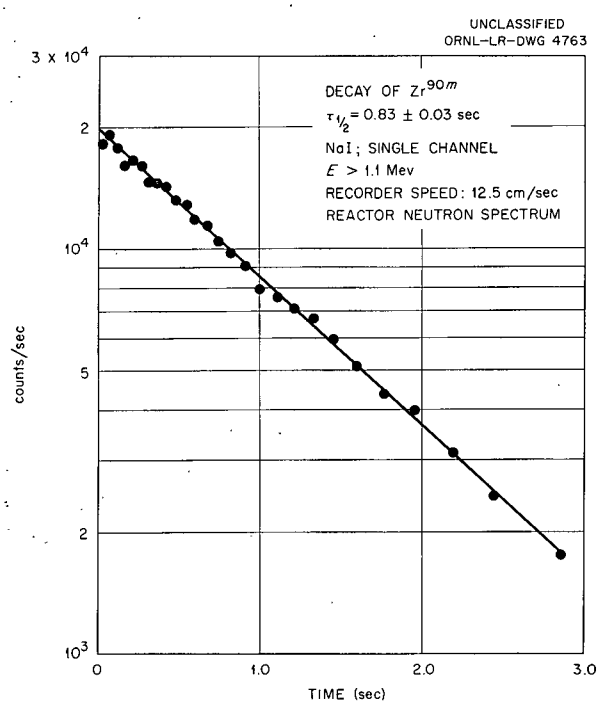

Fig. 2.1. Decay of Zr^{90m}.

In order to determine the energy of the gamma rays associated with the 0.8-sec activity, the pulse-height distribution of pulses from the NaI detector was obtained with the help of a 40-channel analyzer designed by P. R. Bell and G. G. Kelley at this Laboratory. The results are shown in Fig. 2.2. Calibration points are indicated by arrows for the full-energy peaks of Zn^{65}, F^{20}, and ThC″. The curve is interpreted as being due to a single gamma ray of energy 2.30 ± 0.02 Mev. The low-

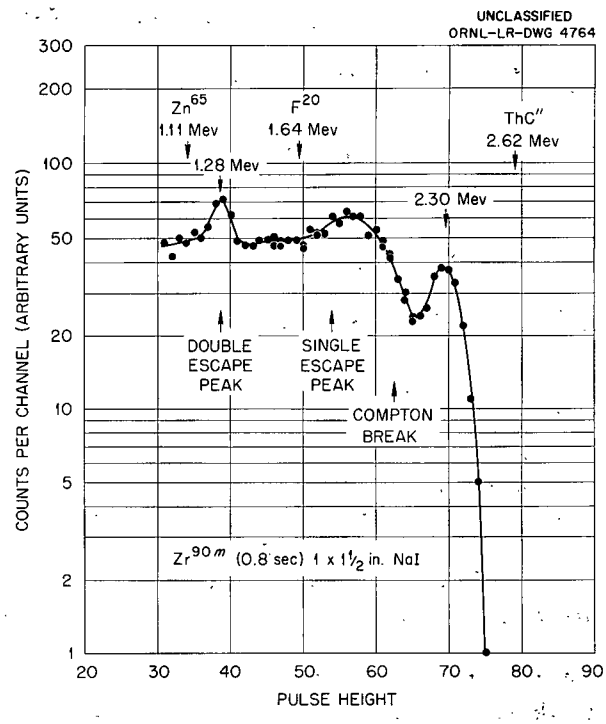

Fig. 2.2. Pulse-Height Spectrum of 2.3-Mev Gamma Ray in Zr^{90m} (0.83 sec).

energy region (not shown) was also investigated, but this region, except for two peaks ascribed to a 19-sec Hf^{179m} contamination, showed only the normal low-energy continuation of the Compton distribution.

By irradiating the separated isotopes of zirconium, we established that the activity was definitely associated with Zr^{90} as a target nucleus. In order to determine whether the nuclear reaction was produced by thermal neutrons, we irradiated a sample of zirconium which was completely covered by cadmium. We observed that the activity was not sensitive to the presence of cadmium and concluded that the activity was therefore not produced by thermal neutrons in the reactor.

In Sec. 1.6, data on the fast-neutron excitation cross section is presented. These data are taken as evidence that the nuclear reaction responsible is $Zr^{90}(n,n')Zr^{90m}$.

2.3 HALF-LIFE MEASUREMENT BY SQUARE-WAVE ACTIVATION

E. C. Campbell

A method is proposed for measuring half lives of nuclear isomers by means of a pulse-activation technique. Assume that the isomer is produced by

an inelastic scattering of fast neutrons from a (p,n) reaction; the neutron flux at the position of the sample to be studied is square-wave-modulated by turning the proton beam on and off the target at a frequency $f = 1/T$ with an electrostatic deflector. Delayed gammas from the sample are detected by a scintillation counter only during the interval when the beam is off. For simplicity, assume that each "beam-on" interval of length $T/2$ is followed by a counting interval of equal length. Let A_0 be the counting rate of the sample at the beginning of each counting interval after equilibrium has been reached. The average counting rate R is then given by

$$R = \frac{A_0}{T}\int_0^{T/2} e^{-\lambda t}\,dt = \frac{A_0}{\lambda T}\left(1 - e^{-\lambda T/2}\right) ,$$

where λ is the decay constant of the isomeric transition. Let A_s be the saturation counting rate of the sample. Then at equilibrium the buildup of activity during each interval T is equal to the decay. This condition relates A_0 to A_s by the following equation:

$$A_0 e^{-\lambda T} + A_s\left(1 - e^{-\lambda T/2}\right) = A_0 ,$$

or

$$A_0 = \frac{A_s}{1 + e^{-\lambda T/2}} .$$

The expression for R then becomes

$$R = \frac{A_s}{\lambda T}\,\frac{1 - e^{-\lambda T/2}}{1 + e^{-\lambda T/2}} = \frac{A_s}{\lambda T}\tanh\left(\frac{\lambda T}{4}\right) .$$

In terms of the frequencies $f = 1/T$ and

$$f_0 = \frac{\lambda}{4} = \frac{0.173}{\tau_{1/2}} ,$$

where $\tau_{1/2}$ is the half life, the previous equation can be written

$$R = \frac{A_s}{4}\,\frac{f}{f_0}\tanh\left(\frac{f_0}{f}\right) . \qquad (1)$$

The limiting forms of this expression are easily shown to be:

$$R = \frac{A_s}{4}\,\frac{f}{f_0} , \quad f \ll f_0 ;$$

$$R = \frac{A_s}{4} , \quad f \gg f_0 .$$

The method consists in measuring the average counting rate R as a function of the modulating frequency f. The value of f_0 and the half life $\tau_{1/2} = 0.173/f_0$ may be obtained either by fitting the data to Eq. 1 or by observing that the extrapolation of the linear portion of the curve intersects the constant high-frequency value $A_s/4$ at $f = f_0$, as shown in Fig. 2.3.

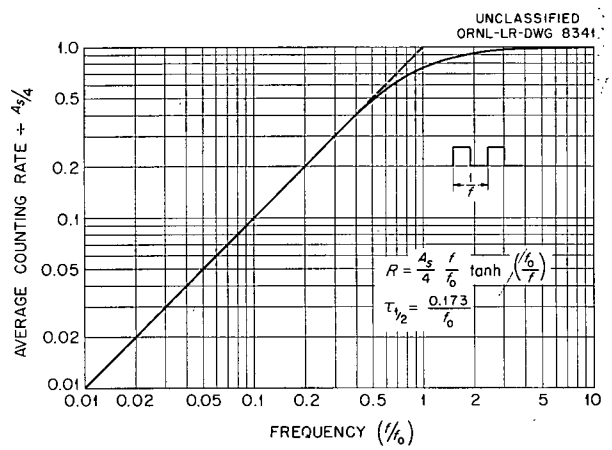

Fig. 2.3. Half-Life Measurement by Square-Wave Activation.

It should be noted that the problem is mathematically equivalent to that involved in obtaining the square-wave response of an electrical circuit consisting of a resistance and capacitance in series.

It is proposed to test this method when suitable timing circuits, presently under construction, are completed.

2.4 PROMPT FISSION GAMMA RAYS

J. E. Francis R. L. Gamble[2]

A previously described[3] investigation of U^{235} prompt fission gamma rays has been completed. A single $1\frac{1}{2} \times 1$ in. cylindrical NaI(Tl) crystal was used to detect gamma rays from a parallel-plate fission chamber. The gamma rays in coincidence with fission fragments were counted with a ten-

[2]ORINS fellow, University of Texas.

[3]R. L. Gamble, *Phys. Semiann. Prog. Rep. Sept. 10, 1953*, ORNL-1620, p 15.

channel pulse-height analyzer. The resolution of the coincidence circuit was 0.4 μsec.

The coincidence pulse-height spectra, after subtraction of the accidental coincidences, are shown in Figs. 2.4, 2.5, and 2.6. Their shapes indicate a continuous prompt fission gamma-ray spectrum. The analysis of the coincidence pulse-height spectrum to obtain the gamma-ray spectrum consisted of peeling monoenergetic gamma-ray pulse-height spectra of successively lower energies from it.[4] The analyzed pulse-height spectrum, after smoothing, is shown in Fig. 2.7. The prompt gamma-ray spectrum was obtained from Fig. 2.7 by dividing its ordinates by the detection efficiency of the crystal at the energies in question. The prompt gamma-ray spectrum so obtained is shown in Fig. 2.8, according to which there are 7.51 prompt gamma rays per fission, with a total energy of 7.46 Mev. The monoenergetic gamma-ray pulse-height spectra used in the analysis were from Cr^{51}, Sr^{85}, Cs^{137}, Cb^{95}, Zn^{65}, Y^{88}, Na^{24}, $Be^{9}(\alpha,n\gamma)C^{12}$, and $F^{19}(p,\alpha\gamma)O^{16}$.

The efficiency of the crystal for point sources of gamma rays was calculated by a graphical-numerical integration. The probability that a gamma ray will produce a scintillation in a thickness x cm of NaI is $1 - e^{-\tau x}$, where τ is the noncoherent gamma-ray absorption coefficient of NaI in cm^{-1} at the gamma ray in question. The efficiency of the crystal is the average value of $1 - e^{-\tau x}$ over all directions from the point source of gamma rays. The method employed a scale-of-six model of the crystal for measuring the distances x. To get the efficiency of the crystal for gamma rays from the fission chamber, the above point-source efficiencies were weighted with the measured spatial

[4] R. Stephenson and P. R. Bell, *Phys. Semiann. Prog. Rep. Sept. 10, 1953*, ORNL-1620, p 16.

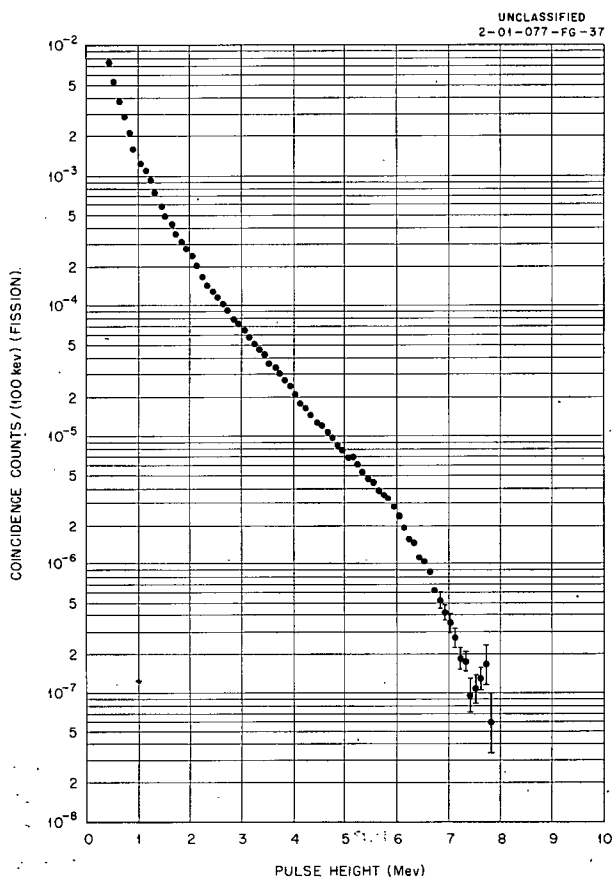

Fig. 2.4. Fission Gamma Coincidence Pulse-Height Spectrum at Gain 8.

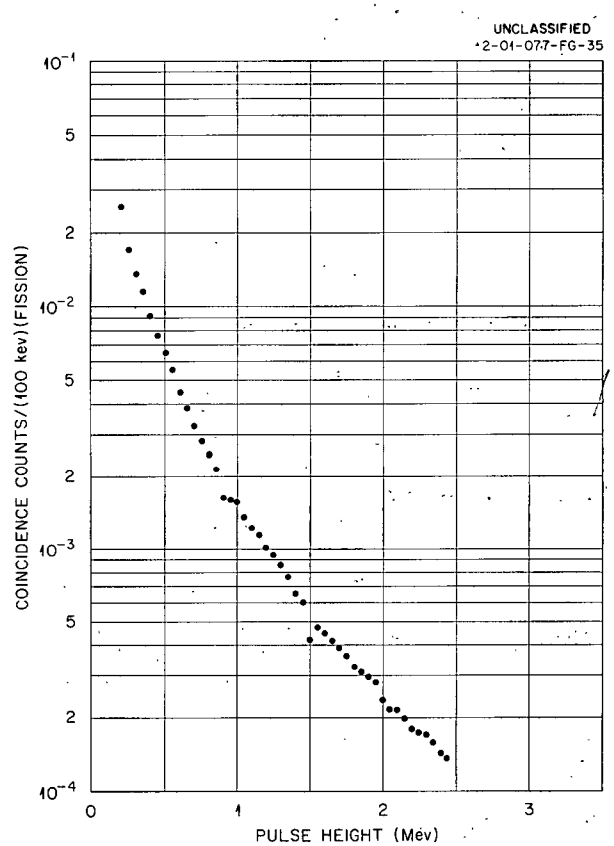

Fig. 2.5. Fission Gamma Coincidence Pulse-Height Spectrum at Gain 16.

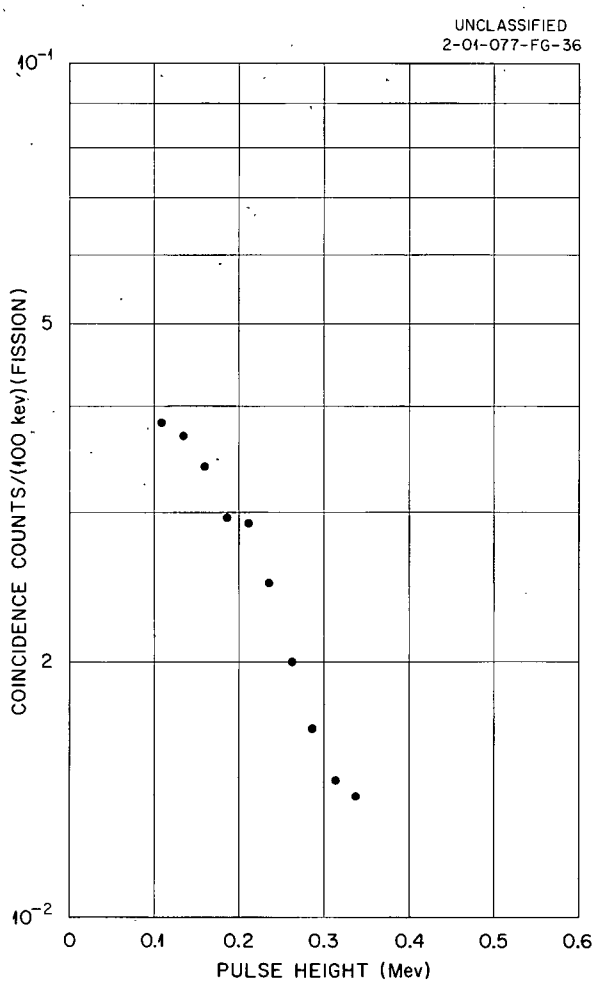

Fig. 2.6. Fission Gamma Coincidence Pulse-Height Spectrum at Gain 32.

fission distribution over the fission chamber. This average calculated efficiency with respect to the fission chamber had to be corrected for the effects of scattering and absorption of the gamma rays by shielding and moderating material near the fission chamber and crystal. The efficiency correction factor was determined by obtaining pulse-height spectra of the above monoenergetic gamma rays with and without the scattering and absorbing

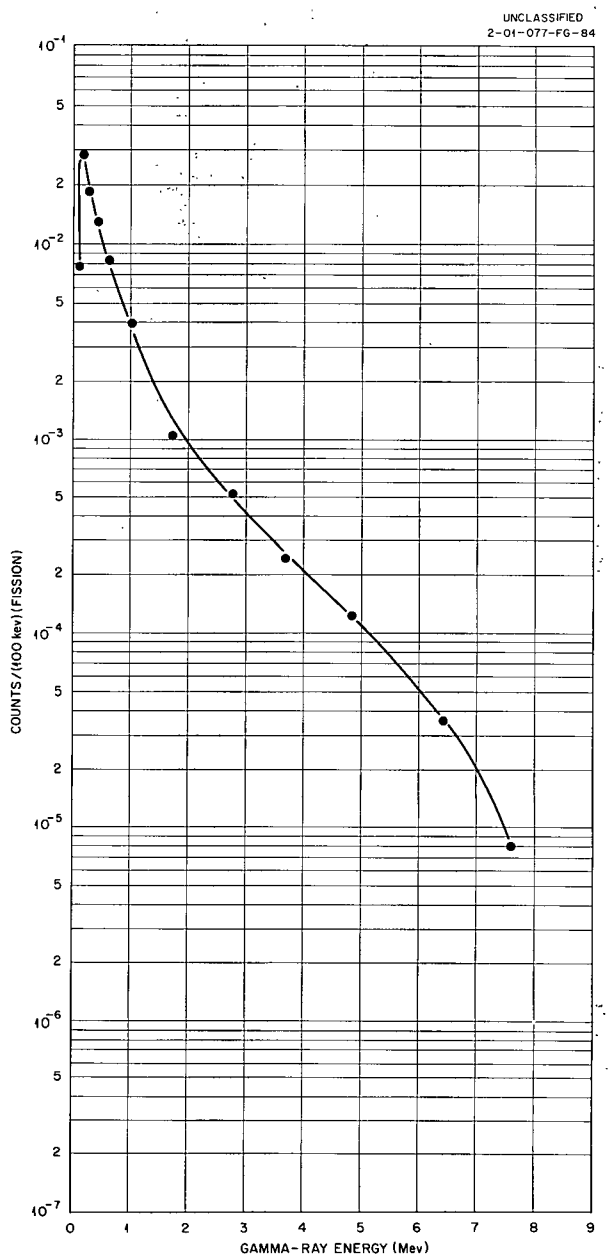

Fig. 2.7. Analyzed Fission Gamma Coincidence Pulse-Height Spectrum After Smoothing and Correction for Nonlinearity of Spectrum.

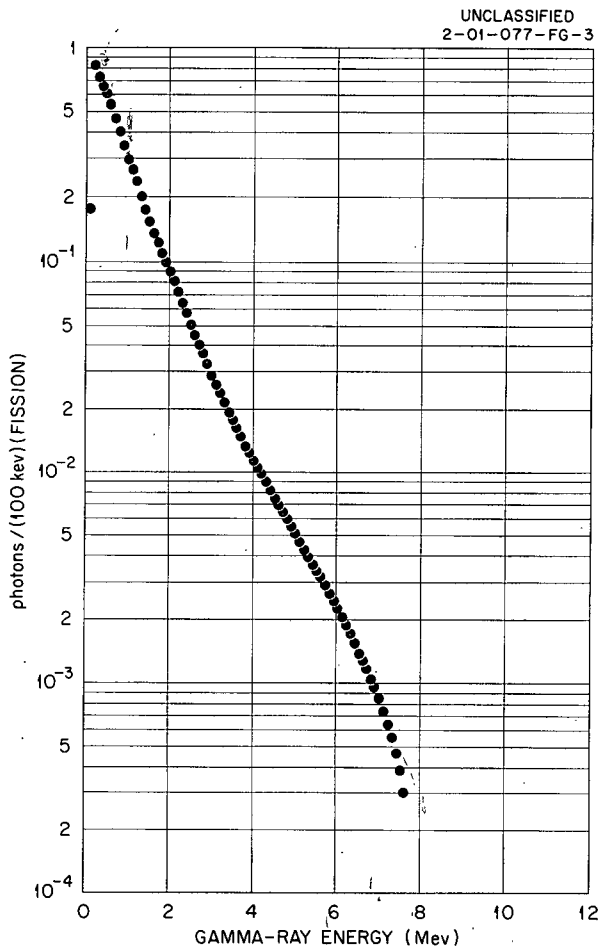

Fig. 2.8. Energy Spectrum of Prompt Fission Gamma Rays from U^{235}.

materials which were necessary for coincidence counting. The efficiency correction factor at the energy in question was the ratio of the counts per second in the former spectrum to the counts per second in the latter spectrum. The true efficiency, by which the ordinates of Fig. 2.7 were divided to obtain those of Fig. 2.8, was the calculated efficiency multiplied by the above efficiency correction factor.

A search was made for delayed fission gamma rays by inserting delay cables in both the fission and gamma branches of the coincidence circuit. Delays greater than 0.4 μsec in either branch reduced the coincidence counting rate to the calculated accidental coincidence counting rate. This was evidence that there were no delayed fission gamma rays.

3. NEUTRON DIFFRACTION

3.1 MAGNETIC STRUCTURE OF URANIUM HYDRIDE

C. G. Shull M. K. Wilkinson

It has been reported in the literature[1] that UH_3 exhibits a Curie point behavior at low temperatures and becomes ferromagnetic below 175°K. This behavior is very unexpected and represents the first case of ferromagnetism or antiferromagnetism in elements or compounds from this section of the periodic table. Recent studies at Ames and at Argonne have substantiated and extended the original Polish magnetic work, and it was decided to see whether neutron-diffraction patterns would exhibit details of either the ferromagnetic or the paramagnetic structure.

Polycrystalline samples of both UD_3 and UH_3 were prepared at the Ames Laboratory,[2] and neutron-diffraction patterns were obtained with sample temperatures ranging from 20°K to as high as 200°C. Both samples were of the beta-UH_3 form, with no evidence in the patterns of the alpha or low-temperature phase. Typical of the patterns are those for UD_3 shown in Fig. 3.1, which were obtained at 46°K and at room temperature. The low-temperature pattern shows additional scattering, principally in the (210) and (211) reflections, and these intensity changes represent the additional ferromagnetic scattering which develops at low temperature. A detailed study of the temperature dependence of the intensity for these two reflections has been made, and it is summarized in Fig. 3.2. Within the significance of the intensity measurements, the magnetic intensity exhibits a characteristic Brillouin temperature dependence and disappears at a temperature in the vicinity of the reported Curie temperature of 175°K. A further direct indication that the intensity changes are really of ferromagnetic origin comes in the analysis of the UH_3 patterns. The nuclear scattering in the hydride pattern differs completely from that in the deuteride pattern, and yet the intensity changes upon cooling are the same for the two materials. Thus the observed effects cannot be accounted for by crystallographic modifications such as sometimes occur at Curie temperatures.

Also to be noticed in Fig. 3.1 is the small but definite change in the diffuse-scattering level, and this is ascribed to the buildup of paramagnetic scattering at the higher temperatures. This diffuse scattering has been studied at temperatures up to about 200°C, that is, at temperatures up to 2.7 times the Curie temperature, so as to remove as much as possible any contributions caused by short-range magnetic order. In comparing the high-temperature diffuse-scattering level with the low-temperature observations, a correction for the normal lattice diffuse-scattering effects must be included. This correction is absent in the forward direction (small scattering angles) and gets larger as the scattering angle increases. After applying this correction to the diffuse-scattering intensity, the magnetic-disorder scattering was obtained in absolute units of differential scattering cross section, and this is shown in Fig. 3.3. This cross-section curve as a function of the scattering-angle variable $(\sin\theta)/\lambda$ exhibits the magnetic-form factor which characterizes the magnetic uranium atoms in the lattice.

Various magnetic lattice models have been studied in an attempt to account for the presence or absence of coherent magnetic intensity in the low-temperature patterns. These have included a number of possible ferrimagnetic models, as well as a simple ferromagnetic structure. The only model which has given satisfactory agreement with the observations is the simple ferromagnetic one in which all eight uranium atoms in the unit cell possess the same magnetic-scattering amplitude, and hence the same magnetic moment, with common orientation below the Curie point. Using the magnetic-structure factors characteristic of this model, the observed magnetic intensity can be used to calculate the magnetic-scattering cross section, and these evaluations are shown in Fig. 3.3 superimposed on the cross-section curve obtained from the diffuse scattering. The general agreement between the results obtained from coherent scattering in both UD_3 and UH_3 and the results obtained from the incoherent scattering in UD_3 appears to be quite satisfactory, considering the weakness of the observed effects.

[1] W. Trzebiatowski, A. Śliwa, and B. Stalinski, *Roczniki Chem.* 26, 110 (1952).

[2] We are indebted to R. E. Rundle for preparing these samples. He had furnished us with earlier samples of this material, and the diffraction patterns for these had enabled him to establish the crystallographic structure of the hydride; *see* R. E. Rundle, *J. Am. Chem. Soc.* 73, 4172 (1951).

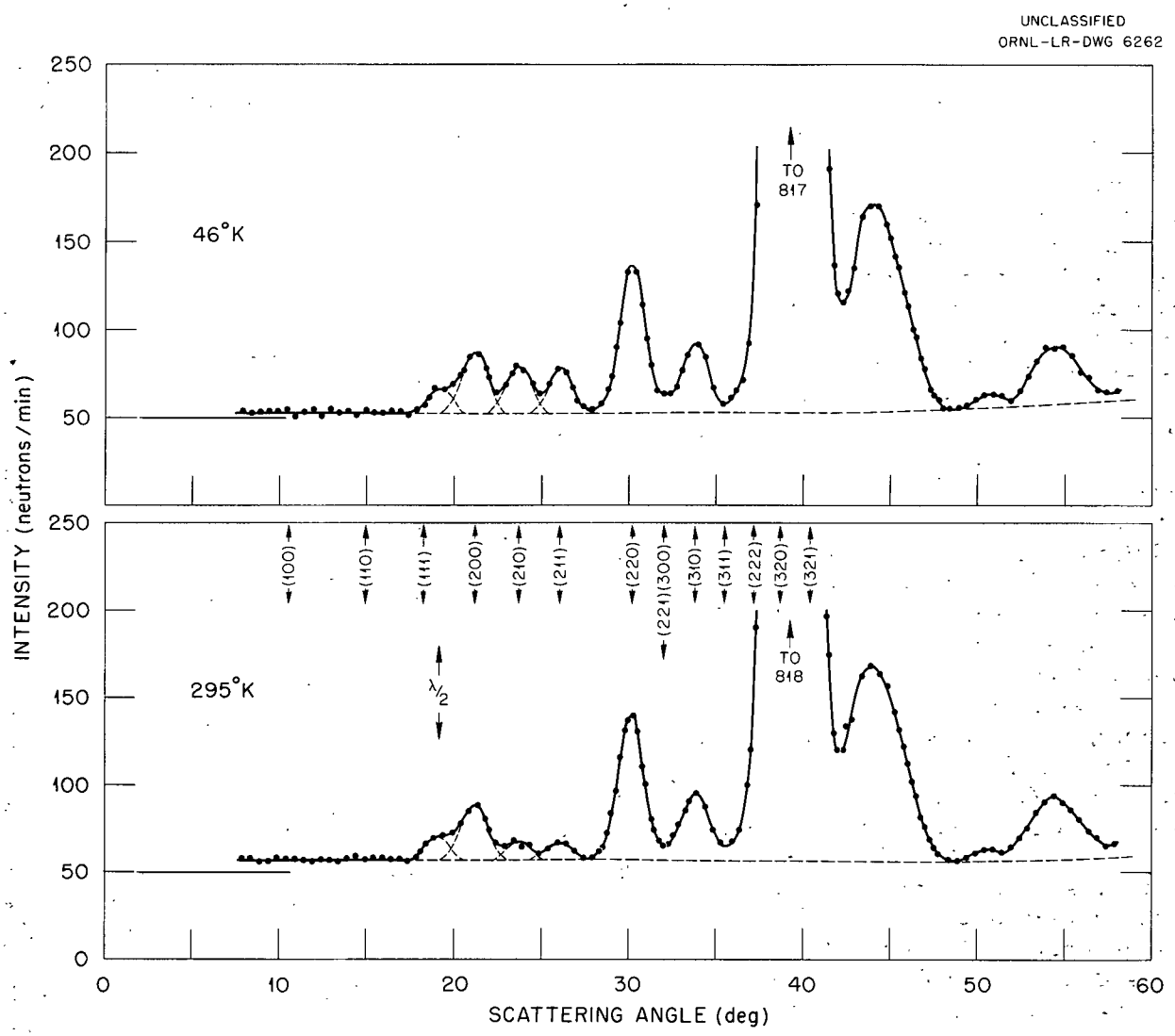

Fig. 3.1. Neutron-Diffraction Patterns for UD_3 at 46°K and at Room Temperature.

The intercept value of the magnetic-scattering cross section at zero scattering angle can be used to evaluate the effective ferromagnetic moment. According to magnetic-scattering theory, this intercept value is given as

$$P^2 = \frac{2}{3}\left(\frac{e^2\gamma}{mc^2}\right)^2 \frac{1}{4} g^2 J^2$$

$$= \frac{2}{3}(0.539 \times 10^{-12})^2 \frac{1}{4} g^2 J^2 ,$$

where g is the gyromagnetic ratio and J is the total quantum number of the magnetic ion. The ferromagnetic moment is given by the quantity (gJ), and upon insertion of the experimental value for P^2 this moment may be evaluated as 1.39 Bohr magnetons per uranium atom. This value is in the region of the measured value[3] for the ferromagnetic moment as determined from the magnetization at low temperature in a high magnetic field. On the other hand, it is somewhat lower than the value of

[3] W. E. Henry of the Naval Research Laboratory has kindly furnished us preliminary results on the ferromagnetic moment, for which he obtains a value of 1.0 ± 0.2 Bohr magnetons. He suspects that this value may be somewhat too low because of possible nonferromagnetic impurities in his sample.

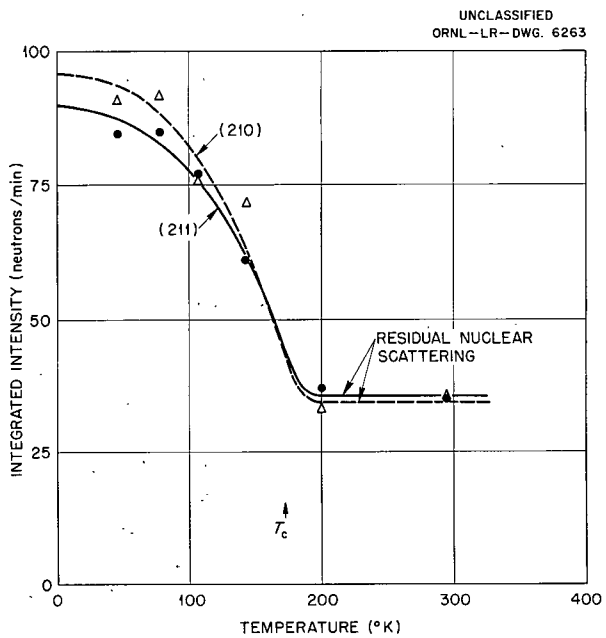

Fig. 3.2. Temperature Dependence of the (210) and (211) Ferromagnetic Reflections in UD_3.

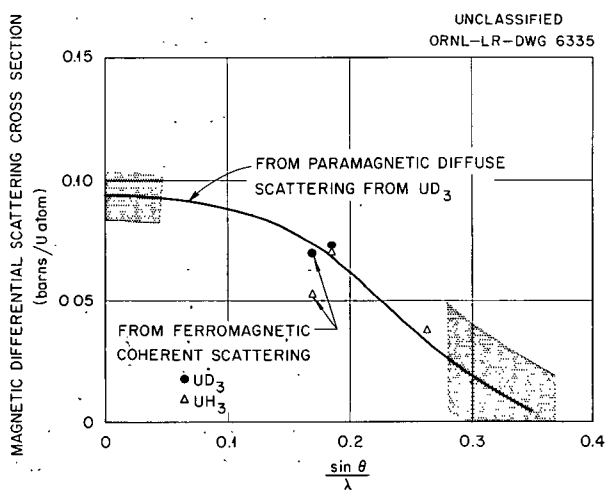

Fig. 3.3. Magnetic Scattering Cross Sections in Uranium Hydride as Obtained from Both Ferromagnetic and Paramagnetic Scattering.

about 2 Bohr magnetons suggested from the high-temperature paramagnetic susceptibility.

In addition to the magnetic-moment implications of the cross-section curve in Fig. 3.3, the magnetic-form factor suggested by this curve is of interest because it is to be associated with the electronic configuration in the uranium ion which manufactures the ionic magnetic moment. There exists considerable evidence that the outer electrons in uranium ions reside in the $5f$ shell, although, at the same time, it is recognized from energy considerations that a $6d$ configuration, or possibly a mixture of the two states, may sometimes be encountered. Since these two configurations differ considerably in their spatial distributions (average radius, width, etc.) within the atom, the magnetic-scattering form factor can be of some use in establishing the true configuration. Calculations have been made of the form factors to be expected for a variety of $6d$ and $5f$ configurations, and these are shown in Figs. 3.4 and 3.5 for comparison with the experimental results. In these calculations,

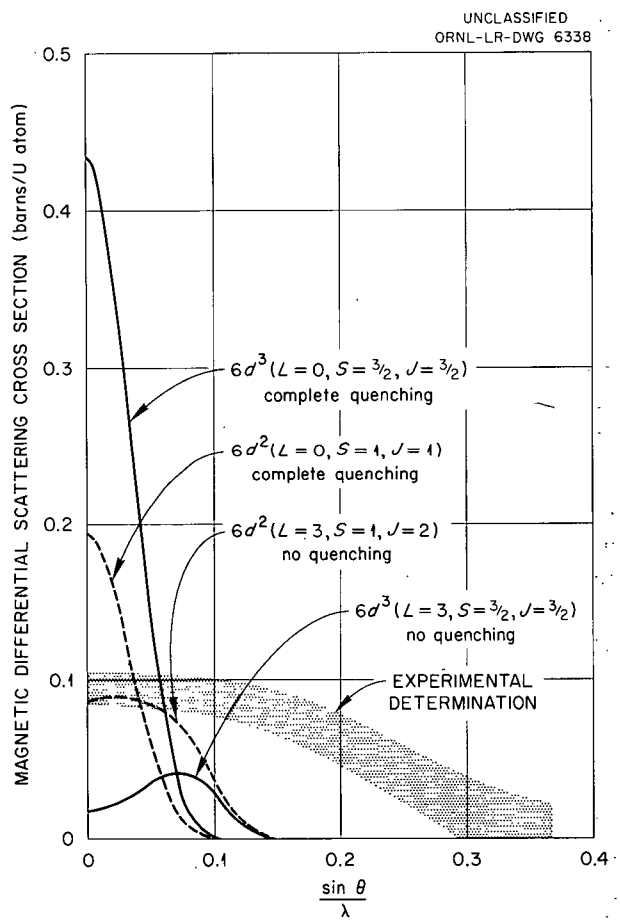

Fig. 3.4. Comparison Between Observed Magnetic Scattering in Uranium Hydride and That Calculated for Several $6d$-Shell Ionic Configurations.

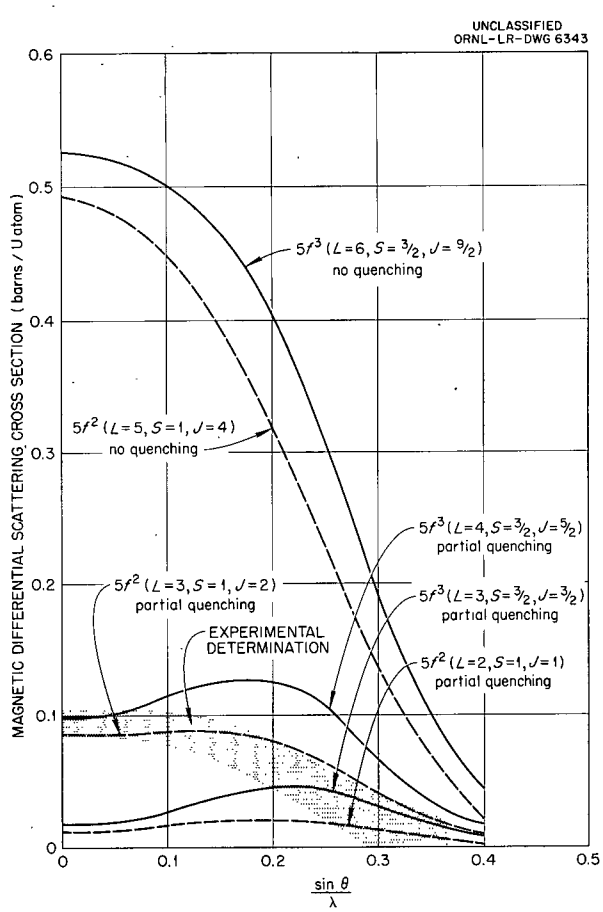

Fig. 3.5. Comparison Between Observed Magnetic Scattering in Uranium Hydride and That Calculated for Several 5*f*-Shell Ionic Configurations.

the general expression developed by Trammell[4] for the scattering by an ion possessing both orbital- and spin-moment values has been used, namely,

$$P^2 = \frac{2}{3}\left(\frac{e^2\gamma}{2mc^2}\right)^2 \frac{J}{J+1}\left(\frac{\overline{L}\cdot\overline{J}}{|J|} f_L + 2\,\frac{\overline{S}\cdot\overline{J}}{|J|} f_S\right)^2 ,$$

where L, S, and J are the orbital, spin, and total quantum numbers of the scattering ion, and f_L and f_S are the amplitude form factors associated with the orbital and spin moments, respectively. The spin form factor f_S has been calculated directly from the Pauling-Sherman hydrogenic wave functions, and the orbital form factor f_L was obtained from f_S by use of a suitable scale factor.

Figure 3.4 shows typical form factors calculated for both quenched and nonquenched $6d^2$ and $6d^3$ configurations and, for comparison, the experimental form factor obtained in uranium hydride. It is to be emphasized that all these results are on an absolute scale, and hence comparisons should be made with respect to the level of scattering, as well as the angular distribution. All the $6d$ calculated curves are concentrated much inside the angular region favored by experiment and hence do not appear to be suitable. On the other hand, a reasonably close matching can be accomplished with some of the $5f$ configuration shown in Fig. 3.5. The most favored configuration which has been calculated corresponds to a $5f^2 7S$ distribution, with partial quenching of the orbital moment. In addition to the form factors calculated for pure $6d$ or $5f$ configurations, some mixed-state configurations have been investigated, but these have not appeared to be so successful as those shown for the $5f$ case. Thus these observations can be considered as evidence that the outer electrons of the uranium ions in uranium hydride are present in the $5f$ shell.

3.2 MAGNETIC STRUCTURE OF $MnCl_2$

M. K. Wilkinson R. B. Murray
C. G. Shull

Previous experimental investigations at this Laboratory[5] have indicated that both the specific heat and magnetic susceptibility of $MnCl_2$ have unusual behavior at low temperatures. The specific-heat data showed two sharp lambda-type anomalies, located at 1.81 and 1.96°K, while the polycrystalline magnetic susceptibility passed through a plateau between 2 and 1.5°K and was rising again at 1.1°K, which was the lowest temperature obtained during the measurements. These data suggest that there is a double transition in the electron-spin system of the divalent manganese ions and that both transitions involve antiferromagnetic ordering. The specific-heat maximum at 1.96°K presumably represents a transition from the paramagnetic state to a first type of antiferromagnetic

[4] G. T. Trammell, *Phys. Rev.* 92, 1387 (1953); see particularly Eq. 38 modified to the conditions of the present experiment.

[5] R. B. Murray, L. D. Roberts, and R. A. Erickson, *Phys. Semiann. Prog. Rep. Sept. 10, 1954*, ORNL-1798, p 60.

ordering, while the maximum at 1.81°K results from a reorientation to a second type of antiferromagnetic ordering. Hence the neutron-diffraction measurements were started in an attempt to learn the details of the magnetic structure of $MnCl_2$ in this low-temperature region.

Preliminary measurements have been obtained for both polycrystalline samples and single crystals at temperatures down to 1.39°K. Data were obtained first on powdered samples, and, while the diffraction pattern at 1.39°K indicated the presence of antiferromagnetic reflections, the intensities were too weak to be significant. Several cylindrical pillars were then cut from a large single crystal along specific crystallographic directions, and a search was made for magnetic reflections from these pillars. In addition to the nuclear-scattering peaks, the patterns at 1.39°K showed antiferromagnetic reflections from a $(00l)$ plane and an $(h0l)$ plane (indexed in terms of a hexagonal lattice). Both reflections occurred at angular positions which indicated that the magnetic unit cell was much larger than the chemical unit cell. Unfortunately, the samples were not good single crystals, and the diffraction peaks were very broad and unsymmetrical. Therefore the data were not sufficiently reliable for the observed reflections to be assigned to definite crystallographic planes. There was no significant change in the intensity of the nuclear-scattering peaks between 4.2 and 1.39°K, which indicated the absence of ferromagnetic ordering, in agreement with the susceptibility measurements.

The neutron intensity of the $(h0l)$ magnetic reflection was studied as a function of temperature in the region from 2.5 to 1.39°K. The data showed a sharp increase in intensity at about 1.9°K and a continued increase along a typical saturation magnetization curve to the lowest temperature of 1.39°K. Hence the Neél temperature predicted by neutron-diffraction measurements coincides with the temperature region of the specific-heat and susceptibility anomalies. These measurements, however, do not establish conclusively the exact temperature at which the magnetic reflection appears or whether there may be a complex behavior of the neutron intensity of this reflection in the temperature range from 1.81 to 1.96°K. Additional experiments will be performed when better single crystals of $MnCl_2$ are available.

3.3 A NEW STRUCTURE IN THE PEROVSKITE-TYPE COMPOUNDS $(La,Ca)MnO_3$

E. O. Wollan W. C. Koehler

In previous semiannual reports the magnetic structure associated with the systems of perovskite-type compounds $[(1 - x)La, xCa]MnO_3$ has been discussed. It has been seen that these compounds are purely ferromagnetic over a relatively narrow range of compositions ($x \sim 0.35$) and show simultaneous occurrence of ferromagnetic and antiferromagnetic phases in the ranges ($0 < x < 0.25$) and ($0.40 < x < 0.50$). Several types of antiferromagnetic structures have also been described:[6] type A at $x = 0$, type C at $x = 0.75$, and type G at $x = 1.0$.

A further study of samples in the composition range $0.5 < x < 0.75$ has now shown that some diffraction patterns cannot be accounted for by any of the cell types[6] A through G or as incoherent mixtures of these magnetic structures. The first evidence for a more complicated magnetic structure came from a pattern which showed a broad peak at small angles when observed with the normal angular resolution. A difference pattern for a sample of $(0.5\ La–0.5\ Ca)MnO_3$ containing 58% Mn^{4+} and taken with Soller slits for higher resolution is shown in Fig. 3.6.

The smallest unit cell upon which it is possible to index the observed magnetic reflections of this pattern is one which has $a = b = \sqrt{2}c$, where c is twice the Mn–Mn separation. The new a and b

[6] These structure types were illustrated previously: E. O. Wollan and W. C. Koehler, *Phys. Semiann. Prog. Rep. Sept. 10, 1954*, ORNL-1798, p 43 (Fig. 3.2).

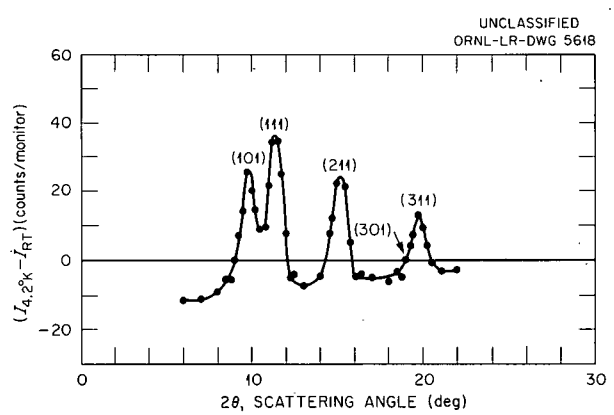

Fig. 3.6. Temperature-Difference Pattern for (0.42 La – 0.58 Ca)MnO_3 Taken with Soller Slits.

axes are thus face diagonals of a cell which is doubled along all three edges of the simple perovskite cube of the double cell (see Fig. 3.7). The observed reflections, which represent only a small fraction of those possible for this cell, fall into two groups. In the one, single reflections (excluding permutations of indices) are observed with l odd, (101), (121), (301), etc.; and, in the other, contributions to a given peak can arise from superimposed even and odd l index reflections, (111) and (200), (311) and (202), etc. No single reflections with even l index are found, nor are any reflections observed for planes of the form (00l). Attempts to interpret the pattern with nonvanishing (200) and (202) reflections were not successful, and hence the reflections in the latter group were ascribed to the (111) and (311) reflections only. On this basis all the observed reflections have l odd, and this calls for a cell with all ions antiferromagnetically coupled in the *c* direction. The above considerations and a consideration of other absent reflections, together with the fact that planes which contribute intensity cannot have a vanishing net spin, lead to the arrangement of spins shown in Fig. 3.7.

It is interesting to observe that this spin arrangement can be developed by the coherent stacking of octants of the C- and E-type structures as shown by the octant labels in the structure diagram presented previously.[6] This stacking feature has led to the designation of this structure as the C-E type. In the C-E type structure, the same simple ferro- and antiferromagnetic neighbor relations are present as in the case of the C-type alone.

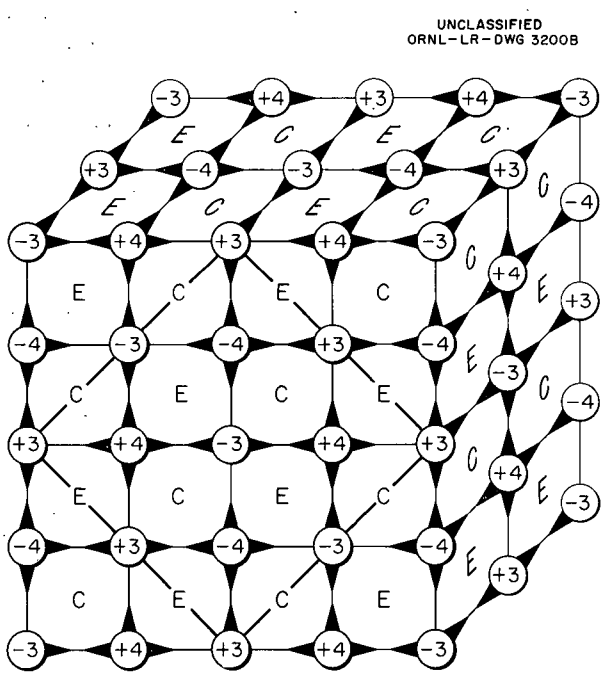

Fig. 3.7. C-E Type Structure.

In the case of these mixed oxides the magnetic structures may be associated with an ordering of the Mn^{3+} and Mn^{4+} ions on the lattice sites. In the A- and G-type structures this point did not enter. For the C-type structure the intensities are rather insensitive to ion ordering, and no direct information on this point could be obtained from the data. This is not true, however, for the C-E structure, for which the predicted intensities are for some cases quite sensitive to the assumed distribution of the Mn^{3+} and Mn^{4+} ions on the lattice sites.

Before considering the effects of ion ordering, it will be well to establish independently, if possible, the orientation of the spins relative to the crystalline axes. Calculations relative to both these points are brought together in Table 3.1. The first column gives the indices of the observed reflections based on the C-E type structure. The second column lists the values of q^2jF^2 deduced from the measured intensities in the pattern, and succeeding columns list calculated values of this quantity. The first group of calculated values refers to a structure in which the Mn^{3+} and Mn^{4+} ions in equal proportions are distributed at random on the various lattice sites. Columns *a*, *b*, and *c* refer to the axis to which the spin vector has been assumed to be parallel. Although the agreement with the data is in no case very good, the low value predicted for the (301) reflection in the first column of this group suggests that the spins are oriented along the *a* axis. The fact that the calculations were made for a (50–50) ion composition, whereas the sample analysis gave (42–58), has no effect on the relative values.

For the calculations involving ordering of the ions on lattice sites, two types of ordering have been considered. One type results from simple phenomenological arguments about the types of indirect coupling between the magnetic ions in this system which are consistent with most of the data. The rules thus established which were discussed in more detail previously,[7] call for the indirect

[7] E. O. Wollan and W. C. Koehler, *Phys. Semiann. Prog. Rep. Sept. 10, 1954*, ORNL-1798, p 42–45.

TABLE 3.1. COMPARISON OF OBSERVED AND CALCULATED q^2jF^2 VALUES FOR C-E TYPE STRUCTURE

hkl	q^2jF^2 (10^{-24} cm^2 per atom)						
	Observed	Calculated					
		Disordered			Ordered		
		(50–50)*			(50–50)	(42–58)	(44–56)
		*a***	*b*	*c*	*a*	*a*	*a*
101	0.45	0.49	0.74	0.25	0.64	0.33	0.40
111	0.75	1.06	1.06	0.71	0.78	0.78	0.78
121	0.82	1.05	0.45	0.75	1.37	0.71	0.86
301	0.1	0.09	0.49	0.41	0.12	0.05	0.07
311	0.85	1.11	1.11	1.59	0.82	0.82	0.82

*Numbers in parentheses refer to per cent Mn^{3+}–Mn^{4+}.

***a*, *b*, *c*, refer to axis along which spin is oriented.

coupling in the region ($x > 0.5$) to be ferromagnetic between unlike pairs and antiferromagnetic between like pairs of ions. The ion ordering obtained on the basis of these criteria puts Mn^{3+} and Mn^{4+} ions in positions for which the major intensity contributions are the same as for a disordered lattice. The ordering would lead to other non-vanishing reflections than those corresponding to the few observed lines in the pattern, but they would have been too weak to have been observed.

The other type of ordering was suggested from a study of the pattern, and it is of interest to observe that it fits well into a coupling scheme suggested by Goodenough.[8] This type of ion ordering is the one illustrated in the drawing of the C-E structure in Fig. 3.7.

For a pure structure of this type, the (101), (121), (301), etc., reflections would result from scattering by one kind of ion only, and the (111), (311), etc., reflections would result from the other kind only. Unfortunately, the sample from which the pattern under consideration was obtained did not have a (50–50) ion composition, the results of the chemical analysis being (42–58). This fact makes it impossible to verify definitely this proposed type of ion ordering, since additional assumptions must be made about the disposition of the excess Mn^{4+} ions.

[8] J. B. Goodenough, private communication.

Calculations relative to this type of ordering are given in the last three columns of Table 3.1. The first column was calculated for the ideal composition. For the other two columns, correction for composition was made on the assumption that the excess Mn^{4+} ions go at random, but with opposite spin, into sites occupied by Mn^{3+} ions in the ideal structure. The last column, which agrees well with the experimental data, was calculated for a slightly different composition than that given by the analysis but within the errors of the analysis.

The assumption that excess Mn^{4+} ions go into the Mn^{3+} sites with reversed spin is not completely arbitrary. If the C-E type of arrangement is examined, it is observed that a C-type structure can be obtained by reversing half the spins of ions on the Mn^{3+} sites, provided that specific spins are so reversed. If this spin reversal is a result of the addition of Mn^{4+}, then it would be expected that the C-type structure should set in at a 75% Mn^{4+} concentration. Such a structure is in fact observed at 80% Mn^{4+}. It would seem reasonable to assume that in the early phases of this transformation the excess Mn^{4+} would go into the Mn^{3+} sites at random. A series of observations which suggested that this model for the transformation may be correct is shown in Fig. 3.8, where the first pair of reflections (101) and (111) are represented for various ion concentrations over the range 50–80% Mn^{4+}. The intermediate compound

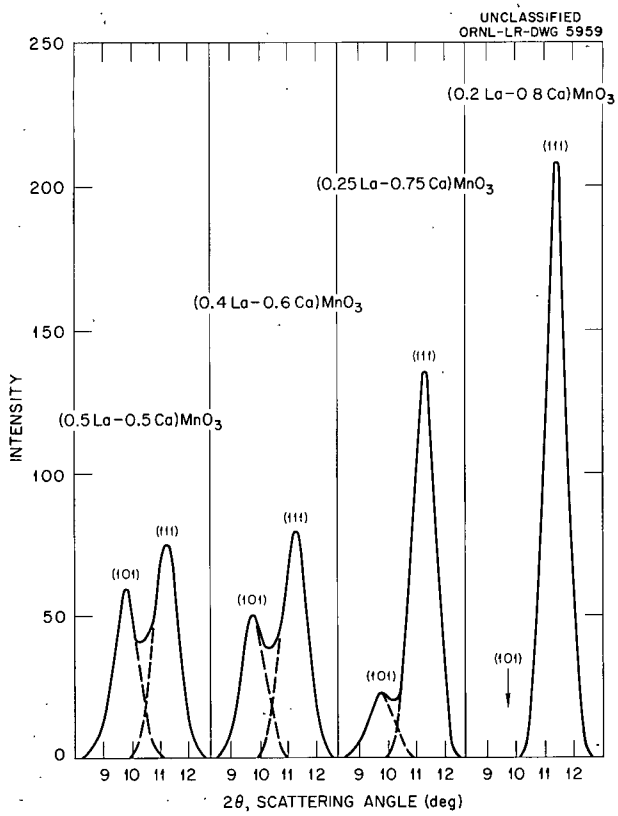

Fig. 3.8. First Two Lines of Four Patterns Showing Growth of C-Type Structure (Right) from C-E Type (Left).

(75 La–25 Ca)MnO_3 is interesting in that it shows a much increased (111) reflection and a correspondingly decreased (101) reflection, and this indicates the approach to the C-type structure.

In connection with this C-E structure, one point should be mentioned. The above discussion relative to the deduction of the spin arrangement in this structure has assumed a single magnetic phase. Under the conditions that the structure is in fact defined by the unit cell described above and that there is antiferromagnetic coupling between adjacent layers, it can be concluded, by exploring all of a reasonable number of possible spin arrangements, that the spin arrangement mentioned is unique. However, measurable intensities may also be put into, and only into, the positions observed in the pattern of Fig. 3.7 by an incoherent mixing of two phases: (1) the C type which will reflect only into the (111), (311), etc., positions and (2) a cell of the same dimensions as C-E but built up of arrested type-E octants which would reflect only into the (101) and (301), etc., positions. If one makes reasonable assumptions about the moment directions in this latter arrangement and attempts to fit the observed intensities as an incoherent mixture of phases, one is led to inconsistencies which suggest the improbability of the incoherent mixture.

The type of structure transition suggested above from C-E to C type is also supported by low-temperature x-ray diffraction studies of four samples in the range ($0.50 < x < 0.80$); three are evidently C-E type and undergo a tetragonal splitting with $c/a < 1$. The fourth, which is C type, splits tetragonally with $c/a > 1$. It is of interest to note that the splitting occurs at a temperature considerably in excess of the Neél point, and it has been suggested by Goodenough[8] that the crystallographic distortions are due to an ordering of covalent bonds in such a way as to minimize the elastic distortions while permitting the formation of the optimum number of covalent bonds. In pursuing these arguments, Goodenough has been led to predict a system of ionic ordering which is in agreement with the neutron-diffraction observations and thus lends support to our proposed structure assignments.

3.4 FERROMAGNETIC- AND ANTIFERROMAGNETIC-MOMENT DATA FOR THE $[(1-x)La, xCa]MnO_3$ SERIES OF COMPOUNDS

E. O. Wollan W. C. Koehler

The magnetic-moment data which have been obtained for this series of compounds[9] are presented graphically as a function of sample composition in Fig. 3.9. In the discussion of the figure, it is necessary to show how the plotted quantities are obtained from the measurements.

In the neutron-diffraction experiments the measured quantities are the absolute values of the integrated power in the various magnetic reflections. From the power in a given peak and the known parameters, one obtains the quantity which can, for all the cases to be considered here, be represented as $q^2 j F^2_{hkl}$, where j is the multiplicity of the set of planes hkl and $q^2 = 1 - (e \cdot k)^2$, where e is the unit scattering vector and k is a unit vector in the direction of alignment $q^2 = \frac{2}{3}$ for all reflections; hence no information can be obtained

[9] E. O. Wollan and W. C. Koehler, *Phys. Semiann. Prog. Rep. March 10, 1954*, ORNL-1705, p 34; *Phys. Semiann. Prog. Rep. Sept. 10, 1954*, ORNL-1798, p 42.

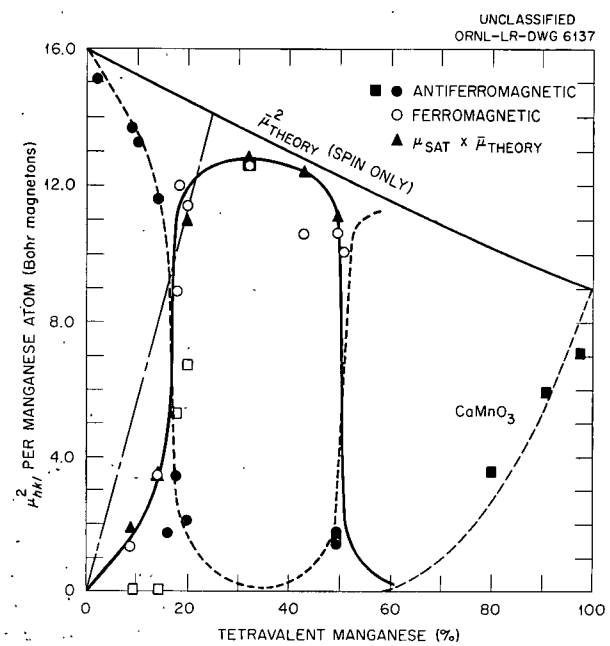

Fig. 3.9. Ferromagnetic and Antiferromagnetic Moments vs Sample Ion Composition.

about the moment orientation in the lattice. For other structures, such as type A, the intensities in the pattern depend upon the moment orientation relative to the crystalline axes, and therefore in such cases information relative to the moment orientation can be obtained. When q^2 has been evaluated for a given magnetic system, one can obtain the quantity μ_{hkl}, which is defined in terms of the measured quantity $|F_{hkl}|^2$ as

$$(1) \quad \mu_{hkl} = \frac{|F_{hkl}|}{n\left(\frac{e^2\gamma}{2mc^2}\right) f(\theta)} = \frac{1}{n}\sum_n \mu_n e^{i\phi_n} e^{2\pi i(hx_n + ky_n + lz_z)},$$

where γ is the neutron magnetic moment, $f(\theta)$ is the form factor of the magnetic electrons and is assumed here to be the same for all the ions in the system, μ_n is the magnitude of the ionic moment, and $\phi_n = 0$ or π for orientation parallel or antiparallel to the direction of alignment of the spin system. The sum is to be taken over the n atoms of a unit cell. For a system which has some degree of randomness in the location of the moments on the lattice sites, proper account must be taken of the randomness in applying Eq. 1 to the observations.

The values of μ_{hkl} obtained from the measured intensities may involve the individual ionic moments in different ways, depending upon the structure and upon the particular reflection hkl considered. In succeeding paragraphs the measured quantities of μ^2_{hkl} are interpreted in terms of the individual ionic moments for a number of cases experimentally encountered, and these are the quantities which are plotted in Fig. 3.9. This representation has been adopted to put on a single plot as much of the magnetic data as possible, although this is not entirely satisfactory for all aspects of the problem.

For the pure A- and G-type structures, where there is only one kind of magnetic ion, the value of μ_{hkl} as obtained from the observed F_{hkl} values yield the magnetic moment per Mn^{3+} or Mn^{4+} ion, respectively. It is seen that for the purest $LaMnO_3$ sample ($\sim$2% Mn^{4+}) the point on the graph is in good agreement with the expected value. The $CaMnO_3$ case will be considered later.

For the magnetic structure involving mixed Mn^{3+} and Mn^{4+} compositions, an evaluation of the ionic moments requires, in general, a determination of the type of ionic ordering on the lattice sites. For the ferromagnetic case the reflections with all indices even give $\mu_{hkl} = p_3\mu_3 + p_4\mu_4$, where p_3 and p_4 are the fractional Mn^{3+} and Mn^{4+} contents, respectively, and μ_3 and μ_4 refer to the magnitudes of the moments of trivalent and tetravalent ions, respectively. This is the same result that would be obtained for a random distribution of Mn^{3+} and Mn^{4+} ions over the lattice sites. In any case, $\bar{\mu}_F = p_3\mu_3 + p_4\mu_4$ is the weighted average moment per ion in the ferromagnetic lattice, and it is the square of the quantity, as determined from the neutron intensities, which is plotted in Fig. 3.9.

In the mixed-phase region $0 < x < 0.25$, the measured values of $q^2 j F^2_{hkl}$ for the two types of phases A and B should be proportional to $p_A\bar{\mu}^2_A$ and $p_F\bar{\mu}^2_F$, respectively, in which p_A is that fraction of the atoms in the sample which are associated with long-range antiferromagnetic ordering and where p_F is the corresponding fraction of long-range ferromagnetic ordering. The average moment per ion in the ferromagnetic phase is denoted by $\bar{\mu}_F$ and has the definition given above. The

average moment per ion in the antiferromagnetic phase $\bar{\mu}_A$ would be μ_3 if all the available Mn^{4+} ions tended to cluster in the ferromagnetic phase or would be $p_3\mu_3 + p_4\mu_4$ if a fraction p_4 of the ions in the antiferromagnetic phase was tetravalent.

In Fig. 3.9 the effective squared moments $p_F\bar{\mu}_F^2$ and $p_A\bar{\mu}_A^2$ have been plotted as a function of ion concentrations. The long-range ferromagnetic order is seen to develop very rapidly near $x = 0.15$, approaches full development in the vicinity of $x = 0.25$, and remains large until x approaches 0.5. These results tend to lend support to the previously proposed[10] ionic ordering schemes B-6-2 and B-4-4.

Information on the ferromagnetic moments was also obtained from direct magnetic saturation measurements. In the case of incoherent mixtures of ferro- and antiferromagnetic phases, one would expect the observed saturation moment per magnetic ion in the sample to be given by $\mu_{Sat} = p_F\bar{\mu}_F$, where, as previously, p_F represents the fraction of the magnetic ions which are ferromagnetically aligned with an average moment $\bar{\mu}_F$. Comparison of these measurements with those obtained from neutron diffraction, which gives $p_F\bar{\mu}_F^2$, is conveniently done by plotting in Fig. 3.9 the quantity $\bar{\mu}_{Sat} \times \bar{\mu}_F = p_F\bar{\mu}_F^2$, where the multiplying factor $\bar{\mu}_F$ is taken as the spin-only value appropriate to the particular Mn^{4+} concentration. These data are represented by the triangles in the figure, and it is seen that they agree quite closely with the open circles from neutron-diffraction measurements.

For the C-E type of structure observed at an Mn^{4+} content of about 58%, the values of μ_{hkl}^2 obtained from the data can, as has been described, lead to an estimate of the moments occupying the several types of lattice sites. For the ordering shown in Fig. 3.7 and for the ideal composition, there will be two values of μ_{hkl}^2, of which one is proportional to μ_3^2 and the other to μ_4^2. The departure of sample from the ideal stoichiometric composition was shown to introduce modifications in the intensity pattern, which could be accounted for if the excess Mn^{4+} ions were introduced into the Mn^{3+} sites at random but with reversed spin. In this case the observed μ_{hkl}^2 for the Mn^{3+} sites can be said to be proportional to $\bar{\mu}_3^2$, where $\bar{\mu}_3 = p_3\mu_3 - p_4\mu_4$ and is the weighted average, taking into account the spin reversal, of the moments of the ions on the ideal Mn^{3+} sites. For this, an average magnetic moment cannot be defined in the sense described above, and hence no entry for this case is made in Fig. 3.9.

In the case of the C-type pattern, the μ_{hkl} values for reflections (110), (112), (130), etc., will all be proportional to $p_3\mu_3 + p_4\mu_4 = \bar{\mu}_A$ irrespective of the type of ordering, provided that where there are misfits there are no spin inversions. That this seems to be the case is indicated by the fair agreement of the observed $\bar{\mu}$ value with that expected from the above model (2.99 observed vs 3.20 calculated). The observed value is, however, somewhat lower than was expected and may represent an incomplete development of the structure. Accordingly, for this case also, no entry has been made in Fig. 3.9.

The suggested growth of antiferromagnetic phases in the region $x > 0.5$ is indicated by a rising and leveling-off of the antiferromagnetic-moment curve in this region.

The G-type structure is apparently stable for compositions greater than $x = 0.8$. For this structure, only reflections which have all indices odd are permitted, and for them $\mu_{hkl} = p_4\mu_4 \pm p_3\mu_3 = \bar{\mu}_A$. The plus sign is to be taken if the Mn^{3+} ions in compositions different from $x = 1$ replace Mn^{4+} with the same spin, and the negative sign if they go into the lattice with spin opposite to the replaced Mn^{4+} ions. The predicted curve for this latter case is shown in Fig. 3.9, and it seems to agree well with the observed points. For the first case the average moments would have increased with Mn^{3+} content.

[10] E. O. Wollan and W. C. Koehler, *Phys. Semiann. Prog. Rep. Sept. 10, 1954*, ORNL-1798, p 42.

4. LOW-TEMPERATURE PHYSICS – NUCLEAR ALIGNMENT

4.1 BRUTE-FORCE POLARIZATION OF In^{115} NUCLEI

J. W. T. Dabbs, Jr. L. D. Roberts
S. Bernstein

Experiments have been successfully completed on the polarization of In^{115} nuclei by application (at a very low temperature) of a magnetic field directly to the nuclear magnetic moments. Indium metal, in the form of thin plates, was thermally connected to a cooling salt by soldering to silver wires which were embedded in the cooling-salt sample of $Fe(NH_4)(SO_4)_2 \cdot 12H_2O$ some 12 cm below. This salt was cooled by adiabatic demagnetization from 0.99°K and 16,400 gauss to a final temperature near 0.035°K. The sample unit was then lowered[1] to place the cooling salt inside a magnetic shield, where the field was less than 2 gauss, and to bring the indium plates into the gap of the Weiss magnet. The magnet was then turned on very slowly (to minimize eddy currents) to 11,150 gauss.

The nuclear sample was then bombarded with polarized thermal neutrons, and the intensity of the transmitted beam was measured with the neutron polarization parallel to, and antiparallel to, the nuclear polarization direction. A maximum change in transmission of approximately 7.0 ± 0.9% was observed on reversal of the neutron spins. (This was the average of four runs.) The change reached the maximum about 30 min after application of the field to the indium nuclei and then decayed away slowly; the change was followed for about 2 hr in each experiment. The change, corrected for background, is shown in Fig. 4.1. The counting rate was about 900–1200 counts/min, with backgrounds of about 90–120 counts/min. Alternate 5-min counts were made, with each neutron-spin direction being used throughout the counting period. Repetition of the experiment at 4.2°K gave no effect within statistics.

The direction of the observed change was the same as that found in the results reported previously[2] (where only a 0.5% effect was observed); that is, the cross section was larger when the spins were parallel. This corresponds to an angular momentum $J = I + 1/2 = 5$ for the compound nucleus In^{116} in the state corresponding to the 1.458-ev neutron resonance in In^{115}. This result disagrees with that of Brockhouse.[3]

The major difference between the present result and that previously reported lies in changes in the disposition of the neutron-polarization apparatus.[2] Reduction of the intensity of neutrons actually striking the nuclear sample was accomplished by diffraction of the neutrons from the (220) planes of a magnetized Fe_3O_4 crystal and, subsequently, from the (111) planes of a copper crystal. The first diffraction[4] polarized the neutrons to about 87%, and the second served the dual purpose of reducing the second-order content of the diffracted beam and of redirecting that beam in such a way that the bulky cryogenic equipment did not have to be moved from its previous location. The neutron energy selected in the diffractions was 0.075 ev in first order.

Reversal of the neutron spins, with respect to the magnetic field applied to the nuclear sample, was accomplished by manipulating the stray field

[1] S. Bernstein *et al.*, *Phys. Rev.* **94**, 1243 (1954).
[2] J. W. T. Dabbs, Jr., *et al.*, *Phys. Semiann. Prog. Rep. Sept. 10, 1954*, ORNL-1798, p 57.
[3] B. N. Brockhouse, *Can. J. Phys.* **31**, 432 (1953).
[4] C. P. Stanford *et al.*, *Phys. Rev.* **94**, 374 (1954).

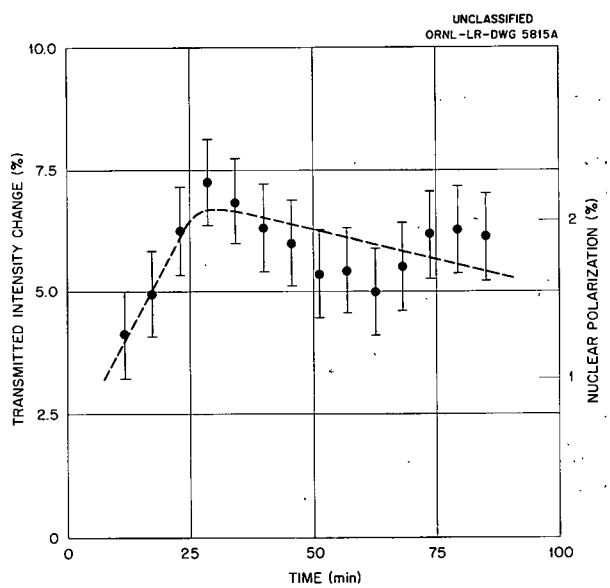

Fig. 4.1. Observed Change in Neutron Transmission of Polarized In^{115} Nuclei with Reversal of Relative Spin Orientation of Neutrons and Nuclei.

in the region near the second crystal with rectangular air-core coils, which merely added (or subtracted) essentially constant fields to the stray field already present. This stray field had a gradient in one component of about 3 gauss/cm; by reducing other components nearly to zero, a transition probability of approximately 90% was obtained in a reproducible manner. By adding to other components, a transition probability near zero was obtained. The theoretical expression for this transition probability is given by

$$(1) \qquad W\left(-\frac{1}{2}, \frac{1}{2}\right) = e^{-0.039H_x^2/\nabla H_y}$$

for 0.075-ev neutrons and is derived from the work of Majorana.[5] In Eq. 1, the field H_x is any constant component; ∇H_y is the gradient of a component perpendicular to H_x taken along the neutron path. The third component is assumed to be zero.

The lowest temperature attained by the nuclear sample may be calculated from the observed change in transmission, and was about 0.043 ± 0.005°K. This corresponds to a nuclear polarization of 2.1%. There is some possibility that such measurements may serve as reliable "thermometers" in the region of temperature 0.0001 to 0.05°K.

These experiments constitute the first demonstration of a macroscopic nuclear polarization obtained by direct interaction of an external magnetic field with nuclei, and, with further development, they suggest the possibility of the attainment of extremely low temperatures by nuclear demagnetization.

4.2 EXTENSION OF MOLECULAR-FIELD THEORY TO A HEXAGONAL LATTICE

R. B. Murray L. D. Roberts

The Van Vleck molecular-field theory of antiferromagnetism has recently been extended by Anderson[6] and by Smart[7] to the cases of face-centered and body-centered cubic lattices, taking into account exchange interactions with second-nearest neighbors as well as first neighbors. These treatments predict several types of magnetic order in a particular lattice, the type of order depending on the sign and magnitude of the exchange interactions between first- and second-nearest neighbors.

In the course of an investigation[8] of the cryomagnetic properties of $MnCl_2$, it became of interest to apply the molecular-field theory to the $MnCl_2$-type lattice, a hexagonal layer structure. The purpose of this calculation is to determine the various types of magnetization predicted by the theory for each of the four possible combinations of ferromagnetic and antiferromagnetic first- and second-nearest-neighbor interactions. The hexagonal lattice is divided into six sublattices, where the first neighbors of a given ion are disposed in a hexagonal arrangement in the same plane, while the second-nearest neighbors are located in adjoining planes. Interactions with ions other than the first and second neighbors are considered to be negligible by virtue of the short range of exchange forces.

The results of the calculation predict three possible types of magnetic order: (1) ferromagnetism, (2) an antiferromagnetic state composed of ferromagnetically ordered layers with adjacent layers oppositely oriented, and (3) an antiferromagnetic state in which the vector sum of the moments of any three neighboring atoms in a layer is zero. This last condition may be fulfilled by a triangular net arrangement of the spins within a layer, and it would result in a state in which there is no unique antiferromagnetic axis as is assumed in the Van Vleck theory. This calculation further predicts the possibility of magnetic-structure transitions from one type of order to another if the interaction parameters are assumed to be temperature dependent.

This model may be applicable to certain anhydrous iron-group chlorides which crystallize in the hexagonal layer structure, for example, $MnCl_2$, $FeCl_2$, $CoCl_2$, and $NiCl_2$. These compounds become antiferromagnetic at low temperatures; however, the magnetic structures are unknown at the present time.

[5] E. Majorana, *Il Nuovo Cimento* 9, 43 (1932).

[6] P. W. Anderson, *Phys. Rev.* 79, 705 (1950).

[7] J. S. Smart, *Phys. Rev.* 86, 968 (1952).

[8] R. B. Murray, L. D. Roberts, and R. A. Erickson, *Phys. Semiann. Prog. Rep. Sept. 10, 1954*, ORNL-1798, p 60.

4.3 EFFECT OF CRYSTALLINE ELECTRIC FIELDS ON ANTIFERROMAGNETIC TRANSITIONS

L. D. Roberts R. B. Murray

The Van Vleck molecular-field theory of antiferromagnetism considers only exchange interactions between nearest-neighbor magnetic ions. The influence of crystalline-electric-field splittings of the spin multiplet of an S-state ion such as Mn^{++}, however, has the effect of introducing an additional term into the effective spin Hamiltonian[9] of the form DS_z^2. Here S_z is the z component of the electron-spin angular-momentum operator, and D is the electric-field splitting coefficient arising from the tetragonal component of the crystalline field at the position of the Mn^{++} ion. In a number of antiferromagnetic manganous salts, for example, $MnCl_2$, MnF_2, and $MnSiF_6 \cdot 6H_2O$, the Mn^{++} ion is surrounded by a charge distribution which gives rise to an electric field having a component of tetragonal symmetry at the Mn^{++} site. Accordingly, it is of interest to investigate the influence of the DS_z^2 term on an antiferromagnetic transition.

The procedure adopted in this calculation is simply to modify the original theory by the inclusion of the DS_z^2 term in the spin Hamiltonian given by Van Vleck.[10] Assuming the same symmetry axis for the electric field as for the molecular field, the modified Hamiltonian is of the form

$$\mathcal{H} = DS_z^2 - g\beta S_z H_e ,$$

where H_e is the effective molecular field,[10] β is the Bohr magneton, and g is the Landé spectroscopic splitting factor. The thermodynamic quantities of interest may then be calculated, by employing standard magnetic theory, from the partition function $Z = \Sigma e^{-\mathcal{H}/kT}$. The calculation is carried out for a spin 5/2 system.

[9] M. H. L. Pryce, *Phys. Rev.* 80, 1107 (1950).

[10] J. H. Van Vleck, *J. Chem. Phys.* 9, 85 (1941).

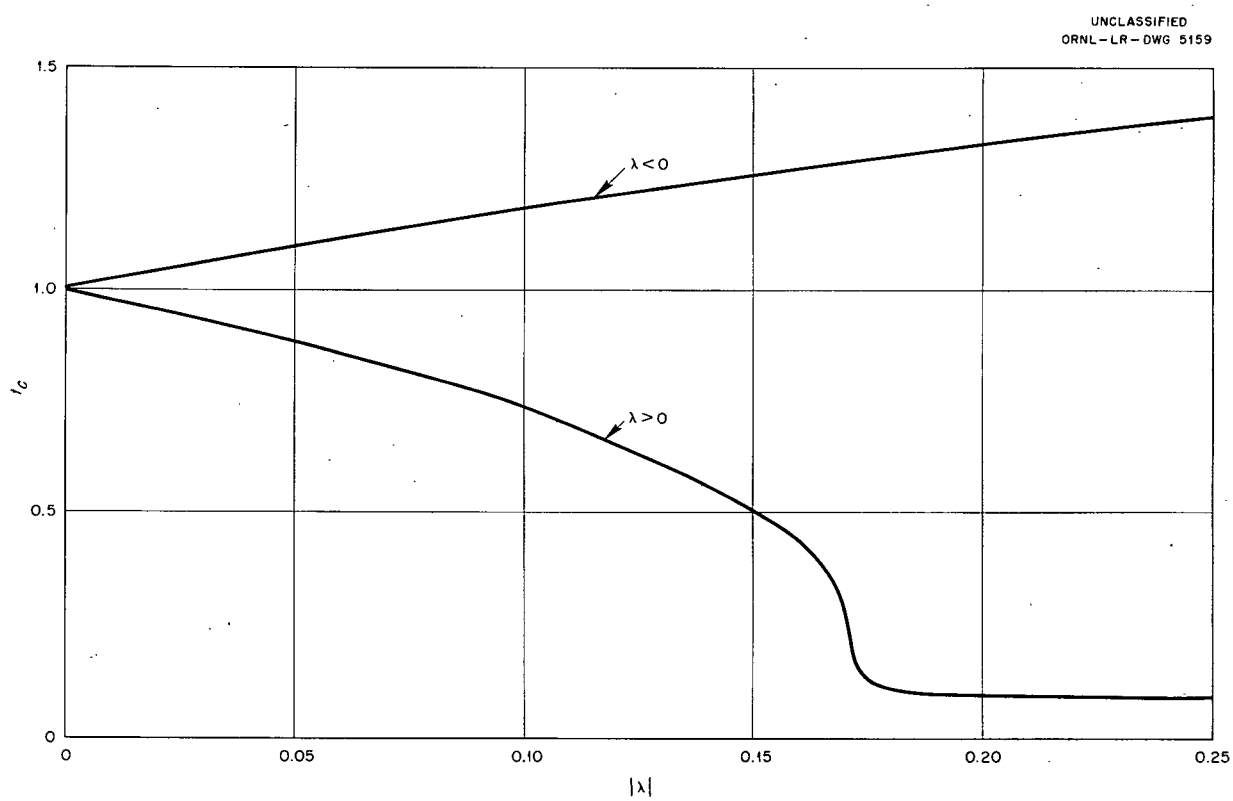

Fig. 4.2. Dependence of t_c on λ.

We denote by $t_c \equiv T_c/T_0$ the ratio of the antiferromagnetic critical temperature in the presence of the D term (T_c) to that in the absence of the D term (T_0). We further define a dimensionless parameter λ as $\lambda \equiv D/kT_0$. As D may be either positive or negative, depending upon the particular charge distribution, λ may be of either sign. The results of the calculation indicate that t_c is quite sensitive to λ, as is shown in Fig. 4.2. For $\lambda > 0$, the transition temperature is strongly depressed by the D term, t_c approaching the asymptotic value 0.086 for large λ. For $\lambda < 0$, t_c is greater than 1, approaching 2.14 for large negative λ. The physical basis for such a dependence of t_c on λ is to be found in the nature of the multiplet splitting brought about by the DS_z^2 term. For positive D, the lowest doublet in a spin 5/2 system will be the $\pm 1/2$ doublet; for negative D, the $\pm 5/2$ doublet is lowest. Since the exchange coupling favors an antiparallel orientation of the maximum (5/2) component of the spins, a negative D effectively "aids" the exchange potential in bringing about the transition, whereas a positive D has the opposite effect.

The reduced magnetization $S_0 = M/Ng\beta$ of an antiferromagnetic sublattice as a function of the reduced temperature $t \equiv T/T_0$ is shown in Fig. 4.3. The temperature t at which S_0 vanishes determines the transition temperature (see Fig.

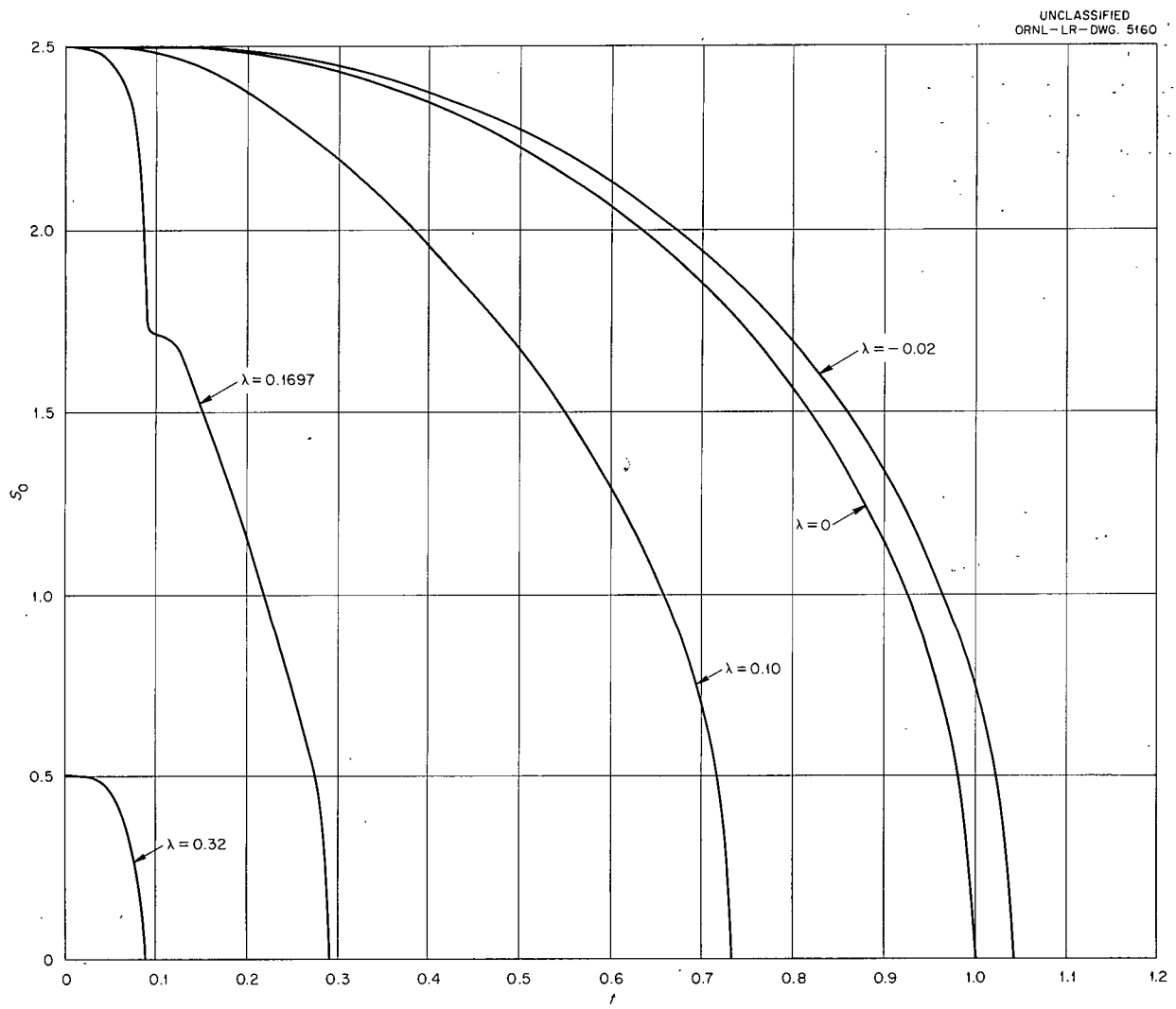

Fig. 4.3. Behavior of Magnetization for Various Values of λ.

4.2). It is found that for large positive λ ($\lambda > 9/35$) the saturation value of S_0 is 1/2 rather than 5/2. For $\lambda \sim 0.2$ the behavior of the S_0 vs t curves is complex; an example is shown for $\lambda = 0.1697$. A calculation of the magnetic susceptibility parallel to the antiferromagnetic axis for various λ reveals that the susceptibility rises smoothly from zero at $t = 0$ and passes through a maximum at t_c.

In this treatment, the calculation of the dependence of t_c and of magnetic properties on λ represents the same degree of approximation as that of the usual molecular-field theory. In this sense, the predicted dependence of t_c on λ should be qualitatively correct, whereas the unusual behavior of S_0 for very small t may be a consequence of the model.

5. HEAVY-ION PHYSICS

P. M. Stier C. F. Barnett

5.1 ELECTRON-CAPTURE AND -LOSS CROSS SECTIONS FOR PROTONS IN VARIOUS GASES

In previous reports,[1,2] the ratios of the electron-loss to electron-capture cross sections were given for each of the ions H^+, He^+, N^+, Ne^+, and A^+ passing through the stopping gases hydrogen, helium, nitrogen, oxygen, neon, and argon; and the cross sections for electron loss by fast hydrogen atoms were reported for the energy range from 20 to 200 kev. During the period of this report, these measurements have been extended for protons to include the interesting energy region from 3 to 20 kev. Also, the electron-capture cross section for protons in the various gases has been measured in the energy range 20 to 200 kev.

Two separate measurements were made in the low-energy (3- to 30-kev) experiment. A determination was made of the fraction of the hydrogen beam which was in each charge state after passage through a thick gas target. Also, the cross section for a natural atom to gain or lose an electron was measured. The apparatus used for these measurements was similar to that used at higher energies and is shown schematically in Fig. 5.1. The ion beam after magnetic analysis was incident on the windowless differentially pumped neutralizer. As a result of charge exchange, the particle beam emerging from this chamber could be of mixed charge. Ions could be removed by electrostatic deflection plates No. 1 (Fig. 5.1). Thus the particle beam incident on the electron-loss chamber could be ions or atoms, or it could have an equilibrium distribution in charge. An electrostatic field could be applied perpendicular to the direction of motion of the particles within the second differentially pumped chamber, so that for a neutral beam incident, ions created by charge exchange could be removed as formed. Thus the observed attenuation as the electrostatic field was applied gave directly the cross section $(\sigma_{01} + \sigma_{0-1})$, where σ_{01} represents the cross section for the loss of an electron by the neutral atom and the formation of a positive ion and σ_{0-1} is the cross section for the formation of a negative ion. A liquid-nitrogen-trapped McLeod gage was used to measure the gas pressure. The third pair of electrostatic deflection plates and the bellows allowed the relative intensity of the positive and negative components of the particle beam to be measured. The detector could be used either as a Faraday cage for ion beams or as a secondary-electron-emission detector for atoms and ions. By taking advantage of the two gas cells, it was possible to avoid the problem of the relative secondary-electron emission for ions and atoms by ensuring that only neutrals, or only equilibrium charge distributions, were incident on the detector.

The results of the measurements of the charge distribution in the hydrogen beam after passage through a "thick" target of the various gases are shown in Figs. 5.2 through 5.7. These data represent the fraction of the particle beam in each possible charge state after passage through enough gas to establish equilibrium between competing capture and loss reactions. The cross sections $(\sigma_{01} + \sigma_{0-1})$ for removal from the neutral state are shown in Figs. 5.8, 5.9, and 5.10. The present results agree well with the previously reported Cockcroft-Walton data. It is observed that, as the energy approaches zero, in nitrogen, oxygen, and argon the tendency is for all the hydrogen beam to be atomic, while in helium and neon most of the beam is positively charged. The latter observation results from the fact that these collisions are violent enough for a hydrogen atom to be ionized by the helium which it is passing through, but it

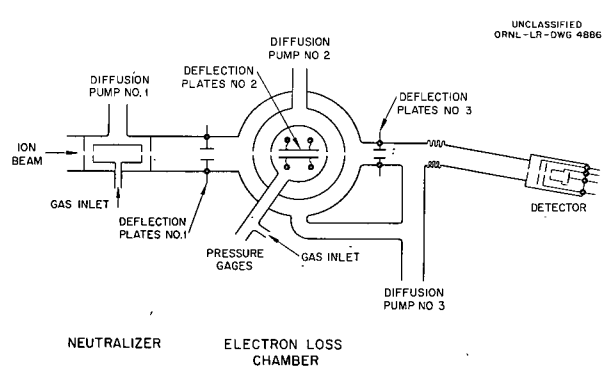

Fig. 5.1. Schematic Drawing of Apparatus Used in Low-Energy Experiment.

[1] P. M. Stier, C. F. Barnett, and G. E. Evans, *Phys. Semiann. Prog. Rep. March 10, 1954*, ORNL-1705, p 43.

[2] P. M. Stier *et al.*, *Phys. Semiann. Prog. Rep. Sept. 10, 1954*, ORNL-1798, p 64.

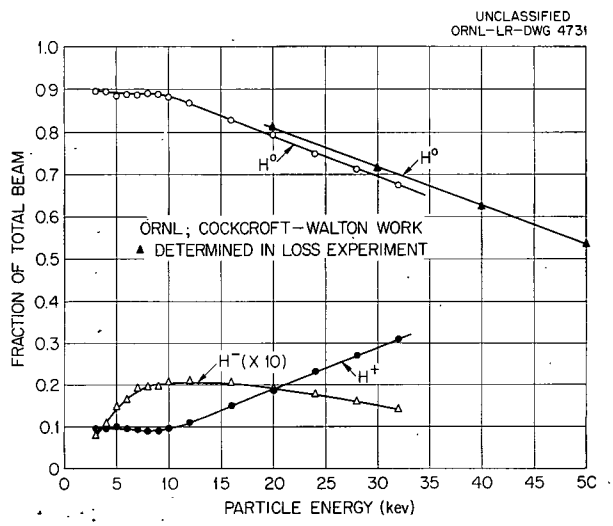

Fig. 5.2. Fraction of H Beam in +1, 0, −1 Charge States After Passage Through "Thick" Target. H in hydrogen.

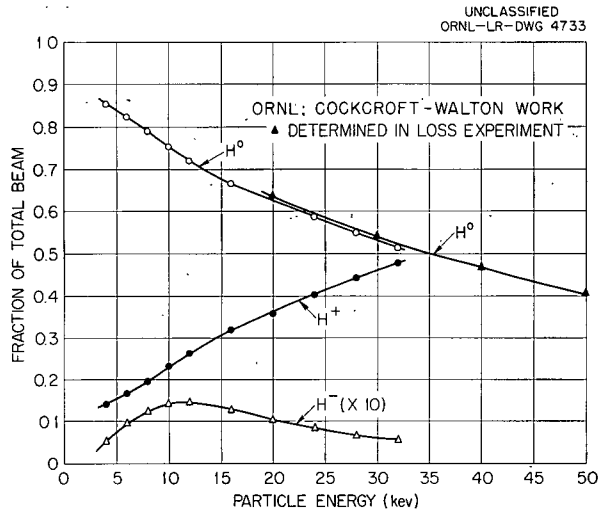

Fig. 5.4. Fraction of H Beam in +1, 0, −1 Charge States After Passage Through "Thick" Target. H in nitrogen.

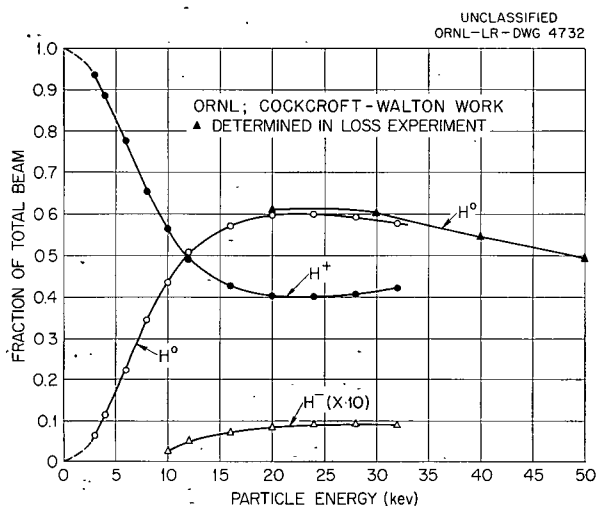

Fig. 5.3. Fraction of H Beam in +1, 0, −1 Charge States After Passage Through "Thick" Target. H in helium.

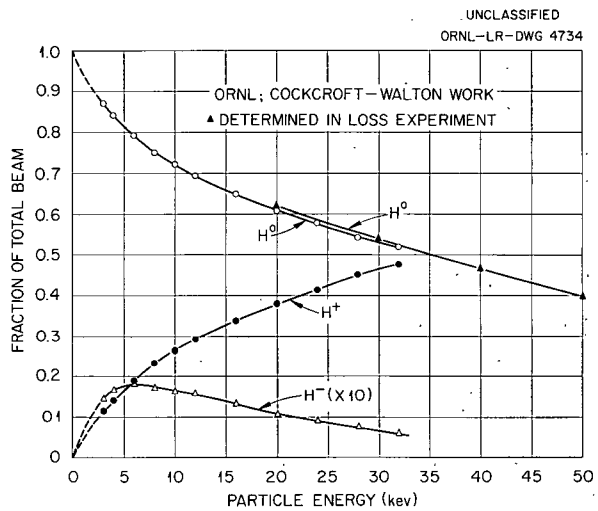

Fig. 5.5. Fraction of H Beam in +1, 0, −1 Charge States After Passage Through "Thick" Target. H in oxygen.

is difficult for a proton to pick up an electron from helium. Intuitively, this is expected from the relative ionization potentials of hydrogen and helium and is similar to the reported[1] behavior of nitrogen and argon ions in helium at higher energies. The plateau in the curve of the fraction of the hydrogen beam which is neutral in hydrogen gas (Fig. 5.2) arises from the secondary maximum in the cross section ($\sigma_{01} + \sigma_{0-1}$) seen in Fig. 5.8. This detail does not appear to be due to the σ_{0-1} contribution to ($\sigma_{01} + \sigma_{0-1}$). From the reported measurements of the cross sections σ_{10} and σ_{-10} for hydrogen ions in hydrogen gas by Whittier[3] and from the present equilibrium data, the cross sections

[3] A. C. Whittier, *Can. J. Phys.* 32, 275 (1954).

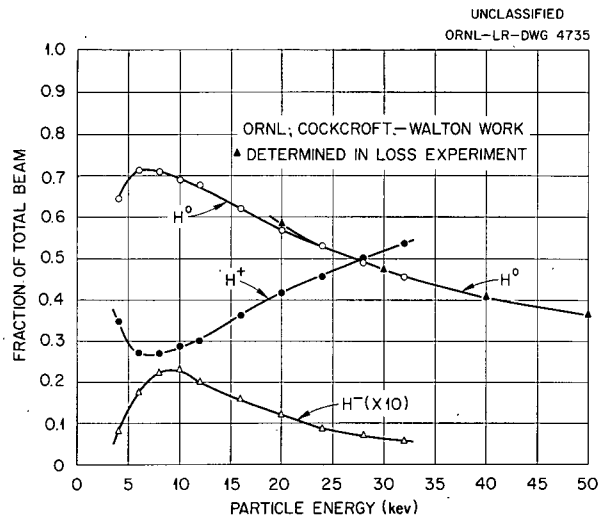

Fig. 5.6. Fraction of H Beam in +1, 0, −1 Charge States After Passage Through "Thick" Target. H in neon.

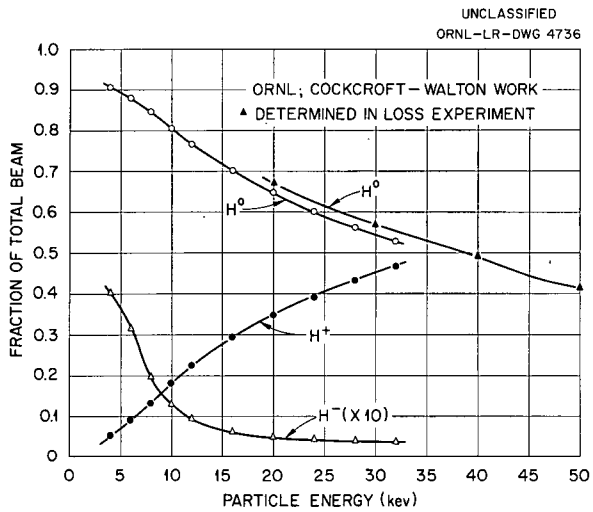

Fig. 5.7. Fraction of H Beam in +1, 0, −1 Charge States After Passage Through "Thick" Target. H in argon.

σ_{01} and σ_{0-1} can be computed, and the submaximum is present in the computed σ_{01}. It should be noted that the computed sum $(\sigma_{01} + \sigma_{0-1})$ agrees well with the curve of Fig. 5.8. Additional experiments are being performed with the aim of establishing the cause of this submaximum.

The electron-capture cross sections have been measured for protons in hydrogen, helium, nitrogen,

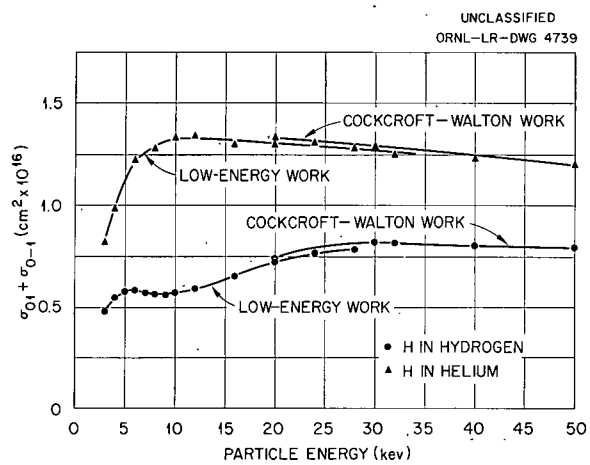

Fig. 5.8. Cross Section $(\sigma_{01} + \sigma_{0-1})$ for H in Hydrogen and for H in Helium.

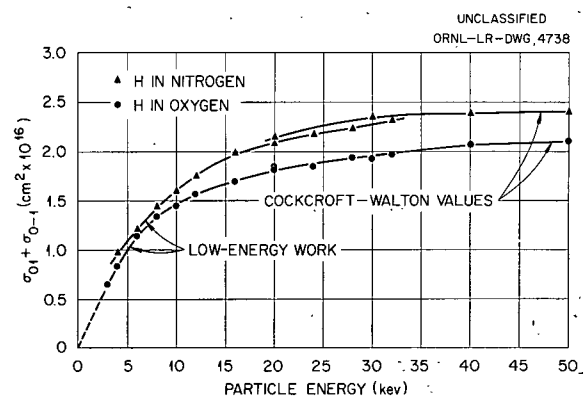

Fig. 5.9. Cross Section $(\sigma_{01} + \sigma_{0-1})$ for H in Nitrogen and for H in Oxygen.

oxygen, neon, and argon for energies 40, 80, 120, and 160 kev. The schematic drawing (Fig. 5.11) represents the apparatus used. The proton beam from the Cockcroft-Walton accelerator was deflected within the differentially pumped gas cell through an angle of 45 deg by the magnetic field. In order to avoid attenuation of the ion beam due to small-angle elastic scattering and in order to maintain the advantage of differential pumping, the ion beam was moved across the exit slit by a linear electrostatic sweep voltage, and the emergent beam was integrated. In the energy range studied, the radius of curvature was sufficiently small so that a proton which captured an electron moved tangentially off the orbit far enough, before any subsequent electron loss, that it did not reach the

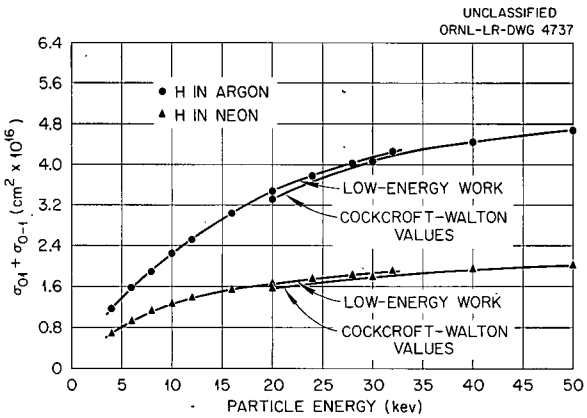

Fig. 5.10. Cross Section ($\sigma_{01} + \sigma_{0-1}$) for H in Argon and for H in Neon.

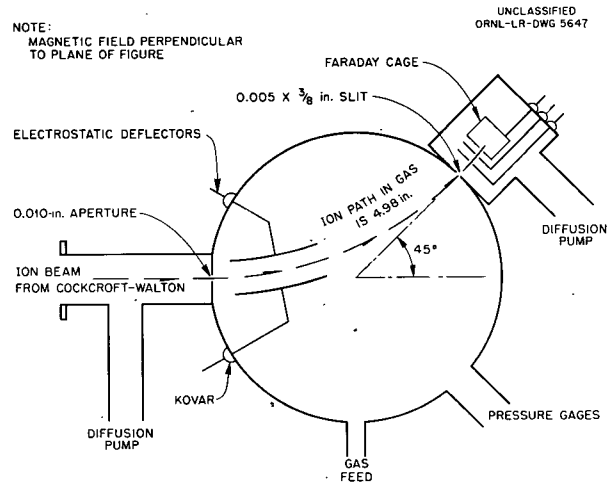

Fig. 5.11. Schematic Drawing of Electron-Capture Apparatus.

detector. If an appreciable number of ions which were recorded had captured and then lost an electron, the measured cross section would have shown some pressure dependence. That this condition was met is evident by the linear dependence of the logarithmic attenuation on the pressure, that is, the pressure independence of the observed cross sections.

In Figs. 5.12 and 5.13 are shown the computed electron-capture cross-section curves previously reported,[2] together with the present results. The agreement is seen to be excellent and represents a consistency which, almost without exception, has not been present in the field of ion interactions. A detailed report of these results is being prepared for publication.

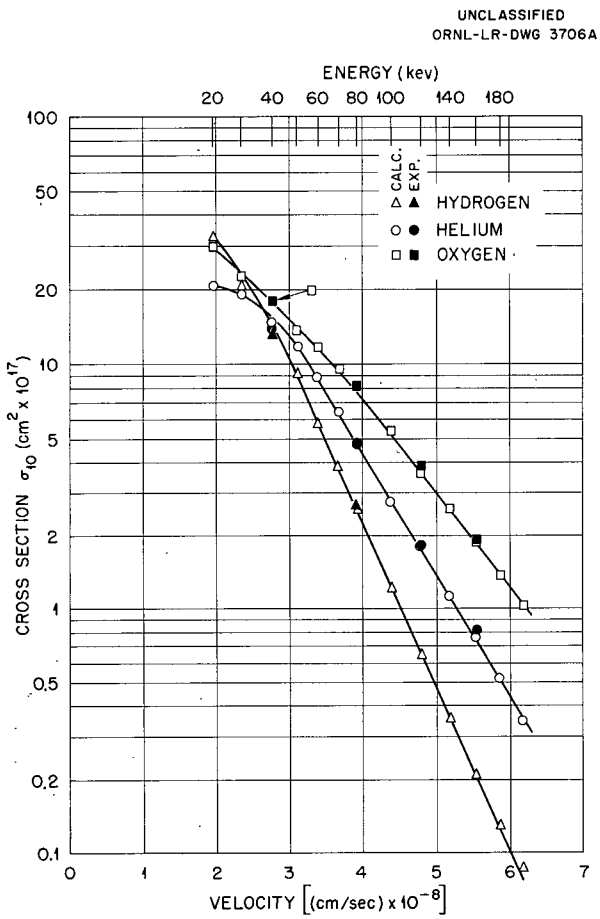

Fig. 5.12. Electron-Capture Cross Section for Protons in Hydrogen, Helium, and Oxygen as a Function of Velocity and Energy. The open points designate cross sections computed from electron-loss cross sections and ratios of electron-loss to electron-capture cross sections. The solid points represent the measured cross sections.

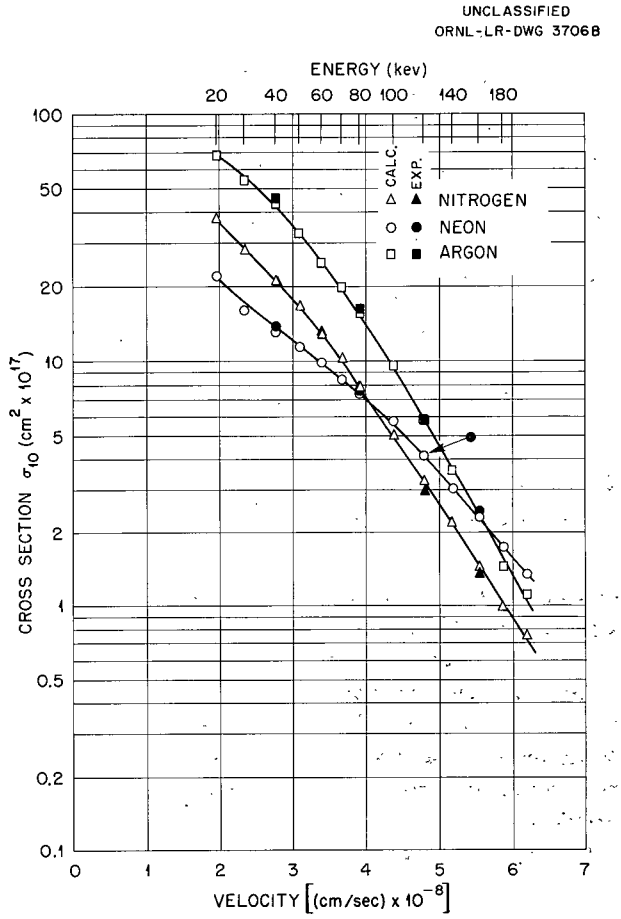

Fig. 5.13. Electron-Capture Cross Section for Protons in Nitrogen, Neon, and Argon as a Function of Velocity and Energy. The open points designate cross sections computed from electron-loss cross sections and ratios of electron-loss to electron-capture cross sections. The solid points represent the measured cross sections.

6. NEUTRINO RECOIL

6.1 RECOIL SPECTROMETRY

A. H. Snell F. Pleasonton

In this investigation the Cl^{37} ions which are produced in the electron-capture decay of A^{37} are subjected to high-resolution deflection spectrometry. It will be recalled that the only nuclear emission involved is an 816-kev neutrino, which leads to the expectation that the recoil atoms would have an energy of 9.66 ev. In the period covered by this report, significant improvements have been made in the quality of the results with respect to resolution of the different charge states, suppression of background, and energy calibration of the analyzing system.

The recoil spectrometer in its present form is illustrated in Fig. 6.1. The insulated conical source volume contains the A^{37} gas at a total pressure of about 10^{-5} mm Hg, and from its field-free interior a beam of the recoils emerges through an apical hole ½ in. in diameter. This beam is subjected to analysis by deflection through 96.5 deg in the two-directional-focusing magnet, followed by a second deflection by a two-directional-focusing 90-deg electrostatic deflector, after which the ions are accelerated for counting with an electron multiplier. It will be observed that for the A^{37} investigation the electrostatic deflector is not necessary so far as the energy analysis of the recoils is concerned; its main function at present is simply to provide another enlargement in the ion paths to which a large diffusion pump can be attached, thus aiding vitally in the suppression of the background that arises from the passage of the radioactive gas into the region of the detector. (For later work with continuous recoil spectra, the electrostatic deflector will team with the magnet to give e/m selection of the ions to be counted.) The differential-pumping situation can be traced out in Fig. 6.1.

The fluxmeter has been found to be the source of slightly nonreproducible results previously observed in the magnetic analysis of the recoils,

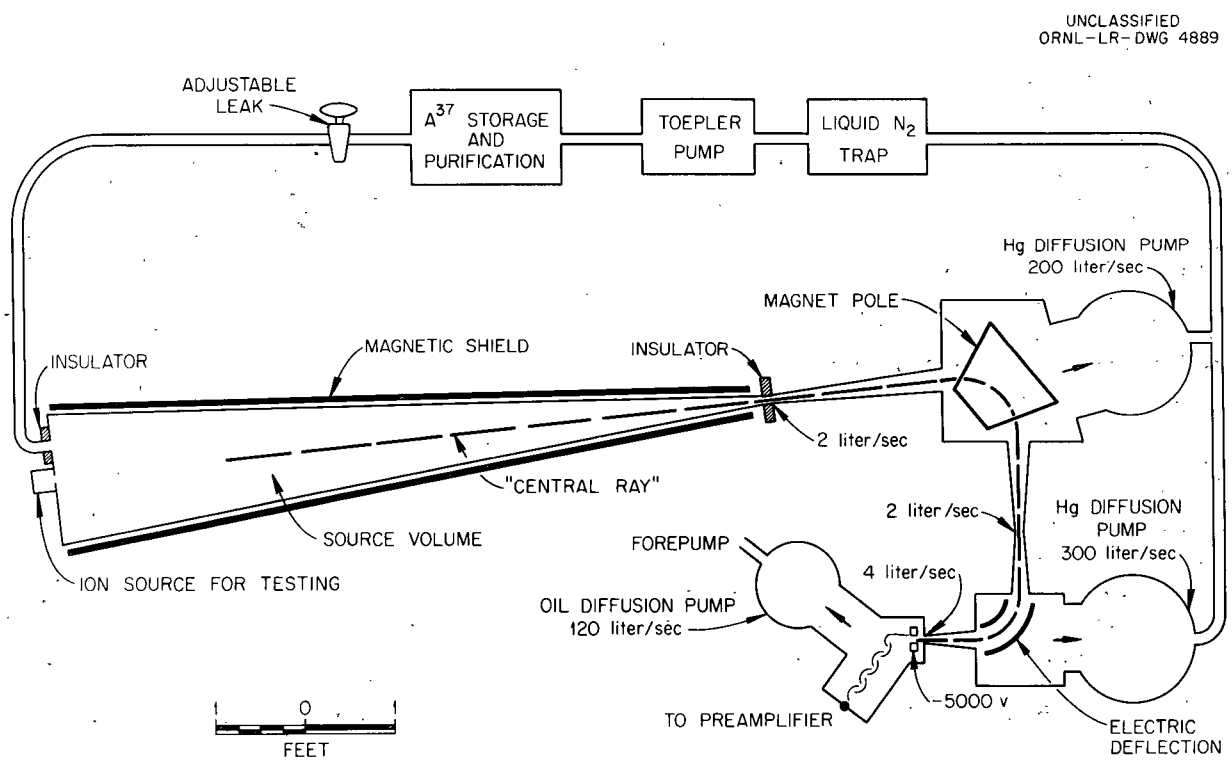

Fig. 6.1. Beta Recoil Spectrometer.

and a more accurate instrument will have to be obtained before a final result is given for the recoil-energy measurement. Meanwhile, the present instrument is calibrated before and after each A^{37} run; for these calibrations, ions of known energy originating in the test source on the large end of the source volume are used (Fig. 6.1).

The operating equations of the magnetic analyzer are

$$B\rho = \frac{[36.9762(E_r + zV_s)]^{1/2}}{143.94x}$$

and

$$F = \frac{5898z}{[36.9762(E_r + zV_s)]^{1/2}},$$

where E_r is the neutrino recoil energy in electron volts, V_s is the predeflection acceleration voltage applied to the source volume, z is the charge of the recoil ion in units of the electronic charge, and $B\rho$ is in gauss-centimeters. The value 36.9762 is taken to be the mass of the Cl^{37+++} ion. F is the fluxmeter reading, and the constant 5898 is derived from calibration with the ion source; it is this quantity that may vary over a range of nearly 1% from day to day because of small, erratic mechanical imperfections in the fluxmeter.

In taking measurements, the electrostatic deflector is matched to the magnet, so that it will pass whatever Cl^{37} ions are transmitted by the magnet. The magnetic- and electric-field strengths are then held constant, and the spectrum is swept over by changing the voltage on the source volume. This procedure substitutes one adjustment for three and is used as a timesaver; this is important because the source is steadily draining away. Monitoring is a nuisance because no A^{37} signal is observable outside the apparatus; this necessitates repeated reference back to a standard point in the spectrum in order to follow the decrease of the source strength with time.

The foregoing apparatus has been used to study the charge spectrum of the Cl^{37} recoil ions, the energy of the recoils, and the natural line shapes.

6.1.1 Charge Spectrum of the Recoiling Cl^{37} Atoms

With a potential of about 500 v applied to the source volume, the natural width of the lines becomes small compared with the transmission width of the analyzer, and under these circumstances it was sufficient in measuring the relative intensities to take counting-rate measurements at single settings upon the respective peaks. The peaks could, however, be traced over at will, as is shown in Figs. 6.2 and 6.3, where the rather weak charge-1 and charge-5 peaks are shown. These plots, of course, trace out only the transmission curve of the analyzer, but they are reproduced here to illustrate the complete resolution and the adequacy of the analyzer to transmit the full natural width of the lines. As will be observed from the scales at the top, the neutrino recoil energy was quite evident even when this rather high voltage was applied to the source volume.

It is unsafe to assume that the multiplier responds equally efficiently to the ions of varying charge, so for relative-intensity measurements it

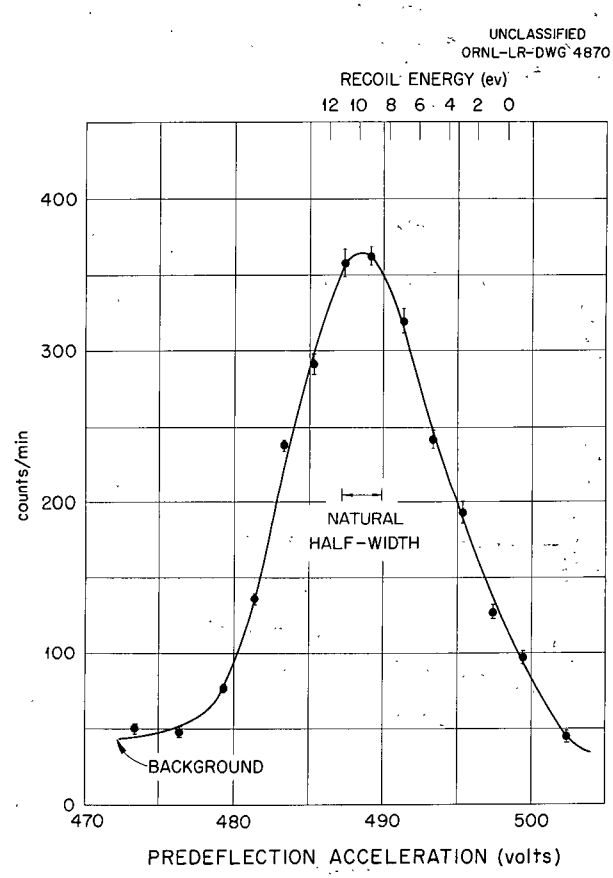

Fig. 6.2. A^{37} Decay; Charge-1 Cl^{37} Recoil Ions. Magnet setting, 19,531 $B\rho$.

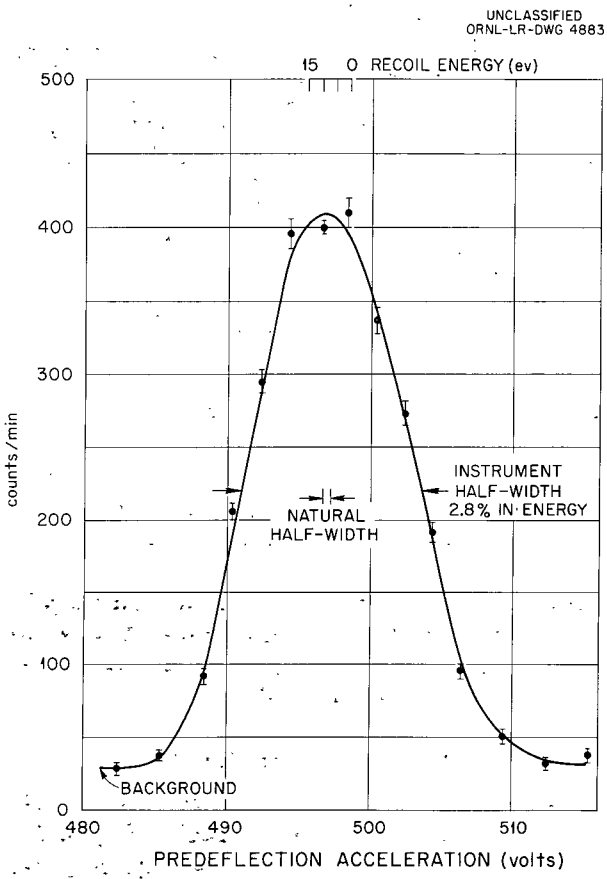

Fig. 6.3. A^{37} Decay; Charge-5 Cl^{37} Recoil Ions. Magnet setting, 8740 $B\rho$.

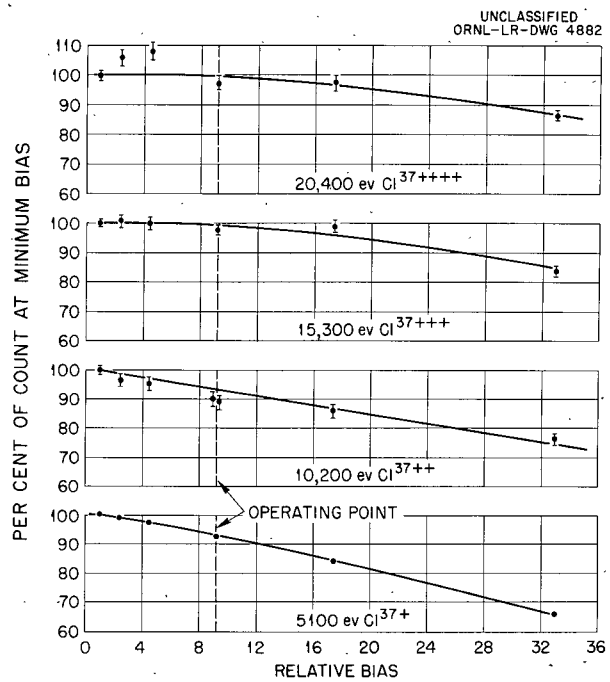

Fig. 6.4. Integral Bias Curves – Chlorine Ions.

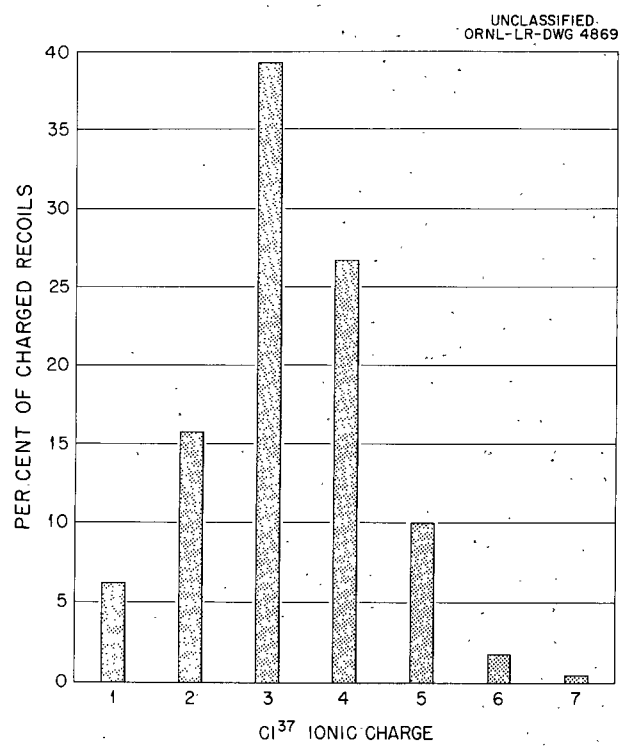

Fig. 6.5. Charge Spectrum of Cl^{37} Ions Made in A^{37} e-Capture.

was necessary to evaluate corrections by the use of conventional integral bias curves. The curve for singly charged ions was accurately obtained by introducing carbon tetrachloride vapor into the ion source, but for the higher charges the A^{37} peaks themselves had to be used. Consequently, the curves for the higher charges are rather rough (Fig. 6.4), but they do seem to indicate that ions of increasing charge produce pulses of slightly increasing average size. The upward corrections, read from these curves at the indicated operating point and applied to the observed counting rates, were 8.5% for charge-1 ions, 6.5% for charge 2, 3% for charge 3, and 1% for charge 4; no correction was assumed to be necessary for charges 5, 6, and 7.

The results of the relative-intensity measurements are displayed in Fig. 6.5 and given in detail in the second column of Table 6.1. The

TABLE 6.1. CHARGE SPECTRUM OF A^{37} RECOILS

Charge	Per Cent of Charged Recoils	
	Pressure 6–7 × 10^{-6} mm Hg	Pressure 12–16 × 10^{-6} mm Hg
1	6.2 ± 0.1	6.9 ± 0.1
2	15.7 ± 0.4	16.8 ± 0.4
3	39.2 ± 0.5	39.0 ± 0.5
4	26.7 ± 0.4	25.9 ± 0.4
5	10.0 ± 0.2	9.6 ± 0.2
6	1.8 ± 0.1	1.5 ± 0.1
7	0.4 ± 0.1	0.2 ± 0.1
Mean charge of charged recoils	3.26 ± 0.03	3.20 ± 0.03

errors indicated are a combination of statistical uncertainty and uncertainty in the multiplier sensitivity correction. These relative-intensity data were obtained by choosing the charge-3 line as a standard and making several alternating settings on charge 3 and on the line under investigation; the necessary allowance was made for source depletion and background. It is assumed that the ions of differing charge were equally efficiently transmitted through the apparatus.

Since the path lengths in the source volume were rather long, it was necessary to provide a magnetic shield (Fig. 6.1) to prevent the earth's field from preferentially affecting the paths of the recoils of high charge. It was also necessary to check the effect of pressure, lest collisions in the gas distort the charge spectrum. This was done by running a second set of measurements at about double the source-volume pressure used for the first set of readings. The source-volume pressures were, in fact, 6 to 7 × 10^{-6} mm Hg for the first run and 12 to 16 × 10^{-6} mm Hg for the second;[1] these are ionization-gage readings. The charge spectrum obtained at the higher pressure is given in the third column of Table 6.1. Comparison of the results shows that at the higher pressure the charge-1 and -2 peaks are strengthened, while the charge-4, -5, -6, and -7 peaks are weakened; there is thus an indication that the effect of collisions is to "degrade" the charge spectrum. However, the observed differences are quite small, and it is likely that the intensities obtained at the lower pressure are not far from what they would be if there were no collisions.

[1]These pressures include impurities; it must not, of course, be assumed that all this gas was pure A^{37}.

6.1.2 Energy of the Recoils

The energy of the recoil ions is most sensitively studied by using the charge-1 peak. Figure 6.6 shows this peak as obtained by adjusting the voltage of the source volume to give a natural line width approximately equal to the transmission width of the analyzer. Taking the center line of this peak and referring it to the recoil-energy scale at the top of the figure, it is clear that the recoil energy is very close to 9.6 ev. The main uncertainty in the determination remains in the calibration of the magnet and fluxmeter, that is, in the position of the upper scale relative to the operating scale at the bottom of the figure. The error here may be as large as 2% in the recoil energy. Within this limit of error it is apparent that the recoil momentum balances the momentum which would be carried off by a single neutrino having a kinetic energy of 816 kev.

Figure 6.7 shows a separate sensitive determination of the recoil energy.

6.1.3 Natural Line Widths

A computation performed by J. M. Jauch has indicated that the natural half-widths of the recoil lines should be about 2.4 ev, part of this originating in the thermal motion of the A^{37} atoms and part from the recoil given by the randomly

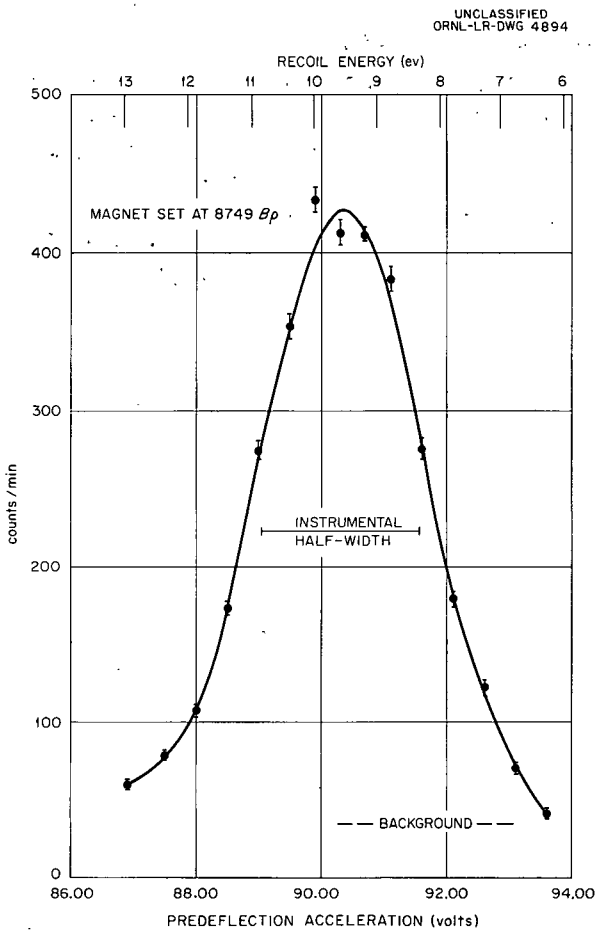

Fig. 6.6. A^{37} Decay; Charge-1 Cl^{37} Recoil Ions. Magnet setting, 8749 $B\rho$.

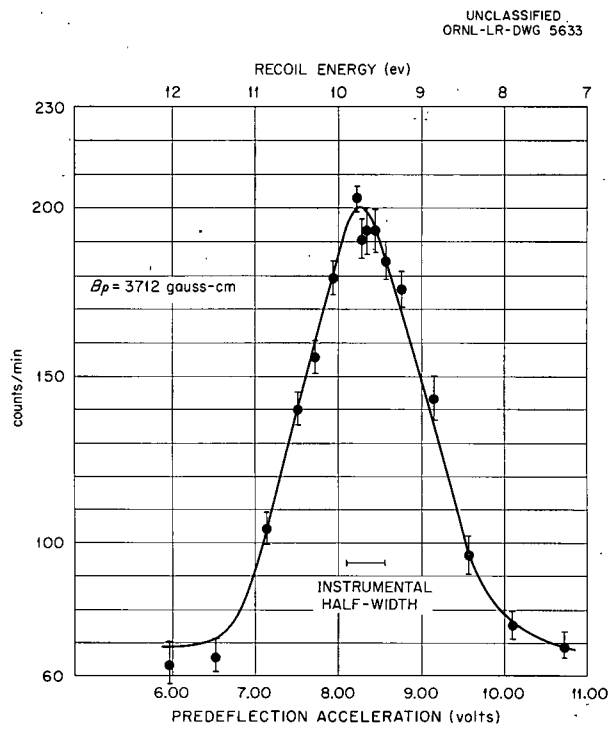

Fig. 6.7. A^{37} Decay; Charge-1 Cl^{37} Recoil Ions. Magnet setting, 3712 $B\rho$.

directed emission of the most energetic Auger electrons. It is possible to employ a little ruse to observe these effects separately. Consider, for example, the only processes that can give rise to singly charged recoils. They are:

1. K-capture followed by emission of an energetic Auger electron, leading to the creation of two L- or M-shell vacancies; these events to be followed by *no additional* Auger events in the L- and M-subshells;
2. K-capture followed by fluorescent K x-ray emission, leading to one L-shell vacancy, which would be followed by one Auger event in the L- or M-subshells;
3. L-capture, leading to one L-shell vacancy, to be followed by one Auger event in the L- or M-subshells.

The fluorescence yield for A^{37} has been measured[2] as 11%, and the L-captures have been found to occur in 8% of the decays.[3] Thus the first Auger event of process 1 will occur in 81% of the decays.[4] Despite this rather high probability, the prevalence of high charges in the recoil spectrum indicates a strong tendency for L-shell vacancies to be followed by Auger transitions in the L- and M-subshells, so that from the charge spectrum itself it seems very improbable that *two* L-shell vacancies would both be filled by purely radiative transitions. If this presumption is correct, then the total process 1 might occur much less frequently than processes 2 and 3, in which an Auger transition in the L- and M-subshells is actually called for. Processes 2 and 3 do not involve the emission of the most energetic Auger electrons, so the charge-1 line would have a width arising from thermal motion almost exclusively, and the line should be narrower than the lines containing recoils of higher charge.

[2] C. D. Broyles, D. A. Thomas, and S. K. Haynes, *Phys. Rev.* 89, 715 (1953).

[3] B. Pontecorvo, D. H. W. Kirkwood, and G. C. Hanna, *Phys. Rev.* 75, 982 (1949).

[4] Kofoed-Hansen's observations [*Phys. Rev.* 96, 1045 (1954)] would suggest 65% rather than 81%; if he is right, the argument above will be strengthened.

Figure 6.7 shows an examination of the charge-1 line, in which only 8 v was applied to the source volume. This gives a condition of high resolution, and the transmission width of the analyzer is small compared with the natural width of the line. It will be observed that, even including some width contributed by the analyzer, the half-width is only 1.8 ev. Jauch's estimate of the half-width arising from thermal motion alone was 1.6 ev.

It will be interesting to observe whether or not lines of higher charge are wider than the charge-1 line, but at the moment of writing the necessary measurements have not been made.

The authors are indebted to R. E. McHenry of the Operations Division for his extraction of the A^{37} from the CaO irradiated in the LITR.

7. NEUTRON CROSS SECTIONS AND FISSION PHYSICS

7.1 ABSORPTION CROSS SECTIONS FOR LONG-LIVED FISSION-PRODUCT Zr^{93}, Am^{241}, AND ENRICHED STABLE PLATINUM ISOTOPES

H. Pomerance

Absorption cross sections were measured for long-lived fission-product Zr^{93}, Am^{241}, and enriched stable platinum isotopes. The Zr^{93} was separated from old uranium slugs by G. W. Parker *et al.* of the Chemistry Division. A sample of 295 mg of the oxide gave a thermal-neutron absorption cross section of 0.63 ± 0.63 barn per average zirconium atom. The other atoms contribute more than half the absorption (Table 7.1), leaving a calculated value for Zr^{93} of 1.4 ± 3 barns. The best statement of the absorption cross section is that it is less than 4 barns.

TABLE 7.1. ISOTOPIC CONTRIBUTIONS TO THE ABSORPTION OF A ZIRCONIUM SAMPLE

Isotope	Abundance (%)	Absorption Cross Section (barns)	Sample Contribution (barn)
Zr^{90}	3.2	0.1	0.00
Zr^{91}	18.5	1.52	0.28
Zr^{92}	18.8	0.25	0.05
Zr^{93}	20.0	1.4	0.28
Zr^{94}	19.8	0.06	0.01
Zr^{96}	19.8	0.045	0.01
	100.0		0.63

The platinum isotopes were enriched and assayed by the Stable Isotopes Division. The four heavier isotopes – masses 194, 195, 196, and 198 – were about 60% abundant in their enriched materials; masses 190 and 192 were 0.76 and 7.62% abundant, respectively, in their enriched materials. The samples were in metallic form and were quite pure according to the semi-quantitative analyses. The reactor oscillator measurements give a larger atomic-cross-section value for the Pt^{195} than the value measured several years ago for natural platinum. Reanalysis of the sample at X-10 verifies only that the sample is chemically purer than any available commercial platinum. The values given in Table 7.2 can be compared with a recent value for Pt^{196}, determined by W. S. Lyon of the Analytical Chemistry Division, of 0.72 ± 0.1 barn and with quoted values[1] of 90 ± 40 barns for Pt^{192} and 3.9 ± 0.8 barns for Pt^{198}.

The Chemical Technology Division prepared some chemically pure Am^{241} from reactor-irradiated material. An aluminum foil with 19 mg of the americium was measured in the reactor oscillator. The thermal-neutron absorption cross section of 625 ± 35 barns is based on the value of 98 barns for gold. Other samples of americium which were

[1]Neutron Cross Section Advisory Group, *Neutron Cross Sections*, AECU-2040 (May 15, 1952).

TABLE 7.2. THERMAL-NEUTRON ABSORPTION CROSS SECTIONS FOR PLATINUM ISOTOPES

Experimental				Computed Isotopic Cross Section (barns)
Isotope Mass	Sample Code	Weight (mg)	Equivalent Gold (mg)	
190	776a	151	15.3	90 +200, −90
192	777b	703	55.8	8 ± 8
194	778a	4988	437.2	1.2 ± 0.9
195	779a	751	1278	26.8 ± 1.3
196	780a	5980	467.8	0.7 ± 0.7
198	781b	986	55.8	4.0 ± 0.5

analyzed chemically showed rare-earth impurities, but none large enough to change the americium value by as much as the quoted error.

7.2 FISSION NEUTRON SPECTRUM OF U^{233}

K. M. Henry M. P. Haydon

The possible use of U^{233} as a reactor fuel creates interest in the U^{233} fission neutron spectrum. The proton-recoil neutron spectrometer[2] developed at the Bulk Shielding Facility has been used to ascertain this spectrum between 1.3 and 10 Mev.

Radiation from the Bulk Shielding Reactor filtered through 5 in. of lead and 3 ft of carbon served as a thermal-neutron source (thermal column). The source for the fission neutron spectrum was constructed by R. E. Greene, K-25 Plant, and consisted of 1.62 g of U^{233} plated on ten 3-in.-dia aluminum disks. This source was placed against the thermal column. The neutron spectrometer looked at neutrons from the source through a short (10-in.) collimator. The experimental arrangement is shown in Fig. 7.1. The spectrum obtained (with background subtracted) is shown in Fig. 7.2. The background, which consisted of reactor fast-neutron flux scattered through the thermal column, was measured by removing the source plate. It also is plotted in Fig. 7.2.

The spectral measurement was partially repeated with the use of 1.43 g of U^{235}. This source provided a normalization to the previously known U^{235} fission spectrum,[3] which is shown as a dashed line in Fig. 7.2. The two spectral curves in Fig. 7.2 were normalized to equal masses of fissionable material.

The points of the U^{233} and U^{235} fission neutron spectra agree within statistical error. The resulting spectral curves indicate that the U^{235} spectrum is slightly higher at the lower energies. The uncertainty of the neutron-abundance curves varies from 10% at the lower energies to 200% at the highest energy. Now that more U^{233} is available, it is planned to rerun the spectrum with a larger sample of U^{233} in order to improve the information-to-background ratio.

[2]R. G. Cochran and K. M. Henry, *A Proton Recoil Fast Neutron Spectrometer*, ORNL-1479 (April 2, 1953).

[3]R. G. Cochran *et al.*, *Reactor Radiations Through Slabs of Graphite*, ORNL CF-54-7-105.

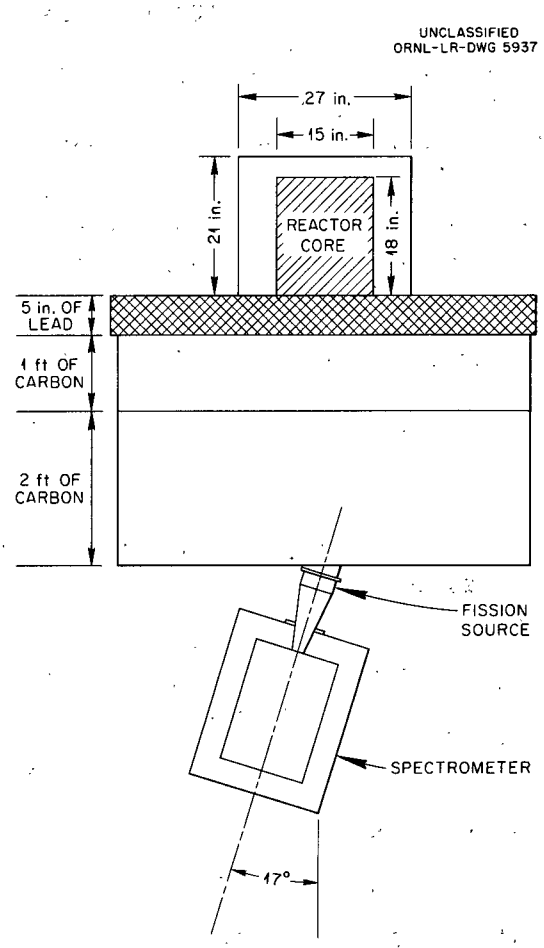

Fig. 7.1. Experimental Arrangement for BSF Measurement of the Fission Neutron Spectrum of U^{233} (Top View).

Nuclear plates were exposed to both the U^{233} fission source and the thermal column background. Results of this study should be available in about nine months.

7.3 ENERGY SPECTRUM OF GAMMA RAYS ACCOMPANYING THE FISSION OF U^{235}

F. C. Maienschein R. W. Peelle
R. G. Cochran K. M. Henry
G. M. Estabrook T. A. Love

To design an effective reactor shield on the most reasonable basis, it is necessary to have spectral information concerning the various sources of radiation involved. The spectrum of photons given off at the time of the fission process has, until recently, been virtually unknown

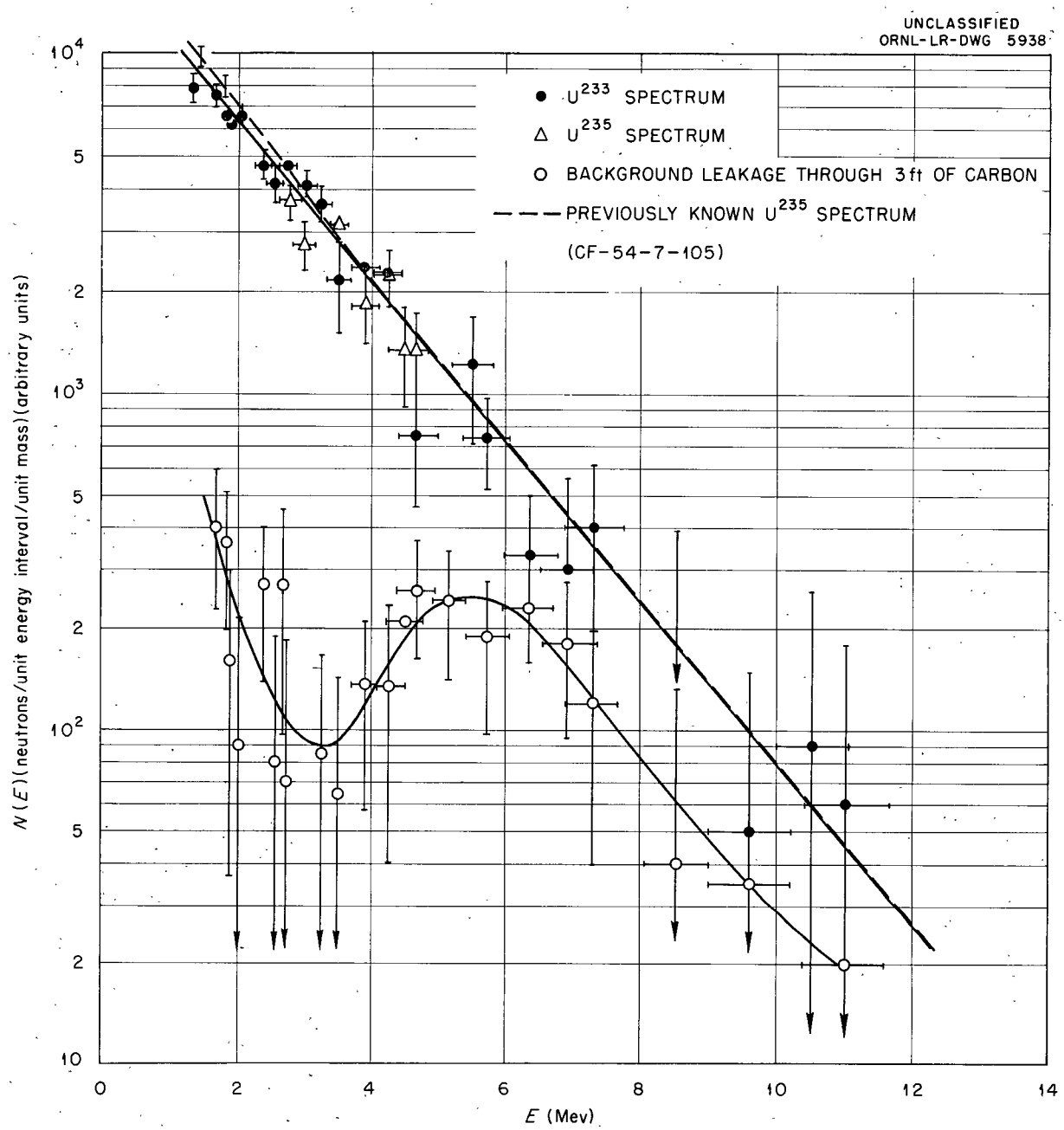

Fig. 7.2. Fission Neutron Spectra of U^{233} and U^{235}.

(see Sec. 2.4). Although it is commonly assumed that the major fraction of the photons arise from the decay of primary fission fragments, a knowledge of the prompt fission photon spectrum might have some bearing upon the theory of the fission process. A continuing program is being conducted at the Bulk Shielding Facility for the measurement of the prompt fission gamma-ray spectrum. In this experiment, all photons are considered as prompt if they occur within the resolving time of the coincidence circuit. Thus far, preliminary results of the experiment have been obtained for the

energy interval between 0.5 and 2.3 Mev.

The mechanical layout of the experimental equipment is shown in Fig. 7.3. The lead shield, which encases the spectrometer, rests on the BSF thermal column. A stream of thermal neutrons flows from the thermal column through a bismuth gamma-ray shield toward a spiral-wound fission chamber containing $U^{235}O_3$ deposited on aluminum. The fission chamber is placed within a removable annular cylinder chosen to make the experimental backgrounds as low as possible. In the experiments reported here, cylinders composed of bismuth and of lithiated paraffin were employed. Gamma rays that originate at the fission chamber may pass through a collimator to a multiple-crystal gamma-ray coincidence spectrometer within a lead shield. For the collection of the data presented here, only the two lower sodium iodide crystals were used in coincidence with the fission chamber. This two-crystal arrangement comprises a Compton scintillation spectrometer.

Figure 7.4 shows a block diagram of the electronic equipment. The arrangement is designed to allow the analysis of that pulse-height spectrum in the center crystal which is in coincidence with

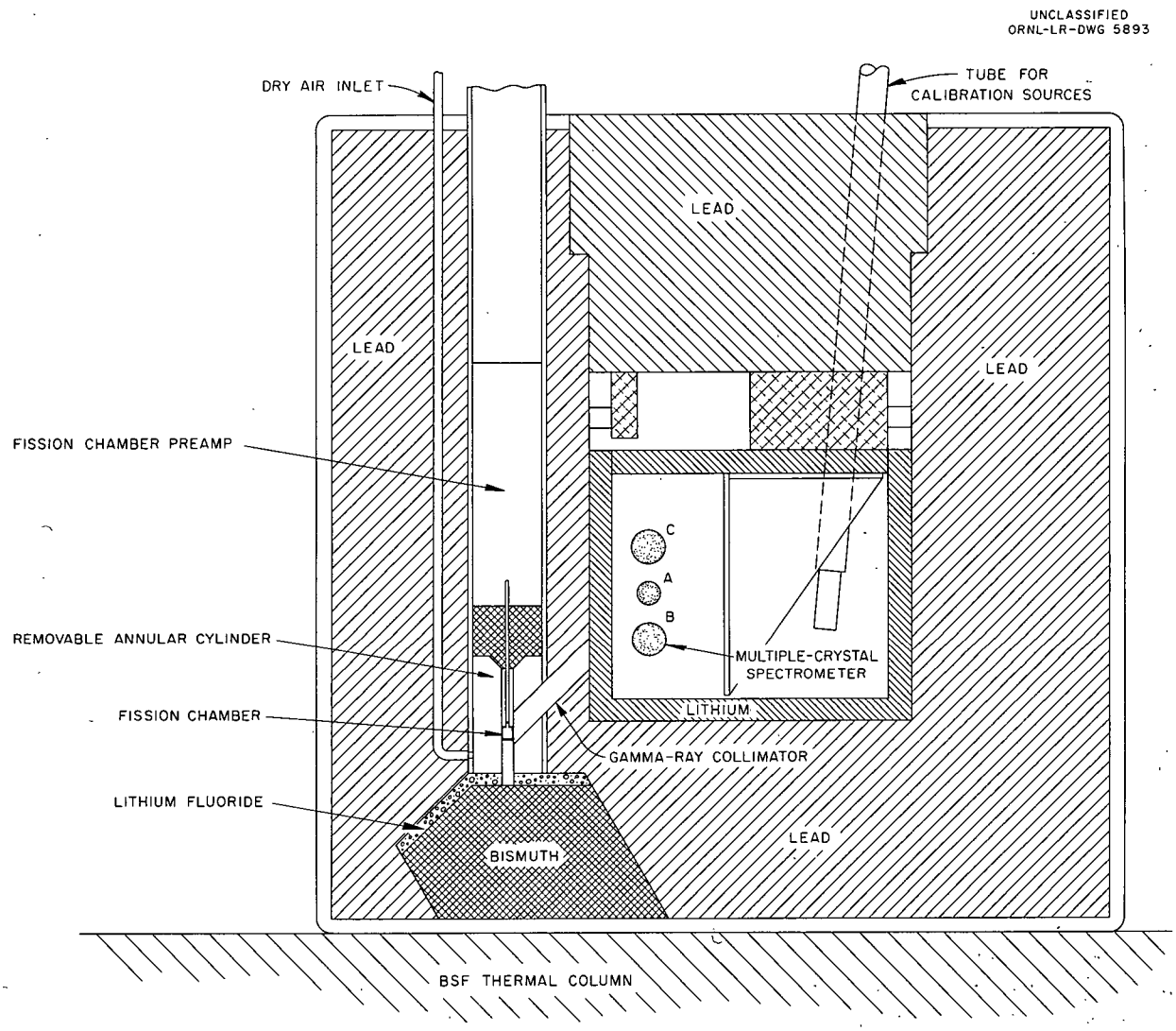

Fig. 7.3. Fission Gamma-Ray Spectrometer.

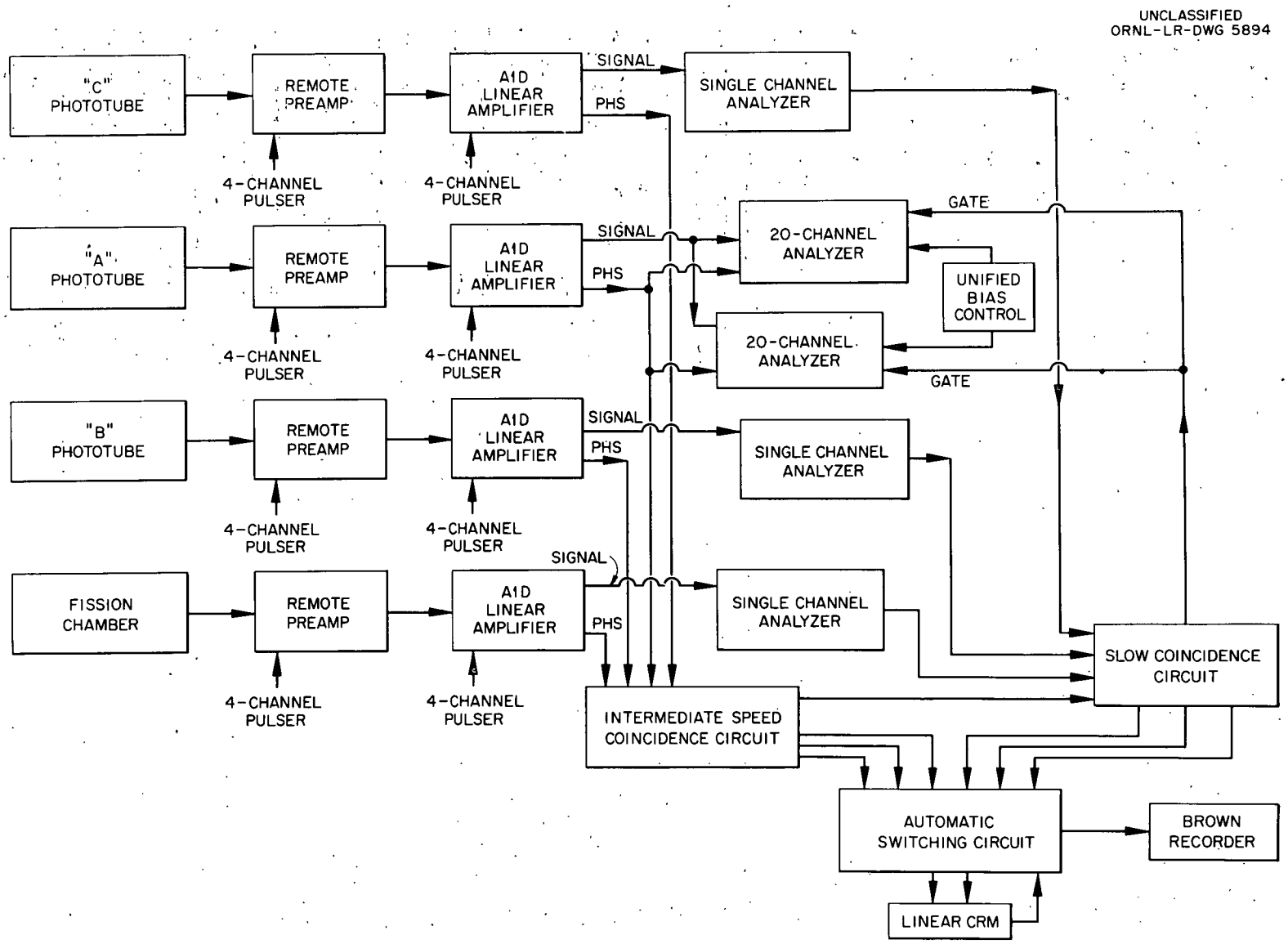

Fig. 7.4. Block Diagram of Fission Gamma-Ray Spectrometer Electronics.

Compton-scattered gamma rays in the lower crystal.[4]

In the past, experimental difficulties have been caused by the presence of a background spectrum originating largely in chance coincidences between the three channels involved – two scintillation counters and one fission chamber. Meaningful results for this experiment were made possible by improvements in the shield design, which lowered the level of the gamma-ray flux in the region of the scintillation crystals. The most important of these improvements include lining the interior of the lead shield with a metallic lithium box and placing crystalline lithium fluoride[5] upon the top and forward side of the bismuth gamma-ray suppressor.

For any given reactor power, an apparent energy spectrum with 40 energy channels was obtained. This spectrum, which contained both true and random counts, was derived from the experimental pulse-height distribution as described below.

The response of the Compton spectrometer is not entirely unique,[6] and the final analysis must include a correction for the low pulse-height "tail" which accompanies the main peak. This correction was not made in the present analysis. The energy of the photon corresponding to a given Compton-scattered electron energy was obtained by assuming 135-deg scattering of the gamma rays. The number of apparent photons/(fission·Mev) was determined from the experimental data by using the published[5] relative-efficiency curve. The absolute solid-angle and efficiency factors were determined by the use of Nb^{95} and Na^{22} sources for which the disintegration rates were obtained by using the calibrated high-pressure ionization chamber of the Analytical Chemistry Division. The three gamma rays from the above sources gave consistent results for the absolute efficiency of the spectrometer.

With the method outlined above, the apparent number of photons/(fission·Mev) as a function of energy could be obtained for any desired thermal flux at the fission chamber. The determination of the contribution from random coincidences for this experiment is sufficiently complicated to deserve some explanation.

The random-coincidence background could be readily determined if it were really caused by random triple coincidences, since a registered coincidence requires the instantaneous confluence of three rectangular pulses of known length. This triple-coincidence rate is negligible, compared with random coincidences between a count in any one detector and a true coincidence in the other two detectors. Therefore, in order to calculate the random-background spectrum with the use of measured resolving times, a series of double-coincidence spectra must first be measured, and then a series of subtractions for each energy channel must be made. Another common method for the evaluation of random backgrounds involves direct measurements by the insertion of delay lines in one or more of the signal channels. Here the process of successive subtraction becomes even more treacherous, because of the effects of the delay cable upon the pulse shapes.

The method of analysis actually used on the present data depends upon the behavior of the background as the counting rates in each detector are increased by raising the reactor power. The true number of photons per fission will surely not depend on reactor power, but the important random backgrounds per fission will increase linearly with the counting rates in the detectors. Thus, if the apparent number of photons/(fission·Mev) is plotted as a function of reactor power, the extrapolated value at zero power will yield a point on the true spectrum.

Therefore, to determine a true spectrum from a set of three or four apparent spectra obtained with differing reactor powers, a least-squares fit to a straight line for the plot of photons/(fission·Mev) vs reactor power was obtained for each channel. The fitted value of the zero-power intercept, the statistical error of the intercept induced by the experimental data, and the degree of goodness of fit constitute the output data from this analysis. Figure 7.5 shows the results of two independent spectral determinations. The errors shown are those derived from experimental statistical errors through the least-squares analysis. The results of the test for degree of goodness of fit, when applied to the data as a whole, imply that the errors in the extrapolation are statistical in nature.

[4] F. C. Maienschein, *Multiple-Crystal Gamma-Ray Spectrometer*, ORNL-1142 (July 3, 1952).

[5] F. Kertesz, private communication.

[6] F. C. Maienschein, R. W. Peelle, and T. A. Love, *Phys. Semiann. Prog. Rep. Sept. 10, 1954*, ORNL-1798, p 34–36.

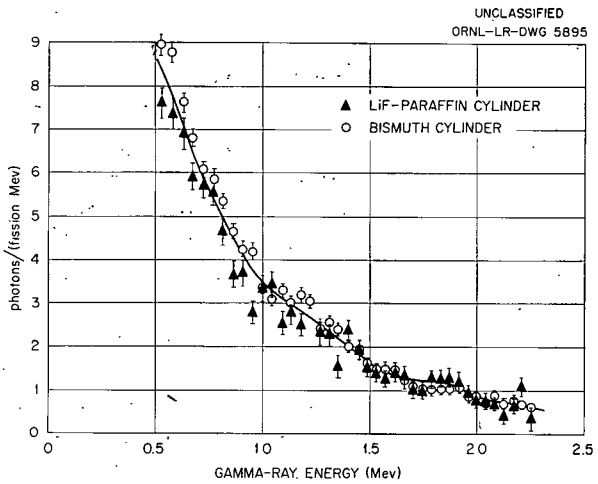

Fig. 7.5. Gamma-Ray Energy Spectrum (0.5 to 2.3 Mev) Accompanying the Fission of U^{235}.

If the combined data from the runs with lithiated paraffin and bismuth are considered, the number of photons per fission for the energy region covered by this work can be determined by integration. This results in 5.0 photons/fission for a total energy of 5.1 Mev/fission from the measured spectrum between 0.5 and 2.3 Mev. It is interesting to note that the spectral data do not differ markedly from those in Sec. 2.4 for the part of the spectrum that has been measured.

8. REACTOR PHYSICS AND SHIELDING

8.1 ATTENUATION OF SWIMMING POOL REACTOR RADIATIONS

F. C. Maienschein
G. M. Estabrook E. B. Johnson
J. D. Flynn K. M. Henry

A swimming pool reactor depends upon water in the reactor pool to act as the radiation shield. Other reactors utilizing the same type of core use water as the initial portion of the shield. Therefore part of the basic design data needed for such reactors is the attenuation of the reactor radiations in water. Measurements of the attenuation of the gamma-ray dose rate and the thermal-neutron flux from the Bulk Shielding Reactor have now been made through greater thicknesses of water than would be required for any practical shield. Only the direct penetration of radiation is reported here; no mention is made of the possibility of activities being transported through the water.

8.1.1 Reactor Description

The swimming pool reactor used in these measurements was the ORNL Bulk Shielding Reactor (BSR). The reactor loading consisted of 28 MTR-type fuel elements containing a total of 3.6 kg of U^{235}. The BSR, which can be operated at powers up to 1 Mw, is suspended in a pool of water 40 ft long by 20 ft wide by 20 ft deep.[1] The water of the pool acts as the moderator, the reflector, and the coolant, as well as the radiation shield. Flow through the reactor at all power levels is by thermal convection.

All radiation levels presented in this report are expressed in terms of reactor power. This power was determined by the usual method of mapping the thermal-neutron flux throughout the reactor. From the integrated thermal-neutron flux the fission rate was determined. The power was then derived from the known energy release per fission for this reactor.[2] The reactor power utilized varied between 0.1 and 10^6 w.

8.1.2 Radiation Detectors

Gamma-ray dose-rate measurements were made with a set of ion chambers utilizing the Bragg-Gray principle. These chambers were designed by J. L. Meem and calibrated by L. H. Ballweg.[3] For such chambers the gamma-ray dose is proportional to the voltage produced by the ionization current flowing through a precision resistor. An electrometer[4] determines the null condition for which this voltage is just balanced by a known bucking voltage. The conversion from voltage to dose was taken from the report by Ballweg and Meem.[3] A check of the absolute calibration for one of the chambers was made with a radium source previously calibrated by the National Bureau of Standards, and, for favorable geometries, agreement to within 3% was obtained. The center of detection calculated by Hungerford was used.[5] The measurements were made with three ion chambers of different sensitivities in order to cover a large dose range. The sizes of the instruments were: 50-cc volume, 10^{12}-ohm resistor; 50-cc volume, resistor variable from 10^6 to 10^{10} ohms; and 900-cc volume, 10^{12}-ohm resistor.

For thermal-neutron flux measurements, three different detectors were utilized. Close to the reactor a 3-in.-dia single-plate U^{235} fission chamber was used; this instrument has little gamma-ray background response, and the center of detection is well known. At greater distances, where more sensitivity was required, the measurements were made with a large BF_3 proportional counter (12 in. long and 2 in. in diameter). The center of detection was again taken from Hungerford.[5] For both the chamber and the counter a conventional amplifier and scaler were used.

Absolute calibration of the thermal-neutron flux was provided by exposure of indium foils with and without cadmium covers. The difference of such readings is proportional to the thermal-neutron flux. The foil calibrations were made in the ORNL Standard Pile, with due correction being

[1] W. M. Breazeale, *Nucleonics* 10, No. 11, 56 (1952).
[2] J. L. Meem, *Nucleonics* 12, No. 5, 62 (1954).
[3] L. H. Ballweg and J. L. Meem, *A Standard Gamma Ray Ionization Chamber for Shielding Measurements*, ORNL-1028 (July 9, 1951).
[4] F. M. Glass, *A Simple Low Drift Electrometer*, ORNL-486 (Dec. 30, 1949).
[5] H. E. Hungerford, *Center of Detection Calculations for Neutron Counters and Ion Chambers*, ORNL CF-51-5-177.

made for the change from a water to a graphite medium.[6]

8.1.3 Measurements

For the gamma-ray attenuations, a new set of fuel elements was available, so that the fission-product gamma-ray activity was nil. As the distance between reactor and ion chamber was increased, the reactor power was raised. At all points a check was made for residual gamma activity by a background reading with the reactor at zero power.

The gamma-ray activity induced in the water was greatly reduced by the recent introduction of demineralized water into the BSF reactor pool. Previously, the process water, which was treated with sodium chromate, gave rise to appreciable induced activities. With the pure demineralized water, it became necessary to measure the background due to induced activities only at very large distances (greater than 500 cm). This background was measured with a 5-in.-thick, 4-ton lead slab between the reactor and detector. Any dose measured with the slab in place was due to activity in the water, since penetration through the lead by gamma radiation was less than 0.3%. Rotation of the lead slab showed that no appreciable radiation scattered around the slab, since the dose was essentially independent of the angle of rotation (up to 75 deg). An attempt to establish an optimum position for the lead between the detector and reactor revealed little apparent variation in dose with position, so the slab was finally placed about halfway between the detector and reactor. The water activity backgrounds were less than 25% until the very last point, which had a 60% background, was measured.

The effects of the structure around the reactor were small because of the large size of the BSF reactor pool. The closest concrete was in the pool floor, 8 ft away from the reactor for most of the measurements and about 5 ft for the greatest separations. The pool walls, also of concrete, were 10 ft distant, while the surface of the pool water was 16 ft above the reactor.

Overlapping gamma-ray measurements were made with the three ion chambers, as indicated by the different points in Fig. 8.1. Measurements with the other chambers were normalized to those for the 50-cc volume, 10^{12}-ohm resistor chamber, which was regarded as the standard instrument after calibration by the radium source.

Thermal-neutron flux measurements were made in the same manner as were the gamma-ray dose-rate measurements, except that no background measurements were necessary. At all points the

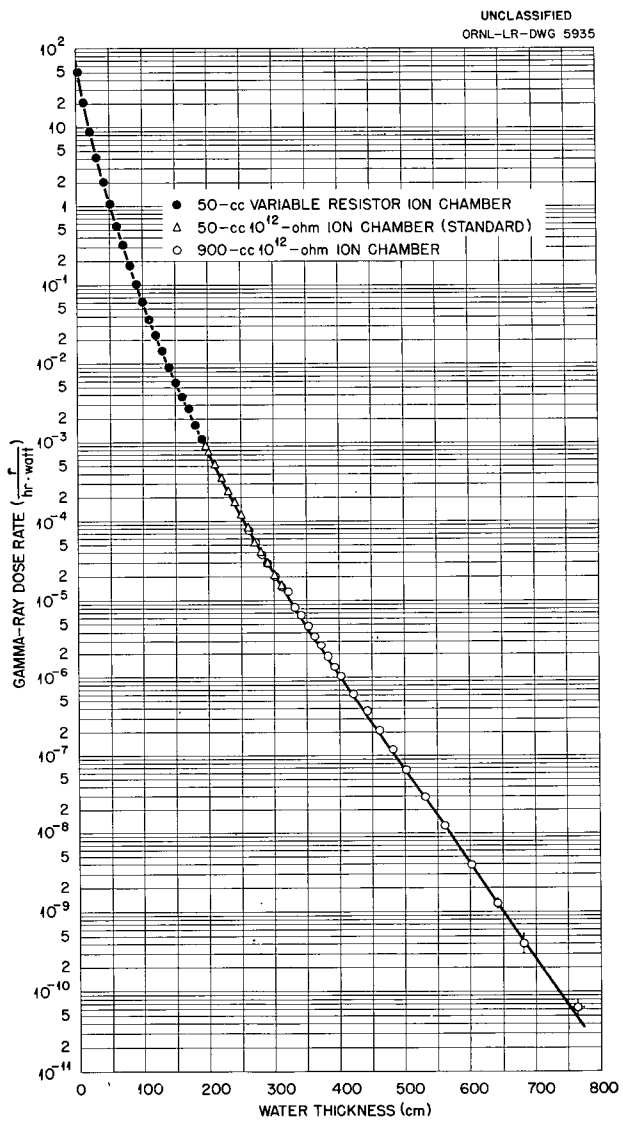

Fig. 8.1. Gamma-Ray Dose Rate as a Function of Distance from the Bulk Shielding Reactor.

[6] E. D. Klema and R. Ritchie, *Preliminary Results on the Determination of Thermal Neutron Flux in Water*, AECD-3174 (April 24, 1951); *also see* E. D. Klema, R. H. Ritchie, and G. McCammon, *Recalibration of the X-10 Standard Graphite Pile*, ORNL-1398 (Oct. 17, 1952) (declassified Aug. 6, 1953).

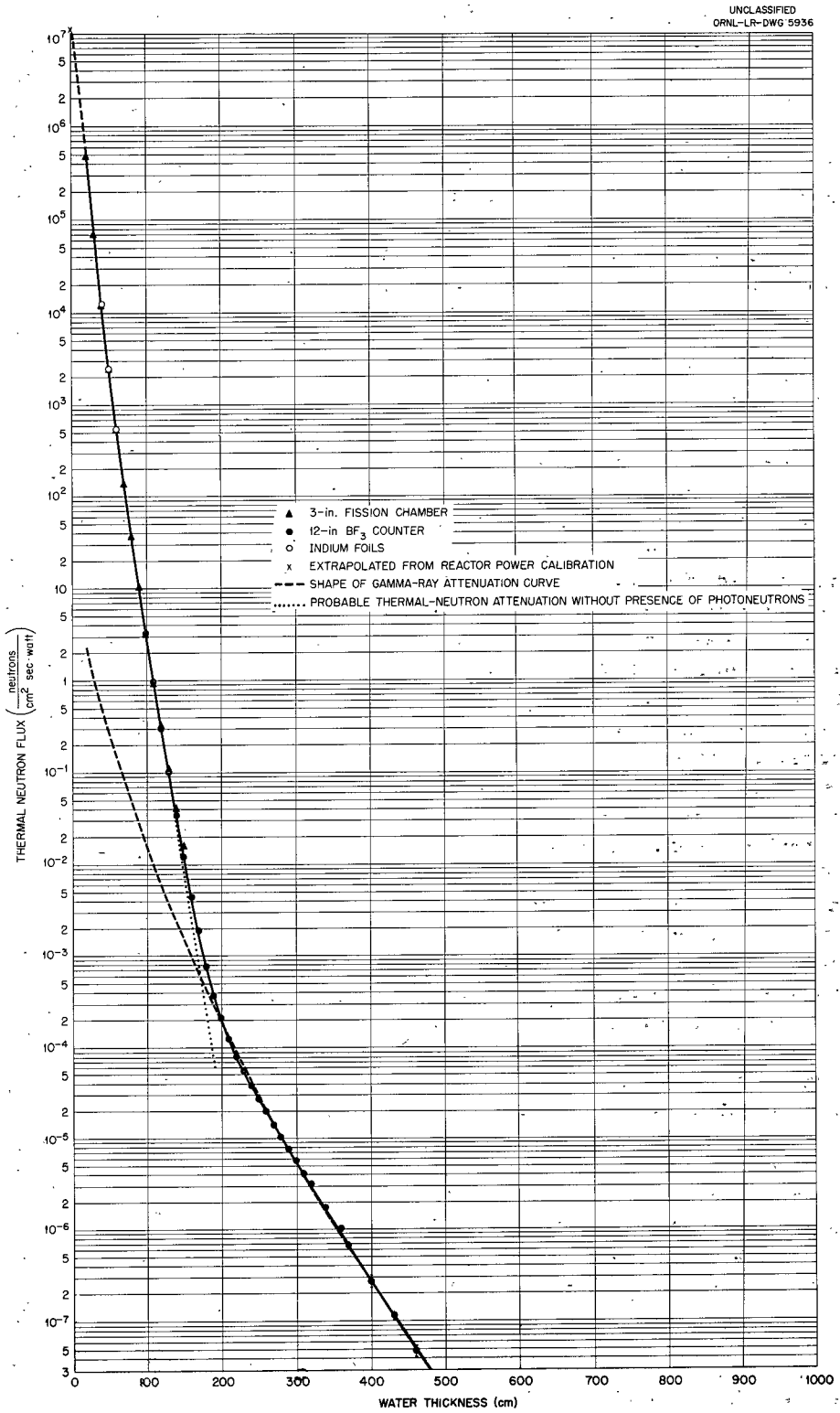

Fig. 8.2. Thermal-Neutron Flux as a Function of Distance from the Bulk Shielding Reactor.

reactor power was adjusted so that no excessive gamma-ray fields were allowed to perturb the BF_3 proportional counter. The thermal-neutron flux data obtained were normalized to the indium-foil measurements taken at the positions indicated in Fig. 8.2. The point at the reactor face (no water thickness) was extrapolated from the thermal-neutron flux in the reactor core as determined in the power calibrations. The error in the flux for this one point might be as large as 10%.

For the points of greatest attenuation, an additional uncertainty was introduced in the reactor-power determination. At a 1-Mw reactor power, possible deviations of 10 to 15% from the nominal reactor power give rise to the large errors shown in Figs. 8.1 and 8.2 at the largest attenuations.

8.1.4 Results

The curves obtained in Figs. 8.1 and 8.2 may be used to determine the leakage flux at the reactor face. Thus at 1 Mw the gamma-ray dose rate at the surface of the reactor is seen to be about 8×10^7 r/hr, while the thermal-neutron flux is about 1.1×10^{13} neutrons/(cm^2·sec).

The two curves are plotted on the same scale, even though the more penetrating gamma radiation extends to greater distances, so that the similarity between the curves beyond 200 cm may be observed. In Fig. 8.2 the dashed curve has the same shape as the gamma-ray dose-rate attenuation curve from Fig. 8.1. The similarity in slopes arises because essentially all neutrons beyond 200 cm are photoneutrons produced by the gamma rays in the deuterium naturally occurring in the pool water. This explanation was first put forward by E. P. Blizard. The difference curve, shown as a dotted line in Fig. 8.2, should correspond to the actual thermal-neutron attenuation. This attenuation is exponential with a relaxation length (reduction to $1/e$) which varies between 6 and 9 cm over a reduction of 10^{10}.

8.2 CALIBRATION OF CONTROL RODS IN THE BULK SHIELDING REACTOR

E. B. Johnson K. M. Henry
F. C. Maienschein

The most practical method available for measuring the change in reactivity of a reactor is by means of calibrated control rods. Since a quantitative knowledge of the reactivity changes was necessary for the beam-hole experiments described in Sec. 8.3, rod calibrations were made for the pertinent reactor configurations. Further studies were made of the effectiveness of these rods in other reactor loadings.

8.2.1 Reactor Loadings

The control rods of the BSR have been calibrated in three reactor loadings: loadings 22A, 32, and 33. The regulating rod has also been calibrated in loading 38. Loading 22A was a completely water-reflected assembly, arranged in a 5 × 6 array. The control rods used for this loading consisted of two cadmium-lead safety rods, each worth about 1.3% $\Delta k/k$, and a cadmium-lead regulating rod worth about 0.6% $\Delta k/k$ over the last 12 in. of travel. This lattice configuration and the calibration of these rods in this critical assembly have been discussed in detail in an earlier report.[7]

Loading 32 was an arrangement of 20 fuel elements reflected on the four vertical sides by 3 in. of beryllium oxide as shown in Fig. 8.3. The control rods used for this configuration consisted of two safety rods containing B_4C

[7] R. G. Cochran *et al.*, *Reactivity Measurements with the Bulk Shielding Reactor*, ORNL-1682 (Nov. 9, 1954).

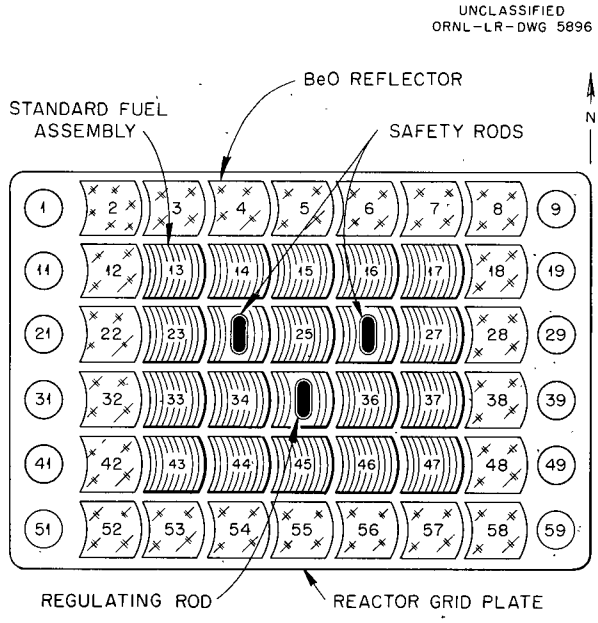

Fig. 8.3. Bulk Shielding Reactor Loading 32.

powder as the neutron-absorbing material and a water-filled, hollow, type 347 stainless steel regulating rod with an 0.087-in. wall. The calibration of these rods is described below.

Loading 33 (Fig. 8.4) was essentially a 5 × 6 completely water-reflected arrangement with two elements missing at the corners of the back (south) face. The two B_4C safety rods and the stainless steel regulating rod were also used in this configuration.

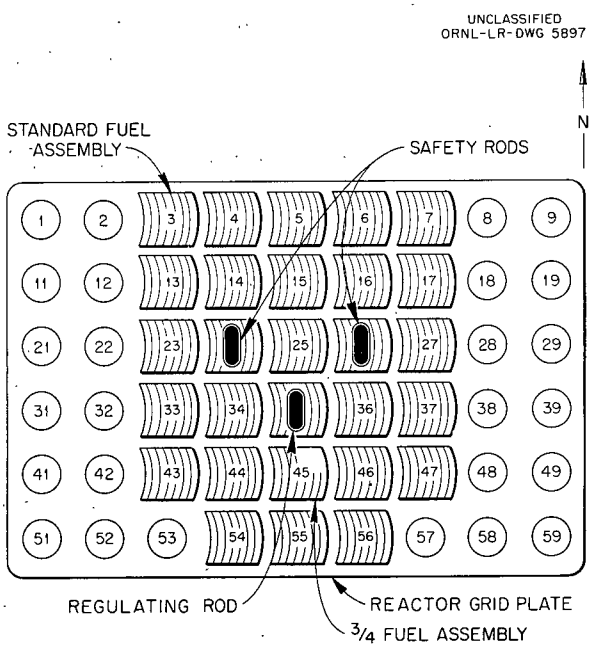

Fig. 8.4. Bulk Shielding Reactor Loading 33.

Loading 38 (Fig. 8.5) was reflected along the north face by 3 in. of beryllium oxide but was water-reflected on the other five sides.

8.2.2 Distributed-Poison Calibration Method

Since the effect of photoneutrons from beryllium make rod calibrations by the usual inhour formula questionable in a beryllium-reflected loading and since it was further necessary to keep the fuel elements "cold" until other experiments had been performed, the regulating rod in loading 32 was calibrated by means of distributed gold poisoning. Gold in the form of foils was attached to Lucite strips, which were then inserted in the fuel elements of the reactor lattice in such a pattern that the poisoning was approximately uniform.

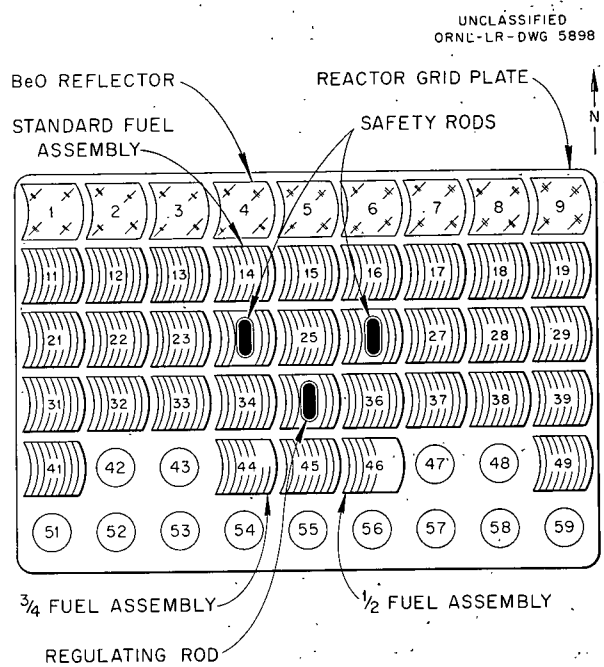

Fig. 8.5. Bulk Shielding Reactor Loading 38.

The reactor was brought to a low, stable power level, and the position of the regulating rod was measured both with and without the poison, the safety-rod positions remaining unchanged. Six different amounts of poison were used, all with the safety rods at the same positions. The position of the regulating rod, with no gold or Lucite in the lattice, corresponding to these safety-rod settings was 18.5 cm. Finally, all the gold was removed from the Lucite strips, and they were inserted in the same positions that they had occupied when loaded with gold. With the safety rods at the same positions as previously, the regulating rod was inserted only 1.5 cm farther because of the presence of the Lucite instead of water. A selsyn is used with each control rod to indicate on a dial the position of that rod relative to its fully inserted position for reactor-control purposes. However, for a more accurate method of determining rod positions, pointers were installed on the tops of the rods of the lift magnets, and the rod positions were measured directly. By this method, the safety rods could be restored to a previous position with an uncertainty of ±0.05 cm. Uncertainties in the regulating-rod positions were ±0.5 cm.

The reactor cross section was computed as

5900 cm^2 by considering only the active portion of the lattice. The change of reactivity resulting from the insertion of a known amount of gold could then be calculated from $\Delta\Sigma/\Sigma$ by using a thermal-neutron absorption cross section for gold of 98 barns.[8] Since the presence of the gold should cause no appreciable change in the Fermi age, $\Delta\Sigma/\Sigma$ should be the same as $\Delta k/k$. The calibration curve for the regulating rod was then plotted as an integral curve showing the change in reactivity from the initial rod position of 17 cm (Fig. 8.6). It was necessary to extrapolate the upper portion of the curve above the measured points by assuming symmetry around the point at which the rod is half withdrawn from the lattice. This procedure indicated a total worth of regulating rod of approximately 1.2% $\Delta k/k$, which was much higher than was expected, even in a beryllium-reflected loading, on the basis of the inhour calibration of the TSF rod.[7]

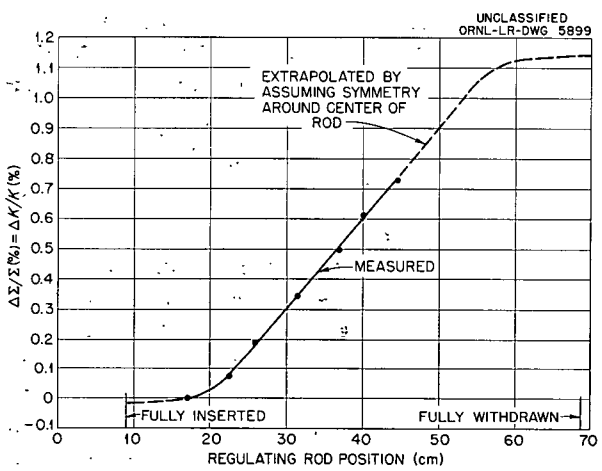

Fig. 8.6. Integral Curve for Stainless Steel Regulating Rod in Loading 32 (Beryllium Oxide Reflected) – Distributed-Poison Calibration Method.

Each of the safety rods in loading 32 was calibrated against the regulating rod. The reactor was brought to a stable power level of something less than 1 w, was put on servo control, and the positions of all three rods were noted. Then the position of one of the safety rods was changed a known amount, the other safety rod remaining fixed, and the new position of the regulating rod necessary to maintain constant power was noted. This procedure was repeated until the entire available length of each rod had been covered. Since there was insufficient excess reactivity in the loading to permit the reactor to remain critical with only one safety rod and with the regulating rod fully withdrawn, the calibration curves for both safety rods were extrapolated from about the 37-cm position to the fully inserted position by assuming symmetry around the mid-point of the rod. The calibration curves for these rods were also plotted as integral curves for the effect of insertion of the rod from the fully withdrawn position. Extrapolation of the curves to the fully inserted position indicated total worth of about 3.8% $\Delta k/k$ for each safety rod in this loading. Figure 8.7 shows these data.

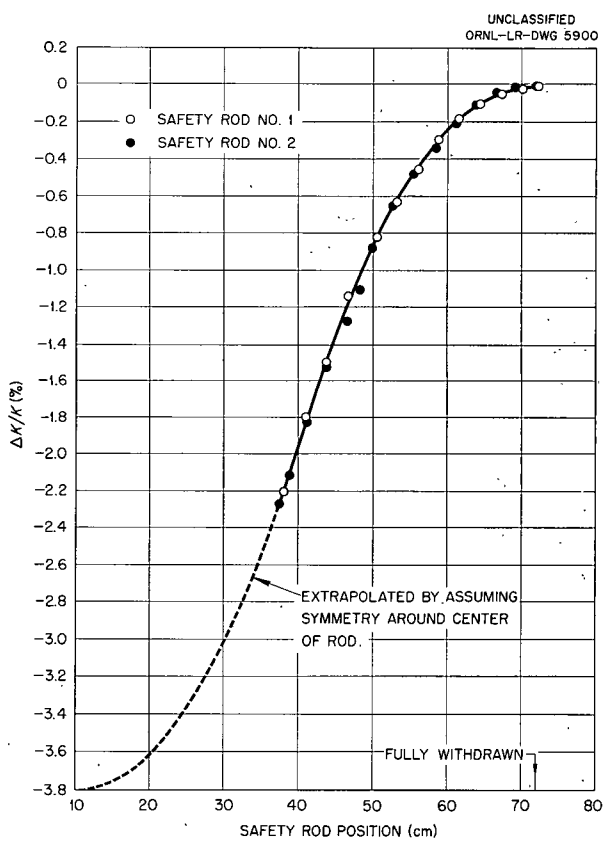

Fig. 8.7. Integral Curves for Boron Carbide Safety Rods in Loading 32 (Beryllium Oxide Reflected).

[8] J. A. Harvey and D. J. Hughes, *Effect of Recent Cross Section Measurements on Pile Constants*, BNL-221 (Jan. 26, 1953).

8.2.3 Inhour Calibration Method

Because of the unexpectedly large effectiveness of the stainless steel regulating rod used in the above experiments, another calibration of this rod in a loading comparable to loading 22A was made. Loading 33 (Fig. 8.4), which, as mentioned above, was essentially a 5 × 6 completely water-reflected arrangement with two elements missing at the corners of the back (south) face, was chosen for this calibration. The difference between loadings 33 and 22A was necessitated by the use of the new unpoisoned fuel elements in loading 33.

The regulating rod was calibrated by means of the inhour equation for a bare thermal reactor. The reactor was brought to criticality at a power level of about 10 w, was allowed to stablize for at least 5 min, and the positions of all rods were noted. The regulating rod was then quickly withdrawn to a predetermined position (the safety rods were not moved), and the rate of increase of the flux level (the reactor period) between power levels of 100 w and 1 kw was determined. It was assumed that the effect of the transient terms on the reactor period would damp out between 10 and 100 w and that there would be no temperature effect at 1 kw. The period is related to the change in reactivity ($\Delta k/k$) by the inhour equation. The data are plotted in Fig. 8.8 as an integral curve. In this loading the stainless steel regulating rod has a worth of about 0.73% $\Delta k/k$, as compared with 1.2% in loading 32.

The B_4C safety rods were calibrated, as described above, by comparison with the regulating rod. Each one has an effectiveness of about 2.5% $\Delta k/k$ in this loading, as compared with the 3.8% in loading 32.

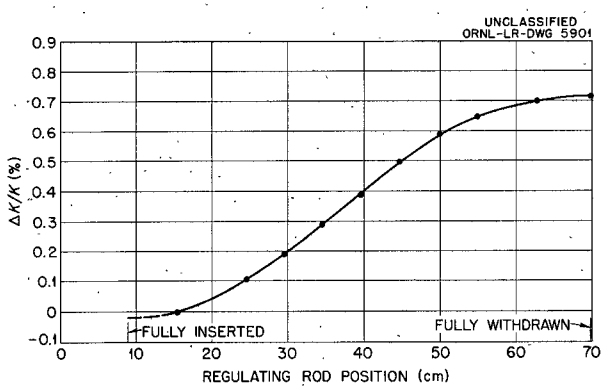

Fig. 8.8. Integral Curve for Stainless Steel Regulating Rod in Loading 33 (Water Reflected) – Inhour Calibration Method.

An inhour calibration of this same regulating rod was carried out in loading 38, a configuration partially reflected by beryllium oxide (Fig. 8.5). The same form of the inhour equation as that for the bare thermal reactor was used; however, the validity of such a procedure is questionable. In this loading the regulating rod has an apparent effectiveness of about 0.5% $\Delta k/k$.

8.2.4 Conclusions

These results present some indication of the variation in effectiveness of a given rod, which is, of course, dependent upon the particular critical assembly in which the rod is used. A summary of the results obtained by both methods is given in Table 8.1.

Further details of this experiment will be published in another report.[9]

8.3 REACTIVITY CHANGES DUE TO BEAM HOLES AND PARTIAL REFLECTORS ADJACENT TO THE BULK SHIELDING REACTOR

E. B. Johnson F. C. Maienschein
R. G. Cochran J. D. Flynn
K. M. Henry

Specific information on the change in reactivity due to beam holes and reflectors adjacent to the reactor is needed for the design of swimming-pool-type research reactors. A series of experiments designed to measure this change in reactivity has been completed. One set of measurements was made with a water-reflected reactor loading and another with the loading reflected on the four vertical sides by beryllium oxide. The reactivity changes were measured relative to the change in position of the previously calibrated reactor control rods. (The calibration of these rods is discussed in Sec. 8.2.)

The water-reflected loading 22A has been described in detail previously.[10] It was a 5 × 6 array of fuel elements with three control rods: two cadmium-lead safety rods and one cadmium-lead regulating rod. In this loading the safety

[9] E. B. Johnson *et al.*, *Reactivity Measurements with the Bulk Shielding Reactor: Control Rod Calibrations; Beam Hole Coefficients; Partial Reflector Coefficients*, ORNL-1871 (to be published).

[10] R. G. Cochran *et al.*, *Reactivity Measurements with the Bulk Shielding Reactor*, ORNL-1682 (Nov. 9, 1954).

TABLE 8.1. EFFECTIVENESS OF CONTROL RODS FOR DIFFERENT REACTOR LOADINGS

Rod	Reactivity Change (% $\Delta k/k$)			
	Loading 22A, H_2O-Reflected	Loading 32, BeO-Reflected	Loading 33, H_2O-Reflected	Loading 38, Partially BeO-Reflected
Cd-Pb regulating rod[a]	0.6[a]			
Cd-Pb safety rod[b]	1.3			
Stainless steel regulating rod[c]		1.2	0.73	0.5
B_4C safety rod[d]		3.8	2.5	

[a]An aluminum shell filled with a molten mixture containing 7½ g of cadmium and the remainder lead. The effectiveness was measured over the last 12 in. of travel.

[b]An aluminum shell filled with molten mixture containing 17½% cadmium.

[c]An appropriately shaped cylinder of type 347 stainless steel with an 0.087-in. wall.

[d]An aluminum shell packed with B_4C powder.

rods were each worth about 1.3% $\Delta k/k$, and the regulating rod was worth about 0.6% $\Delta k/k$ over the last 12 in. of travel. The regulating rod was calibrated by the inhour formula for a bare thermal reactor, and the safety rods were calibrated by comparison with the regulating rod.[10]

Loading 32 (see Fig. 8.3) was composed of 20 fuel elements arranged in a 4 × 5 lattice completely reflected on the four vertical sides by beryllium oxide reflector elements. Two B_4C safety rods and a stainless steel regulating rod were used for this loading. Each safety rod was worth about 3.8% $\Delta k/k$, and the regulating rod was worth about 1.2% $\Delta k/k$. For this loading the regulating rod was calibrated by means of gold poison uniformly distributed throughout the lattice. The safety rods were then calibrated in terms of the regulating rod.

Five different ducts were fabricated for these tests, as shown in Table 8.2. Each duct, or beam hole, was sealed after having been filled with either air or saturated boric acid solution, or it was equipped with an air line so that pressure could be kept on the duct during the test.

Since the BSR is located in a pool of water with the top of the lattice approximately 17 ft below the surface, it was necessary to devise a method of remotely positioning each duct against the reactor so that it would be held rigidly and would be reasonably unlikely to escape while the test was being run. For this purpose, the pit in the large pool was filled with concrete blocks, and ropes were run through the rings in the blocks to each side of the pool so that at least four ropes could be secured around the duct. With one exception, each duct was positioned against the reactor north face so that the center of the face of the duct coincided with the reactor center line (Fig. 8.9). The reactor was then rolled away from the duct and brought to a low power level. The positions of all three rods were noted by actual measurements with a meter stick. The position of the regulating rod was initially (with reactor and duct separated) such that the power level could be maintained without moving the safety rods when the reactor and duct were brought together. The reactor was then cautiously rolled against the stationary duct, allowing the servo to maintain power level. The new position of the regulating rod was noted, and the reactor was shut down. This procedure was repeated with each of the ducts. The data are recorded in Table 8.2 for both the water-reflected and the beryllium oxide–reflected loadings.

The change in reactivity due to the ducts was greater for the beryllium oxide–reflected loading

TABLE 8.2. SUMMARY OF BEAM-HOLE EXPERIMENTS WITH THE BSR

Duct		Duct Filler	Reactivity Change (% $\Delta k/k$)		$C = (\% \Delta k/k)/D$	
Outside Diameter (in.)	Length (in.)		Water-Reflected Reactor	BeO-Reflected Reactor	Water-Reflected Reactor	BeO-Reflected Reactor
17¾	36¾	Air	−1.4	−1.12[a]	0.004	0.0035
8⅛	47¾	Air	−0.55	−0.47	0.009	0.007
6	47¾	Air	−0.36[b]	−0.25[b]	0.010	0.007
6	47¾	Borated water		−0.245[b]		
6	47¾	Air		−0.01[c]		
6	12	Air		−0.26		0.007
6	12	Air		−0.10[d]		
4¼	44	Air	−0.14[e]		0.007	

[a]This duct was larger than the active portion of the lattice.

[b]This duct was held approximately ⅛ in. away from the reactor face by a weld on the face of the duct.

[c]This reactivity change is that resulting from placing the duct against the boral sheet. It is obtained from the difference in regulating-rod positions with only the boral sheet against the reactor and with the duct in position against the boral sheet.

[d]This measurement was made with the duct at the edge of the north face; the face of the duct was against the reflector elements in lattice positions 2 and 3 (for reactor loading see Fig. 8.3).

[e]This duct had a ⅛-in.-thick wall and a ½-in.-thick end, while the other ducts had 1/16-in.-thick walls and ends.

than had been expected. The explanation may lie in an apparent inefficiency of the beryllium oxide reflector (see Sec. 8.2). In any event, the major uncertainty in the experiment would appear to be in the condition of the beryllium oxide reflector elements. These are being recanned, but a simple rod calibration by the distributed-poison method is no longer practical because of the large activity of the fuel elements.

The reactivity effect of the ducts may be related to their cross-sectional area by the expression

$$\Delta k/k = CD^2 ,$$

where D is the diameter of the duct, in inches, and C is a constant for a particular loading. Values of C for each duct are shown in Table 8.2. The results for the 6- and 8-in. ducts are quite consistent, yielding an average value of C of 0.009 (% $\Delta k/k$)/in.^{2} for a water-reflected reactor and 0.007 (% $\Delta k/k$)/in.^{2} for a beryllium oxide–reflected reactor. The value of the constants for the 17½-in. duct was low because this duct was larger than the reactor.

Several reflectors were also run against the north face of the reactor; the results are presented in Table 8.3. The graphite slab and the lead slab were mounted on concrete blocks in the bottom of the pool, and the reactor was rolled cautiously against them for the necessary measurements. The boral sheet, however, was hung from above, but the measurements with it were made in essentially the same way as those in the case of

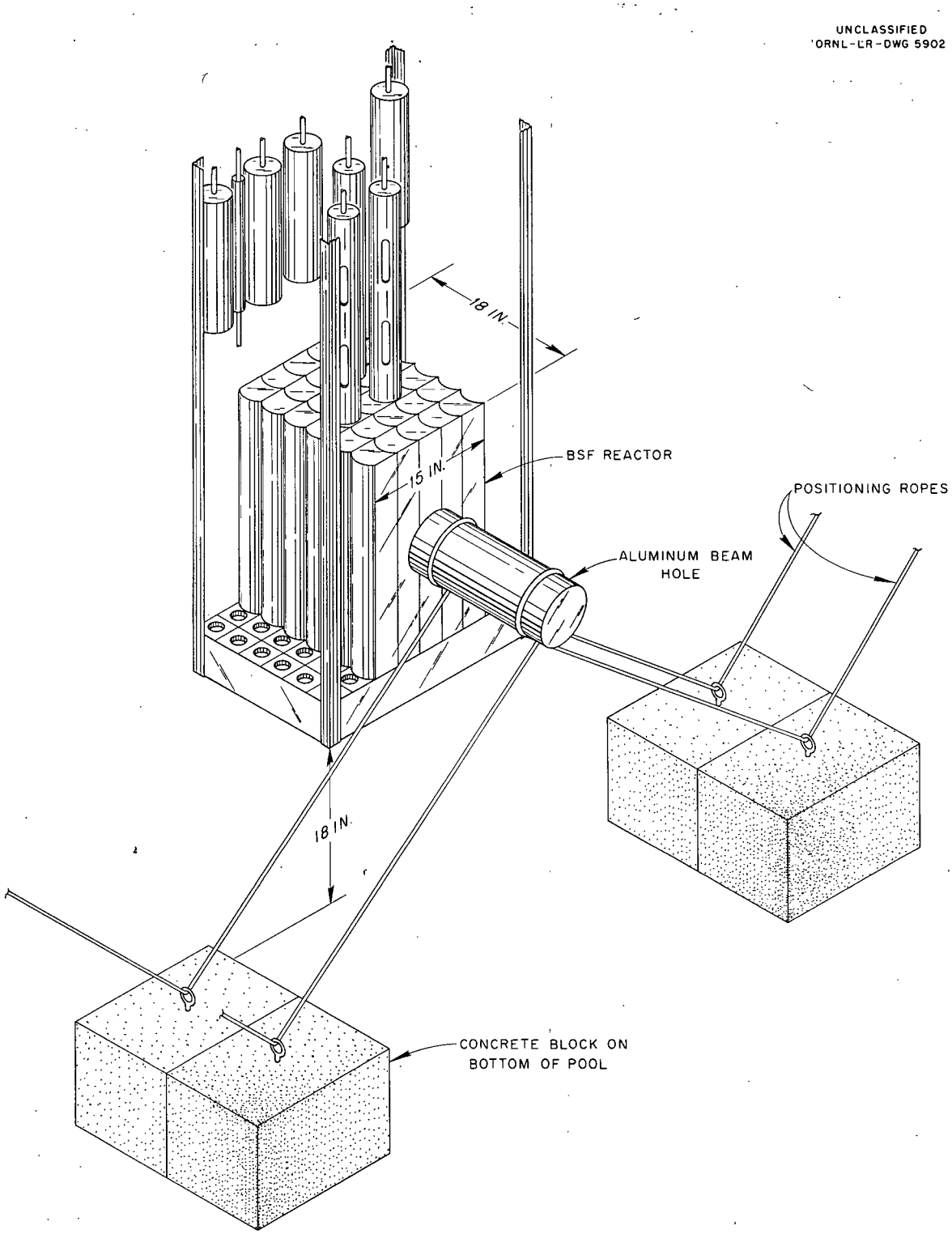

Fig. 8.9. Experimental Arrangement for Tests on the Effects of Beam Holes and Partial Reflectors Adjacent to the Bulk Shielding Reactor.

TABLE 8.3. EFFECT OF PARTIAL REFLECTORS ON THE REACTIVITY OF THE BSR

Reflector*		Reactivity Change (% $\Delta k/k$)	
Material	Thickness	Water-Reflected Reactor	BeO-Reflected Reactor
Boral	$\frac{1}{4}$ in.		–1.36**
Graphite	1 ft		+0.68
Lead	$1\frac{7}{8}$ in.	+0.38	

*All the reflectors extended well beyond the reactor face.

**The boral sheet was held away from the bottom of the reactor face by the structure supporting the reactor.

the other reflectors and beam holes.

The details of this experiment will be incorporated in another report.[11]

[11] E. B. Johnson *et al.*, *Reactivity Measurements with the Bulk Shielding Reactor: Control Rod Calibrations; Beam Hole Coefficients; Partial Reflector Coefficients*, ORNL-1871 (to be published).

9. THEORETICAL PHYSICS

9.1 L-SHELL INTERNAL CONVERSION COEFFICIENTS

M. E. Rose

Since the last report on L-shell internal conversion coefficients was made, there has been considerable progress. Some delay has been encountered because of nonavailability of the SEAC for a period of about two months. As of the date of writing, the internal conversion coefficients listed below have been obtained. In all cases what is implied is a set of ten conversion coefficients – five for electric multipoles and five for magnetic multipoles.

K Shell

- $Z = 25$, 10 values[1] of k (where kmc^2 is the transition energy)
- $Z = 35$, 9 values of k
- $Z = 55$, 9 values of k (the lowest k value does not give energy conservation)
- $Z = 75$, 5 values of k (the two lowest values do not give energy conservation)
- $Z = 85$, 6 values of k (the three lowest values do not give energy conservation)

L_I Shell

- $Z = 15$, 10 k values
- $Z = 25$, 10 k values
- $Z = 55$, 10 k values
- $Z = 75$, 8 k values
- $Z = 85$, 10 k values

L_{II} Shell

- $Z = 25$, 8 k values
- $Z = 55$, 9 k values
- $Z = 85$, 9 k values

L_{III} Shell

- $Z = 55$, 7 k values
- $Z = 85$, 10 k values

In all, almost 1300 coefficients are now available. This represents about 40% of the program.

These results have already proved useful in the interpretation of decay schemes. A study of L/K ratios has been made, and it has become apparent that, where resolution permits, L_I/L_{III} or L_I/L_{II} ratios[2] should be measured. These often provide a more certain clue for the classification of a transition. Simple physical criteria, which indicate which subshell plays the major role in conversion, can be formulated. These criteria are qualitative and show that the factor of importance is the ratio of wavelength ($\hbar/mck$) to shell radius ($\sim\hbar/mc\cdot 1/\alpha Z$). Qualitatively this is roughly correlated to the ratios of transition and binding energies, $\sim k/Z^2$.

[1]The k values are 0.05, 0.10, 0.15, 0.20, 0.40, 0.60, 0.80, 1.0, 1.5, and 2.0.

[2]Alternatively, $(L_I + L_{II})/L_{III}$ etc. ratios may be measured.

9.2 M-SHELL INTERNAL CONVERSION

M. E. Rose A. E. Glassgold

Because it is very often impossible to resolve M and L lines, an experiment provides a $K/(L+M)$ ratio rather than a K/L ratio. To interpret experiments in such cases, one needs to know M-shell conversion coefficients. To calculate these with screening would not be a very practical undertaking. However, the total M contribution should be of the order of 25 to 30% of the total L conversion and in some cases less. Therefore it is entirely reasonable to calculate the former without screening. Experience has shown that the screening corrections are, surprisingly enough, remarkably independent of the principal quantum number so far as the calculations have gone; that is, they are the same for the K and L shells. In these cases they do not amount to more than 10%, and more often are about half that amount.

In consequence, we have set up the M-shell work for the Oracle. When this was done, it was seen that it represented an entirely trivial extension to include the L shell. We refer now to calculations without screening. This work has progressed satisfactorily, and it is hoped that results will be available for inclusion in the next semiannual report. An approximate check on the SEAC work will thereby be provided.

9.3 ORBITAL CAPTURE

H. Brysk M. E. Rose

A rather comprehensive study of orbital capture has been made. The purpose was to provide experimentalists with a handy compendium of all available theoretical results useful for analysis of K and L capture. The following questions were treated quite completely.

9.3.1 Effect of L Capture

L capture includes not only L_I but also L_{II} and L_{III} (i.e., p-states) capture. In general, the L_I subshell plays the major role. An exception to this statement is the case of first-forbidden unique and transition of higher order of forbiddenness. In such cases, capture from the L_{III} subshell predominates for low energies. The results of Rose and Jackson were confirmed.[3] This is of interest in view of the fact that some doubts as to the validity of the theoretical results have been expressed as a result of some experiments giving appreciably greater L_I/K ratios than the calculated ones.

9.3.2 Effect of Electron Transitions

In connection with the foregoing point, it has been suggested that some K captures may appear as L captures, because when a K electron is captured an L electron goes to the K vacancy. This can occur because of the discontinuous change in the coulomb field. We have shown that the probability for this effect, relative to normal K capture, is

$$p = \frac{0.3}{Z^2} .$$

This effect can occur only with the L_I subshell (or other $s_{1/2}$ electrons). For the L_I/K capture ratio, one finds a relative change, in the calculated result, of a factor $1 + pK/L_I$, and the effect is, therefore, of no practical consequence.

9.3.3 Other Effects

The work on capture includes the effect on the K and L electron-wave functions of (1) screening, (2) finite size of the nucleus, and (3) averaging over the nuclear volume instead of evaluation at the nuclear surface. The last is equivalent to replacing the nucleus by a charge distribution of smaller radius and works in the opposite direction to No. 2. For the most part these effects provide marginal corrections.

9.3.4 Angular Correlation Effects

In connection with some angular-correlation experiments on Be^7, it was conjectured that correlation between bremsstrahlung accompanying capture and a succeeding gamma ray had been observed. While this did not seem likely a priori, it was necessary to examine the question with some care because, by such an experiment, one might hope to find a new procedure for obtaining information concerning decay schemes involving capture. Unfortunately, it turns out that the angular distribution is isotropic, except for a very weak contribution arising from transitions involving $p_{3/2}$ electrons. The same conclusion holds for the correlation between the atomic x ray and a succeeding gamma ray.

The work described here in Secs. 9.3.1 and 9.3.3 has appeared previously.[4] A report on the electron transitions mentioned in Sec. 9.3.2 is in preparation. The work on correlation effects has been described earlier.[5]

9.4 HIGH-ENERGY FIXED-FREQUENCY CYCLOTRON STUDIES

T. A. Welton

A previously reported Oracle code for rapid computation of proton-orbit properties in a cyclotron with azimuthal magnetic-field variation has been completely tested, together with a number of convenient modifications for studying various questions not originally considered. In its most recent and generally useful form, the code assumes an equilibrium orbit in the median plane

$$r = q(\theta,\gamma) ,$$

$$q(\theta,\gamma) = q_0(\gamma)\,[1 + q_1(\gamma)\cos(p\theta + \alpha) + q_2(\gamma)\cos^2(p\theta + \alpha) + q_3(\gamma)\cos^3(p\theta + \alpha)] ,$$

$$\gamma = \frac{\beta}{\sqrt{1 - \beta^2}} , \qquad \beta = \frac{v}{c} .$$

The phase angle α is calculated from

$$\alpha(\gamma) = \alpha_0 + \alpha_1 \frac{\gamma}{\sqrt{1 + \gamma^2}} + \alpha_2 \left(\frac{\gamma}{\sqrt{1 + \gamma^2}}\right)^2 .$$

The coefficients q_2 and q_3 are made proportional to q_1 to keep a constant wave form for the magnetic field. The constant q_0 is adjusted by the

[3] M. E. Rose and J. L. Jackson, *Phys. Rev.* **76**, 1540 (1949).

[4] H. Brysk and M. E. Rose, *Theoretical Results on Orbital Capture*, ORNL-1830 (Jan. 25, 1955).

[5] H. Brysk and M. E. Rose, *Angular Correlation in Orbital Capture*, ORNL-1862 (March 23, 1955).

code to hold the orbital frequency constant, and q_1 is continually adjusted by an interpolation procedure so as to maintain a previously prescribed vertical focusing as a function of γ. Magnetic fields, orbit shapes, and horizontal- and vertical-focusing frequencies are automatically printed out.

A large number of runs have been performed for $\alpha = 0$ and various q_n included with $p = 3, 4, 5, 6, 8, 10, 12$. In general, the energy which can be achieved increases markedly as p increases. Unfortunately, to take advantage of this increase, more and more imperfection resonances (in the sense of the A.G. synchrotron theory) must be passed. Also, if $\alpha = 0$, the achievement of proton energies above 500 Mev requires the introduction of reversed magnetic fields, which is quite inefficient. Very encouraging results have recently been obtained for $\alpha \neq 0$, which yields a spiraling magnetic-field pattern similar to that proposed by MURA. For $\alpha_1 = 0$, $\alpha_2 = 16$, for example, no negative fields are required in going to a 1-Bev machine. The first imperfection resonance comes at 450 Mev and should be quite easy to pass. The second comes at 840 Mev and should be very useful for efficient beam extraction. Higher energies can be achieved by careful shimming near the successive resonances. In general, the survey part of the work is nearly complete, and the effort will now be directed at careful examination of a promising configuration, such as that mentioned, in order to make possible profitable model work.

9.5 THEORY OF NUCLEAR FORCES

T. A. Welton

Previously reported work on a reformulation of quantum electrodynamics has led to development of a computation method which is particularly appropriate for work in the pseudoscalar meson theory of nuclear force. In this theory, the coupling constant is so large as to invalidate the usual perturbation calculations, for which no acceptable substitute has previously been available. There exists, further, a large body of important experimental information on nucleon-nucleon and meson-nucleon scattering which cannot yet be used to give a quantitative check of the qualitatively promising symmetrical pseudoscalar meson theory with pseudoscalar coupling.

All essential results of the theory (for one nucleon, excluding closed loops) follow from a simple Dirac equation

$$(1) \qquad K\psi = \gamma p\,\psi + g\gamma_5\,\tau_i A_i(x)\psi \ ,$$

where

K = the "bare" mass,
g = the coupling constant,
τ_i = the usual isotopic spin vector,
A_i = a three-component (isotopic spin space) random, classical, pseudoscalar field.

For illustrative purposes (no loss of essential features), assume only neutral mesons ($\tau_i A_i \to A$). The meson field can be written

$$(2) \qquad A(x) = \sum_{n=1}^{\infty} (-1)^n\, U(|x - \zeta_n|)$$

where

$$(3) \qquad U(x) = \frac{1}{\sqrt{4\pi^3 N}}\,\frac{e^{-\mu r}}{r^3}\,(1 + \mu r) \ ,$$

in which μ = meson mass. N is the number of hypothetical force centers per unit four-volume. An average over all possible force center positions (ζ_n) is to be taken of any formal result in order to obtain a physical answer. The center density N is to be taken sufficiently small ($N \ll \mu^4$) so as to render negligible the contribution to the final averaged result of all configurations of the ζ_n in which overlapping of two force centers occurs. Under these conditions a solution of Eq. 1, before averaging over ζ_n, can be constructed from a solution of the elementary problem in which *one* force center is located at $x = 0$, all others are omitted, and the mass constant is replaced by the experimental mass

$$(4) \qquad m\phi_\pm = \gamma p\phi_\pm \pm g\gamma_5 U(x)\phi_\pm \ .$$

A solution to Eq. 4 can be found in the form of an "incident" four-dimensional plane wave plus a "scattered" wave diverging in *four* dimensions from the force center

$$(5) \qquad \phi_\pm(x) = \Psi(P,x) + F_\pm(P,x) \ ,$$

$$\Psi(P,x) = \chi(P)\, e^{iPx} \ .$$

A solution of Eq. 1 can then be written

$$(6) \quad \psi(x) = \Psi + \sum_n e^{iP\zeta_n} F_{(-1)^n}(P, x - \zeta_n) \ ,$$

and the functions $F_\pm(P,x)$ can be found by extension, from three to four dimensions, of the

elementary technique of separating Eq. 4 into partial waves of definite total "angular momentum." Solutions of the resulting "radial" wave equations can then be found by numerical integration of *total* differential equations. For the nucleon-nucleon scattering, apparently only the phase shifts at infinity of these partial waves are required, which makes a particularly simple calculation. It is easily shown that the constant K can be determined from m, g, and μ by

$$(7) \quad \mathrm{K} = m + \frac{N}{2} \int dx \, \{[\Psi(x)^* \gamma_5 U(x) \, F_+(x)] - [\Psi^*(x) \gamma_5 U(x) \, F_-(x)]\} \, .$$

It is easy to show that the integral in Eq. 7 reduces to a sum of terms, each involving the phase shift for a single partial wave. It is of the greatest importance to note that the potential (Eq. 3) is so singular at small r that a solution of Eq. 4 is by no means automatically guaranteed. Equation 7 and its analogues for other possible couplings may actually be meaningless unless $U(r)$ is artificially cut off for small r (large momentum transfer). Nevertheless, the physically interesting case described by Eq. 1 *does* yield finite phase shifts without cutoff. The formally equally plausible *scalar* meson theory yields nonsense.

The calculation of $F_\pm$ is being set up for the Oracle, and it is hoped to obtain quantitatively useful information in this way concerning the meson-nucleon and nucleon-nucleon scattering problems.